Towards Realising Long Range Interaction of Strontium-88 Atoms

Preetam Ramchurn

University Supervisors: Dr. Yeshpal Singh, Prof. Kai Bongs

15/09/2022

UNIVERSITY OF BIRMINGHAM

UK National
Quantum Technology Hub
Sensors and Metrology

University of Birmingham
PhD Translational Quantum Technology 2018/21

Contents

Abstract

Study of the quantum phenomena present in interacting ultracold gases has led to many fascinating discoveries and applications, such as quantum computing and more precise measuring of time to amazing accuracy of 1 part in 10^{-18}. The future of innovation lies within the world of the small and so many physicists have devoted their efforts into probing into this frontier.
This thesis is concerned with manipulating atoms in the alkaline earth metal, strontium-88, which have the property of long-range dipolar interactions that come about from coherent exchange of photons on the $^3P_0 \rightarrow ^3D_1$ transition. A look back into the historical developments of the techniques used for long range interaction experiments is shown, followed by the present methods used for achieving laser cooling and magneto-optical traps (MOTs). This is followed by a description of the experimental setup used inside of the lab to cool and trap approximately 1 billion Sr atoms to temperatures of 1.1 mK at a density of 10^{11} cm^{-3} inside of a blue MOT. The lifetime of the trapped $^3P_2$ state is shown to be 1.1 seconds. Zeeman sideband spectroscopy allows measurement of the Landé g factor of $^3D_1$ state which is shown to be 0.4995(88) which is in good agreement with the theoretical Landé g factor value of 0.4988. The 2.6 µm laser is currently free running but a specialised cavity housed within a titanium chamber has been created to allow stabilisation.

Further plans for the future of this experiment are outlined as circumstances did not allow these to be completed. After construction of the novel adjustable length 2.6 µm cavity, the next step would have been to integrate this into the experiment. This should increase the number of the captured atoms and perform even better Zeeman spectroscopy. The plan is to then develop the cross laser trap for the dipole 1.06 µm laser. Further evaporative cooling could be performed on the MOT with this installed to achieve denser samples of atoms. This BEC would use a different isotope of ^{84}Sr due to its much better elastic scattering compared with that of ^{88}Sr which actually has a negative value of -2. The optical lattice for the sample can also be performed using the 813 nm laser, frequency doubled to 412 nm and even more upgrades to the vacuum system can be made for better results.

Acknowledgements

Many thanks to my family and friends who have made living through a worldwide pandemic easier where many others had lost hope for the future. I also wish to thank my supervisors Yeshpal Singh and Kai Bongs along with EPSRC for initiating me into the PhD. I thank Marco Menchetti for introducing his setup I would then take over when I visited the Met & Mat building for the very first time. I must also thank the group of colleagues I worked alongside with during the MRes to build the portable magnetometer, Bruce, Richard, Ben, Simon, Ross and Sean. Though we may not have succeeded with all our planning, it was still an enjoyable experience nonetheless which spurred me on to undergo the PhD.

My sincerest thanks to Shengnan Zhang who supervised, guided and most of all was patient with me as I struggled to get to grips with understanding new experimental techniques. I have no doubt you will continue to be with Sandhya and Balsant, the newest additions to the project and a massive help to ourselves. Thanks also to colleagues inside of the cold atoms group, Richard, Freya, Jonathan Jones, Jonathan Winch, Jonny, Sarah, Jithin, Yoge and Alok, who not only assisted but livened up the atmosphere of the office and made tedious lab work more fun over the years. I also wish to thank the physics stores in Met & Mat building, Physics West building as well as their respective workshops for managing to carry out our requests despite how busy they were.

1 Introduction to cold atoms and their applications

This project aims to achieve the observation of a long range interaction between strontium atoms but before this can be done there must be adequate preparation of the atoms beforehand. The atomic sample must be cooled and dense enough to enter a new state of matter in a Bose-Einstein condensate for which the techniques of laser cooling, optical lattices and magneto optical trapping are required. This introductory chapter will explore the origins of these techniques and how they are being applied both inside the lab and outside in the world to achieve greater levels of metrology.

To be clear, the aim of this project is not to develop a clock but it may be helpful to consider their development to better understand the physics of cold atoms.

Atomic Clocks

The world that humans have interacted with over the course of their history for the most part can be understood using classical mechanics which came about by observations made using the most rudimentary of instruments - human senses. With a limited range of vision (400-700 nm) corresponding to the visible light spectrum, a range of hearing from 20 Hz to 20 kHz bested by many other mammals as well as taste, smell and touch, human beings are essentially blind and deaf to their surroundings regarding the universe.

Science is able to enhance the human senses by using innovative measuring instruments to probe the universe in ways humans cannot access which leads to a better understanding of how physical interactions occur. Something that the human body is purported to have is an internal clock, something that has evolved alongside nature to help regulate humans' existence over the course of days by using the Sun[1], months by using the Moon and years according to the changing of the weather with the four seasons.

The idea of time and the measurement of it was a major contributor to how early humans could effectively track harvests, plan for journeys and eventually create more precise and better instruments for science, such a bag of sand with a hole replaced with an hourglass that then develops into a stopwatch. The best and most accurate clocks of today come about from studying the interactions of atoms on the nanoscale and below. When dealing with objects of such a small size, weird things can happen that baffle human common sense ideas, such as quantum tunneling - a particle that can be found outside of a potential barrier that it was supposedly trapped inside, lacking the energy to escape[86]. This would be analagous to seeing a ping pong ball inside a cardboard box suddenly roll through the wall and there are many other quantum phenomena that occur down at the atomic scale.

Every clock generally needs three things in order to function: 1) an oscillator, 2) a counter and 3) a frequency reference. The oscillator is needed for a regular tick which may be a swinging pendulum in old style grandfather clocks, an electrical oscillator in a watch or the laser for an atomic clock which is a defined amount of time t_{cyc}. The counter would then count up the number of these to work out the amount of time that has passed using $t_{clock} = Nt_{cyc}$ where N is the number of cycles that have passed. The frequency reference ν_0 would be a well-known frequency, such as a quartz crystal in a watch[87], to prevent the oscillator from drifting away from the regular ticking by adjusting the oscillator towards it[4]. The quartz crystals' refinement and development has led to losing 1 s over a time of 100 years but even then it is not good enough for some things. After 1 hour, the best quartz oscillators can be off by a nanosecond which would be detrimental to measuring a fast moving object, like that of a spacecraft[5]. An oscillator will be more stable (precise) the more ticks it gives per second but its accuracy is related to how close a measured value is to the target value. Fig 1 shows the differences between stability and accuracy.

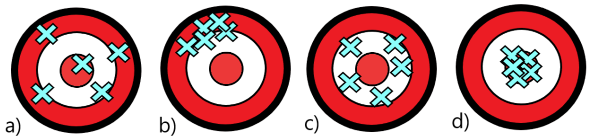

Figure 1: a) Neither stable nor accurate. b) Stable but not accurate. c) Accurate but not stable. d) Both stable and accurate.

Application of clocks

Work on cold atoms has had exciting breakthroughs over recent history which are responsible for many of the technological developments we enjoy today. Atomic clocks are useful for transferring data over networks as well as utilised in miniaturised accelerometers, magnetometers and gyroscopes. Inventions such as GPS (Global Positioning System) required the use of highly accurate clocks in order to make sure the satellites that orbit the Earth remain chronologically in sync with us on the surface due to relativistic and gravitational effects on time dilation that are so small yet they would cause errors if left unchecked for a long period of time. Optical clocks can assist gravimeters which can resolve differences in height below 10 cm when changes in gravitational potential would be unknown[6]. There have been clocks as precise as ultracold ^{171}Yb (ytterbium) with an instability of 1.6×10^{-18} per 25000 s[7]. The quartz crystal in a watch is susceptible to changes in its environment which means any two watches will disagree over what the time may be the longer they are in use. If the reference frequency were tied to something much more stable, like that of an atomic transition ($\nu_0 = E_2 - E_1/\hbar$), time keeping will be much more consistent no matter where in the world it is used. For this reason, in 1967[8], time had been redefined using caesium atoms and the International Units (SI), so that a single second would be known as the length of time taken for 9,192,631,770 periods of the radiation corresponding to the transition between the two hyperfine levels of the unperturbed ground state of the ^{133}Cs atom[13].

In 1971[9] [10], atomic clocks were used to test Einstein's theory of relativity by attaching four caesium clocks to a commercial jet flying around the world both east and west and comparing to a clock stationed on the Earth's surface. The findings managed to confirm the prediction made by the theory as all the clocks disagreed with one another. The clock on the eastern flight lost 59 ns and the western flight gained 273 ns in comparison to the stationary Earth clock which was within margins for error of 25 ns.

Optical clocks have been made by using alkaline-earth atoms due to their level structure allowing laser cooling and their clock transitions are narrow enough to avoid being affected by frequency shifts from external fields[11] [12].

1.1 History of laser cooling

The idea of cooling atoms via laser beam was explained by T. W. Hänsch and A. L. Scawlow[20] in 1975, then brought to life in experiment by D. J. Wineland[21] who reduced Mg^{+2} ions to a temperature of 50 K via radiation pressure. Cooling something means it is robbed of its internal kinetic energy, in macroscopic terms this would be through processes like convection, conduction or radiation. By shining a laser light against an atom travelling with a velocity, the photon can be absorbed which excites the atom and reduces overall momentum by an amount $\Delta p = h/\lambda$ to then be re-emitted in a random direction upon de-excitation. Over many instances of this re-emission the atom's net velocity remains unchanged due to averaging direction and only the absorption hinders the atom. Very shortly after in 1979, Wineland and Itano[22] research into how the kinetic energy of a collection of resonant absorbers were lowered by irradiating them with near-resonant electromagnetic radiation.

In 1982 W. D. Phillips cooled down neutral atoms[23], who utilised a novel idea; the Zeeman slower, able to reduce the velocity of the atoms in such a way that they remain on resonance with the laser, exiting with 40% of their starting speed. A Zeeman slower is a specific arrangment of a magnets designed to accept atoms with speeds of ≈ 100 ms and by the time they reach the exit will be slowed to ≈ 10 ms. Atoms that have a certain distribution of velocities will be affected by the magnetic field inside a cylindrical tube so that a laser coming from the opposite direction will always be on resonance with them no matter where inside the tube they may be. In this way the atoms will be constantly subjected to the absorption-emission cycle throughout the entirety of their time inside and therefore the speeds can be reduced to the fullest degree.

S. Chu *et al.*[24] in 1985 trapped and cooled neutral (sodium) Na atoms in three dimensions using the radiation pressure of counter propagating beams. The atoms had a density of $\sim 10^6$ cm^{-3} and a temperature of ~ 240 µK which they achieved through the use of viscous damping. One year later in 1986 saw S. Chu *et al.*[25] use the dipole force to trap atoms which was later used to create the first magneto optical trap (MOT)[26]. By arranging 3 orthogonal sets of counterpropagating laser beams an "optical molasses" (OM) was created that allowed dense pockets of atoms to be trapped within the small volumes that the overlapping beams provided. Advantages of using a single strongly focused Gaussian laser were that it eliminated standing waves thereby reducing dipole-force heating, which can sometimes supply energy for an atom to escape its confinement. They also provided deeper wells for trapping over a few optical wavelengths.

R. Santra in 2003[59] decided to explore the lowest $^3P_2$ state of alkaline-earth metals, specifically strontium-88 as he was aware of the long lifetime and the potential to be trapped magnetically. He also chose to work with Alkali atoms due to the fact that they have a strong electric dipole transition from ground state that is in the visible light spectrum so they can be laser cooled as well as the existence of the unpaired outermost electron, solely responsible for its magnetic dipole moment, thus being susceptible to external magnetic fields. It was shown that if the separation of the Sr, R, were between 100-1000 Bohr radii then the electric quadrupole-quadrupole interaction dominated but increasing that to the long range limit $R \geq 1000$ Bohr radii meant that the dipole-dipole interaction dominated.

That same year (2003), T. Ido[60] [61] and H. Katori worked with neutral Sr atoms in order to demonstrate a recoil-free spectroscopy on the $^1S_0 \rightarrow ^3P_1$ transition that had been trapped inside a 1-D optical lattice. The atoms were kept under the Lamb-Dicke regime so no Doppler or recoil shifts could affect the measurements of the atomic spectrum which led to the discovery of the magic wavelength at which both states experienced Stark shifts.

A year later in 2004, P. Pellegrini[62] had performed photoassociative spectroscopy (PAS) on $^{88}Sr_2$. PAS was used to further understand the dynamics of collisions in an intercombination-line MOT to obtain a result for the lowest $^1P_1$ state of Sr ($\tau = 5.22 \pm 0.03$) ns.

T. Ido (*et al.*)[63] in 2005 worked on ultracold ^{88}Sr samples by changing their density from 10^9 to more than 10^{12} cm^{-3} so they could measure the density-related frequency shift and linewidth broadening for the $^1S_0$-$^3P_1$ optical clock transition. At that time they also gave the most accurate measurement of that same transition frequency $[434,829,121,312,334 \pm 20(\text{stat}) \pm 33(\text{syst})]$ Hz.

In 2007 the effects of nuclear spin in optical lattice clocks had been researched by Boyd[27] which presented a perturbative approach for describing the state mixing and magnetic sensitivity of the clock states was given for a general alkaline-earth(-like) system, with ^{87}Sr used as an example. The g-factor of the $^1S_0 \rightarrow ^3P_0$ clock transition was also measured to be $\mu_0 \delta g = -108.44 m_F$ Hz/G. In addition the upper limit for the differential and excited state tensor shift coefficients $\Delta\kappa^T = 0.02$ Hz$/(U_T/E_R)$ and $\Delta\kappa^T_e = 0.01$ Hz$/(U_T/E_R)$ have been measured. It was also shown that a polarizing scheme can be used to control the nuclear spin related effects in the ^{87}Sr lattice clock to values greatly under 10^{-17}.

Application of laser cooling

The optical spectroscopy for these kinds of experiments are sensitive to atomic motion because of the Doppler effect. Doppler effect can limit the final accuracy of clocks based upon clouds of atoms in free fall, in comparison to what had already been achieved by the best Cs fountains. What is gained in improved stability will be lost via accuracy due to the Doppler shift.

As seen earlier, laser cooling is a necessary factor to achieving the most stable atomic clocks but it also functions as the preparation of atoms for further experimentation by making them ultracold. Laser cooling has moved on from atoms to diatomic molecules[28] as well as being performed on macroscopic objects, such as a 1 g sample being dropped to 0.8 K[29].

Further applications of this can lead to lasers able to function without generating internal heat[30]. More recent discoveries allow the removal of phonons in a solid to achieve optical refrigeration[31] which would lead to electronic and optical devices to operate at cooler temperatures without any vibrations.

1.2 History of Bose-Einstein Condensate (BEC)

Satayendra N. Bose[32] was researching how photons did not have a thermal distribution that followed the Maxwell-Boltzmann model. If particles follow the function Bose discovered they would be classed as bosons. When a cloud of atoms in a gas are confined to small regions of space and cooled to temperatures approaching 0 K, they can exhibit strange effects as their wavefunctions spread out and interfere with each other to create an essentially gigantic particle. This state of matter was predicted by Albert Einstein[33] back in 1925 after looking at Bose's work.

The first attempt to create this Bose-Einstein condensation was performed in 1938 with a superfluid liquid Helium-4 (^{4}He)[34][35] as it was thought that superfluidity was a result of BEC. Particles in the superfluid have strong interactions which is contrary to the model Einstein proposed which had non-interacting particles. It had been predicted that interactions would change the underlying physics of a BEC. It seems that only 7% of the superfluid particles actually become condensed[36][37][38] despite reaching absolute zero temperatures.

In 1995 the first BEC was created via evaporative cooling of Rubidium (Rb) by M. H. Anderson[72] though Sodium[73] and Lithium[74] had been done shortly after. When a gas of bosons that normally has very low density becomes cooled enough it will undergo a change in state separate from that of solid, liquid and gas and even a plasma. The change is such that the bosons in the gas will almost fully occupy the same lowest level quantum state and then their thermal de Broglie wavelengths will overlap so much as the bosons' separation from one another becomes even smaller by comparison. Thus the microscopic phenomena of wavefunction interference occurs across the whole of the condensate, which is macroscopic.

Laser cooling alone was not sufficient to cause this phenomenon so an additional evaporative cooling stage was added to cause the remaining highest energy atoms to leave the gas. By removing the most energetic of atoms, the remaining atoms in the trap were on average cooler in temperature and therefore more dense allowing condensation to occur.

A few years later in 1998, a review paper outlining the theory behind these three types of BEC was written by F. Dalvofo *et al*[75]. The main takeaway from their work was that even though the gases are dilute, two-body interactions govern the physical properties of the gas.

In 1999 a paper outlining experimental techniques making use of a BEC was written by E.A. Cornell[76]. Its purpose was pedagogical and was intended to help push the development of experiments involving BECs by condensing lectures previously given. Even back then they were aware of how important this work would be in the future and its rapid pace of progression.

After the BEC was made, in 2004, cold atom systems were thought to be a useful method to study many-body physics,[77] until this time the atomic densities were too small to have significant LRI effects in the sample.

Manipulation of alkaline earth metal atoms came about as a result of these developments in creating ultracold atoms. Deshui Yu in 2013[71] was able to work with Strontium in a blue-detuned optical lattice that exhanged virtual photons, leading to low-lying triplet states exhibiting long-range interactions as well as collective dissipation. In 2015, using that study as a basis, they investigated the far-zone fluorescence from an ensemble of two-level atoms alongside long-range dipolar interactions through use of light. They focus on finding things like photon emission rate, fluorescence spectroscopy and second-order correlation of intensity fluctuations. The paper's purpose was to find the effects of LRI on the atoms upon the light-atom interface.

Most recently an attempted replication[78] of a study of "quantum liquids" in a quasi-one-dimensional BEC led to discovery and confirmation of a phenomena where "droplets" may form of a cluster of atoms that behave as their own group of repulsive and attractive forces. Ensembles of individual atoms stuck in an optical lattice or arrays of microscopic dipole traps that are separated by only a few micrometres can be essentially fully controllable with optical addressing techniques. Getting the atoms to interact at distances greater than a micrometre requires excitation to the Rydberg states, states with large principle quantum numbers n[39] [40]. When the atoms are in this high-level state, they have lifetimes that scale as n^3, far longer than the low-level transitions (about 100 µs range for $n \approx 50$). In addition these Rydberg atoms have large dipole moments between states n and $n-1$ with opposite parity, scaling as n^2. The result of which is big interaction strengths V which relates to frequencies of $V/h \geq 1$ MHz (h being Planck's constant) for $n \approx 50$ at distances ~ 5µm.

Application of BEC

Getting atoms into this weird state of matter allowed physicists to discover new things about them that can ultimately lead to more exciting technologies. For example, dark solitons were able to be observed as they had longer lifetimes when trapped in a ^{87}Rb Bose-Einstein condensate[42].

Recently there have been experiments on excitons and photons which become a 2-D bosonic quasiparticle trapped in a microcavity that can make it possible to achieve a BEC at room temperature[41]. It is also proposed that these exciton-polaritons can create a superconducting device at only a few tens of Kelvin.

Logic gates have been made based on storing two light pulses inside of a BEC[43]. It uses atomic-four wave mixing to make a new matter wave and then is able to recall the two pulses. A different approach used BEC quantum walks where a light pulse makes a single BEC travel along a route that can be manipulated with further microwave pulses[44] [45]. The difficulty with this method was that the system could not encode a problem at that time.

It is expected that the next application of cold atom physics will be of equal, if not more, importance than those that came before, namely quantum computing, a much faster alternative to the computers used currently. In order to make a "quantum computer" a reality, new components called "qubits" are to be used to replace traditional "bits", capable of not only being in a 0 or 1 state (OFF or ON), but something in between as well. However, these qubits need to be able to communicate with each other in order to do anything useful and that is where the long range interaction is needed to allow this over a whole array of particles. BECs were the stepping stone to develop things such as superfluids which are necessary for the operation of quantum computers by cooling down the semiconductors to temperatures of a hundreth of a Kelvin. A great example of quantum computing's usefulness comes from searching for a specific item out of a list of N items. Traditional computers would have to randomly select one by one until the correct item is found which on average would take $N/2$ attempts. A quantum computer could perform the same task with only $\sqrt{N}$ attempts by using a quantum logic based algorithm[46].

There are four approaches currently used to achieve long-range interaction in cold atoms: using atoms with large magnetic dipole moment (such as chromium)[14], using polar molecules[15], using Rydberg atoms[16] or light induced dipoles.[17] [19]

1.3 History of long range interaction (LRI) in cold atoms

The long range interaction necessarily involves atoms ”communicating” with several other surrounding atoms and so on, which would be very difficult to keep track of and describe. An area of science known as many-body physics deals with exactly this problem concerning condensed matter, nuclear and high-energy physics and there are experimental observations that are still not fully understood. Trying to relate properties on the macroscopic scale to the microscopic laws of particle interactions is hard due to the exponential scaling of Hilbert space size as the number of them increases. Approximations are required to solve the many-body questions but that comes with the problem of finding out when the results would be valid.

Richard Feynman[47] in 1982 came up with an idea to build a quantum system synthetically in a lab and then apply an approximate model for real world material (but can also be made up) which leads to an artificial many-body system that then becomes something to study itself. A benefit to this method is that parameters can be changed to an extent that wouldn't otherwise be possible so the effects could be studied better, such as discovering how interatomic interactions are related to the phase of a certain system by varying their strength. Synthetic systems are able to be tinkered with to such a degree that it wouldn't be possible to do in a real material. Feynman's method is known as quantum simulation, also referred to as exploring many-body physics with synthetic systems, an idea that wouldn't be realised until the 21st century due to a lack of experimental control over quantum matter. Recently there are photonic simulators that use propagation of light within a material to cause photon-photon interactions as well as polariton condensates that need cavity quantum electrodynamics in semiconductor micro/nano structures[48]. These polariton quantum simulators are useful to study non-equlibrium physics (such as black holes) due to its finite lifetime.

Physicists that could control the quantum state of an individual atom could also tune their interactions. Their next thoughts came up with programmable quantum simulations that can change all parameters of the Hamiltonian. Such a system could also act as a machine preparing the quantum states as they saw fit for many applications, such as large entangled states that develop into clocks or sensors with enhanced precision[49].

In the future this would develop into the idea of an atom acting as a quantum bit in a quantum computer, capable of computing answers to problems that require more effort than those posed by physics, such as combinatorial optimization, specifically the travelling salesman problem.

Strontium Rydberg atoms were used by C. L. Vailant in 2012[64] to show a perturbative approach to the long range interaction calculations as well as create a table of values for C_5 (first order quadrupole-quadrupole) and C_6 (second order dipole-dipole) co-efficients.

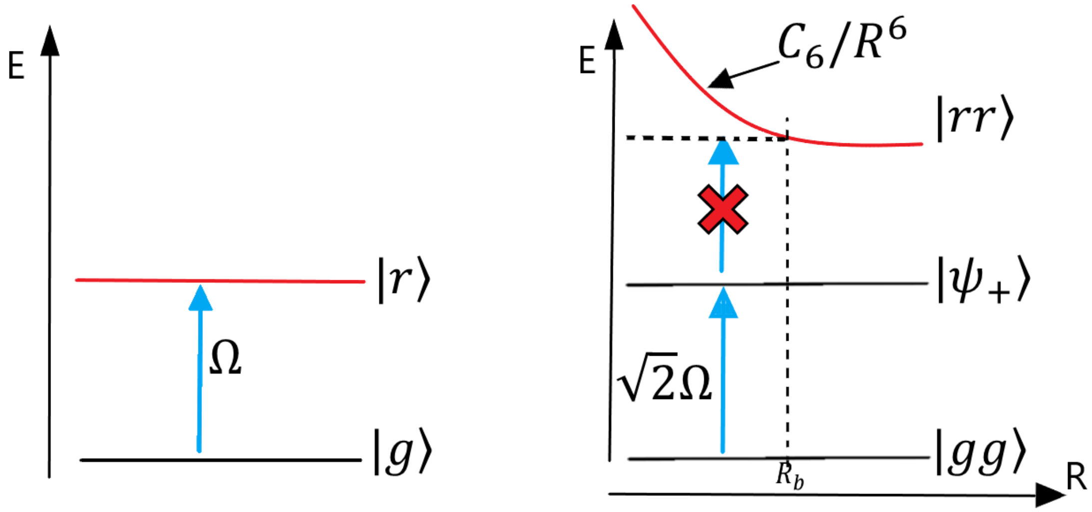

Figure 2: Left: The Rabi frequency between ground and Rydberg state is Ω which the laser is resonant to. Right: When there are two atoms sperated by distance $R < R_b$ the collective ground state $|gg\rangle$ is coupled to $|\psi_+\rangle = (|gr\rangle + |rg\rangle)\sqrt{2}$ but not $|rr\rangle$ due to being moved out of resonance by Van der Waals interaction.

Rydberg blockade

The Rydberg blockade is a phenomenon that occurs between two atoms that are close to one another when a laser that is on resonance with one of them excites it to the high-level Rydberg state and then that same laser cannot promote the second atom to the same level because the presence of the first atom shifts the energy level higher for the second atom. This effect can be used to prevent simultaneous excitations of two neighbouring atoms and generates entangled states. Dipolar interactions with Rydberg atoms have been observed in 1981 by Raimond[50].

Consider a resonant laser to the ground state $|g\rangle$ and a rydberg state $|r\rangle$ which has a Rabi frequency of Ω (see Fig 2). If now there are two atoms in proximity starting off in state $|gg\rangle$ with one of them labelled as the "control" and the other one as "target", separated by a distance of R, then the double excited state $|rr\rangle$ will be shifted by an amount C_6/R^6 because of the Van der Waals interaction, where C_6 is the co-efficient of interaction. When a 2π pulse ($\Omega t = 2\pi$, t being the pulse time) is applied to the target atom this will lead to excitation and de-excitation of the target atom giving phase shift π on the quantum state $|g\rangle_t \rightarrow -|g\rangle_t$. If, however, the control atom is first excited to the Rydberg state whilst the target atom remains in the ground state: $|\psi_+\rangle = (|gr\rangle + |rg\rangle)\sqrt{2}$ with a coupling of $\sqrt{2}\Omega$, the coupling with $|rr\rangle$ becomes off resonance and therefore suppressed which leads to Rabi oscillations of the atoms at frequency $\sqrt{2}\Omega$ between the ground state $|gg\rangle$ and entangled state $|\psi_+\rangle$. The target atom then undergoes $|g\rangle_t \rightarrow |g\rangle_t$ when subjected to the 2π pulse.

If now the same priniciple is applied to an ensemble of N atoms which are within a blockade volume, at most one Rydberg atom excitation is possible, which then leads to group Rabi oscillations with an enhanced frequency of $\sqrt{N}\Omega$ between the collective ground state $|g...g\rangle$ and the entangled state $\sum |g...gr_i g...g\rangle / \sqrt{N}$ where Rydberg excitation is distributed amongst remaining the atoms. If the system's size is larger than the blockade radius then there can be multiple excitations for Rydberg atoms but the positions are strongly correlated due to the blockade constraint, ultimately leading to many-body dynamics.

This means the target atom's excitation dynamics and phase are subject to the state of the control atom. Experiments are set up in such a way using atoms that are close enough to have strong interactions but also far enough to be controlled individually. This blockade comes about by localising single atoms to regions formed by tightly focused beams from a far-detuned laser. By focusing the waist of the beam to $w \sim 10$ µm the atoms can be moved by displacing the control laser, despite the trapping sites being in proximity. As well as this, the Rydberg levels at $n = 79$ to 90 are excited and the strength of the LRI between the two Rydberg atoms scales as n^{11}, where n is the principle quantum number.

Though quantum gases are dilute systems (densities of about 10^{14}-10^{15} cm^{-3}) nearly all of the properties are dictated by the interaction between particles. For temperatures of nK, only s-wave scattering will occur between particles. Huang and Yang in 1957[51] showed the real interatomic potential (which would be Van der Waals: $V(\mathbf{r}) \propto -C_6/r^6$) can be switched out for a short-range, isotropic pseudo-potential:

$$\frac{4\pi\hbar^2 a}{m}\delta(\mathbf{r}-\mathbf{r}')\frac{\partial}{\partial|\mathbf{r}-\mathbf{r}'|}|\mathbf{r}-\mathbf{r}'| \tag{1}$$

a being the s-wave scattering length, m the atomic mass along with a regularization operator that is added to remove the singularity of the delta potential in 3-D.

At the start of 2016 it was demonstrated by R. T. Sutherland and F. Robicheaux[52] that homogeneous line-broadening in a diffuse cold atom cloud was proportional to the resonant optical depth of the cloud. In addition they showed how the strong directionality of the coherent interactions caused the cloud's spectra to strongly depend on the shape. They chose to use strontium-88 for their calculations, focusing on the ${}^1S_1 \rightarrow {}^3P_1$ transition and discuss an experimental application to verify their work. A curious result they share is that in a highly elongated cloud in the direction of laser propagation with a red-detuned laser, atoms at the back of the cloud have a greater chance to be excited than those at the front. This finding runs counter to exponential decay given by the Beer-Lambert law.

Another 2016 paper by S. D. Jenkins and J. Ruostekoski[53] utilised rubidium (Rb) gas to show how cold, dense atomic gases had a different optical resonance than their thermal counterpart due to a Doppler shift. By using both numerical simulations and experimental observation, they found the fluorescence witnessed in a cold Rb sample is not affected by these shifts as much the hot gas is so they can be on resonace with incident light more often, leading to further resonant light-mediated interactions with other atoms. The simulations used the physics of recurrent scattering between atoms where the light can be scattered more than once by the same atom. In the case of cold, dense ensembles it will lead to sub- and superradiant excitations.

In 2018, R. Jones (*et al.*)[54] found a way to manipulate a dense cluster of atoms by placing them near metallic or dielectric surfaces. Ordinarily, if the average separation was comparable or smaller than the wavelength of the scattered photons, then there would be a long range coherent interaction of virtual photons amongst the atoms. However, next to these surfaces the scattering properties can be changed to allow an improvement in the efficiency of the transport of an excitation in a 1-D lattice. This would increase the lifetime of the excitation whilst maintaining the transport due to coherent dipole-dipole interactions.

Light-induced dipoles

Recently in May 2020, A. Glicenstein[55] studied resonant light scattering in a 1-D randomly filled atomic chain. As the light scattered was measured along the chain, it was found that there were constructive interferences in the light-induced dipole-dipole interactions between the atoms. The interesting thing they found was that there was a shift in collective resonances even though the interatomic distance was larger than the light's wavelength, explained by strong collective effects being enhanced due to the particular geometrical arrangement of the atoms.

As explained in the paper, consider a 1D chain of atoms excited by a plane wave (with frequency $\omega = kc$) that propagates along the z-axis. When the intensity is low, the dipoles behave as though the E field is linear (i.e. the dipole of atom n at position z_n is $d_n = \epsilon_0 \alpha E(z_n)$, where $\alpha = i(6\pi/{k_0}^3)/(1 - 2i\Delta/\Gamma_0)$ is the atomic polarisability. Also $k_0 = 2\pi/\lambda_0$ is the transition wavevector, $\Delta = \omega - \omega_0$ the detuning with respect to the single-atom frequency ω_0 and Γ_0 is the linewidth.

As the driving field propogates in the z-direction it gains a phase kz_n on atom n. Induced dipole d_n then scatters a field phase-shifted by $\phi = \text{Arg}(\alpha)$ with respect to the driving plane wave. The scattered field then gains a phase $k|z - z_n|$ by propagating along z-direction. Going forwards ($z > z_n$) the phase accumulated by the field scattered by a single atom is $kz + \phi$, which is independent of the atom's position. Considering all the atoms, the fields scattered forwards are all in phase from first order and so will constructively interfere. The 1-D geometry is what allows this deduction and should hold up even with position disorder along the chain. Conversely, should the atoms not be aligned along z, the phases collected by scattered fields will depend on their position, therefore superposition in the forward direction will not lead to constructive interference.

Application of LRI

The long-range interaction can have interesting effects on a set of atoms that make studying them yield new solutions. One such example comes from studying a Klein–Gordon lattice, containing a non-trivial frequency band and linear dispersion, and a Gorbach–Flach lattice, which has only non-linear terms[56] which are shown below in eqns (2) and (3) respectively. Special low-dimensional solutions are found by exciting an atom in the KG setup which causes the energy to spread out but in the GF model it remains localised.

The KG lattice has quartic and quadratic on site potential and linear dispersion terms given by[56]:

$$H^{KG}(p,x) = \sum_n \frac{1}{2}{p_n}^2 + \frac{1}{2}{x_n}^2 + \frac{1}{4}{x_n}^4 + \frac{C}{2}(x_{n+1} - x_n)^2 \tag{2}$$

The GF lattice has N coupled oscillators, sharing the same on site potential as KG but only quartic interactions for the nearest neighbours' sites[56]:

$$H^{GF}(p,x) = \sum_n \frac{1}{2}{p_n}^2 + \frac{1}{2}{x_n}^2 + \frac{1}{4}{x_n}^4 + \frac{C}{4}(x_{n+1} - x_n)^4 \tag{3}$$

This means GF is free from linear dispersion. For (2) and (3), p_n and x_n are the canonical conjugate pairs of momenta and positions. The boundary conditions are $x_0 = x_N, x_{N+1} = x_1$. Both (2) and (3) have the form[56]:

$$H(p,x) = \sum_n \frac{1}{2}{p_n}^2 + V(x_n) + W(x_{n+1} - x_n) = E \tag{4}$$

with E being the total energy. $V(x)$ is the hard on-site potential $\frac{1}{2}x^2 + \frac{1}{4}x^4$ in both KG and GF systems. $W(x)$ is the potential functions $W^L(x) = \frac{C}{2}x^2$ for linear coupling in KG and $W^N(x) = \frac{C}{4}x^4$ for non-linear coupling in GF.

A mathematical model for LRI systems can be further applied to fluid dynamics, plasma physics, galacticdynamics, and statistical mechanics[57]. A Sr LRI system may be able to improve the measurements of a quantum system that would keep the measured value of an observable intact by coupling the atomic cloud to a light beam[58]. This is known as a quantum nondemolition (QND) measurement; it would be useful to help set up other experiments for spin-squeezed or entangled atoms. This extra control over quantum matter could be the key to preparing a quantum simulator with ultracold Sr. As mentioned for the BEC application, quantum computers benefit from LRI with their vastly improved performances.

1.4 Thesis Outline

The remainder of the thesis is structured as follows:
Chapter 2 focuses on the role played by Strontium in the processes of Laser cooling, trapping and Bose-Einstein Condensation.
Chapter 3 explores the physics behind the processes that will be encountered when dealing with long-range interactions.
Chapter 4 will explain the experiment in detail and what the components' purposes are.
Chapter 5 contains all the measurements taken on the strontium, including the confirmation of the theoretical result for the Landé g-factor of the $^3D_1$ state.
Chapter 6 rounds the thesis off with a conclusion of the LRI setup.

2 Strontium Cooling

2.1 Strontium

Alkaline earth metals are quite abundant in their isotopes with naturally occuring bosonic and fermionic varieties. The bosonic isotopes would not have any nuclear spin associated with them. Following on from the work that came before in Chapter 1, it should be clear how the experiment concerning this thesis will benefit from using the alkaline-metal strontium[65] as it has a single electron governing its magnetic dipole moment, it can be manipulated with magnetic fields and most interestingly, it has a Landé g-factor for the $^3D_1$ state that has yet to be experimentally verified. Confirming this result will be a significant milestone along the way to realising a long range interaction setup for strontium.

2.1.1 Strontium Isotopes

The particular bosonic isotope concerning this thesis is ^{88}Sr, though it can occur as ^{86}Sr and ^{84}Sr as well as fermionic isotope ^{87}Sr. ^{88}Sr is the most abundant in nature at 82.58%, ^{87}Sr occurs at 7%, ^{86}Sr at 9.86% and finally ^{84}Sr at 0.56% being the rarest variety. It is quite reactive when exposed to air so it must be kept under vacuum.

Below Fig 3 depicts the electronic structure of ^{88}Sr. The ground state of $^1S_0$ is able to be excited to state $^1P_1$ with use of a 461 nm laser. The second cooling stage requires use of a 689 nm laser for $^1S_0 \rightarrow {}^3P_1$, which has been used by other groups. Where this thesis differs, however, is the choice of repumping lasers. Though 707 nm will be used to repump instead of using 679 nm, it will be replaced with the 2.6 µm laser, taking advantage of $^3P_0 \rightarrow {}^3D_1$ for more efficient repumping.

Under ordinary room temperature, strontium will be solid but in order to use it in experiments it must be in gaseous form. To do this an oven is required and the higher the vapour pressure of the strontium the higher the number of atoms that will be made. The pressure obeys the Antoine equation given by[67]:

$$\log_{10} P = A - \frac{B}{T + C} \tag{5}$$

Where P is vapour pressure, A, B and C are all Antoine coefficients and T is the temperature.

The oven will need to be heated until an appropriate amount of strontium atoms are aquired at the other end. Higher temperatures would mean higher velocities for the individual atoms emitted (they behave classically) which will be distributed according to the Maxwell Boltzmann distribution equation[68]:

$$P(v) = \left(\frac{m}{2\pi k_B T}\right)^{3/2} 4\pi v^2 \exp\left(-\frac{mv^2}{2k_B T}\right) \tag{6}$$

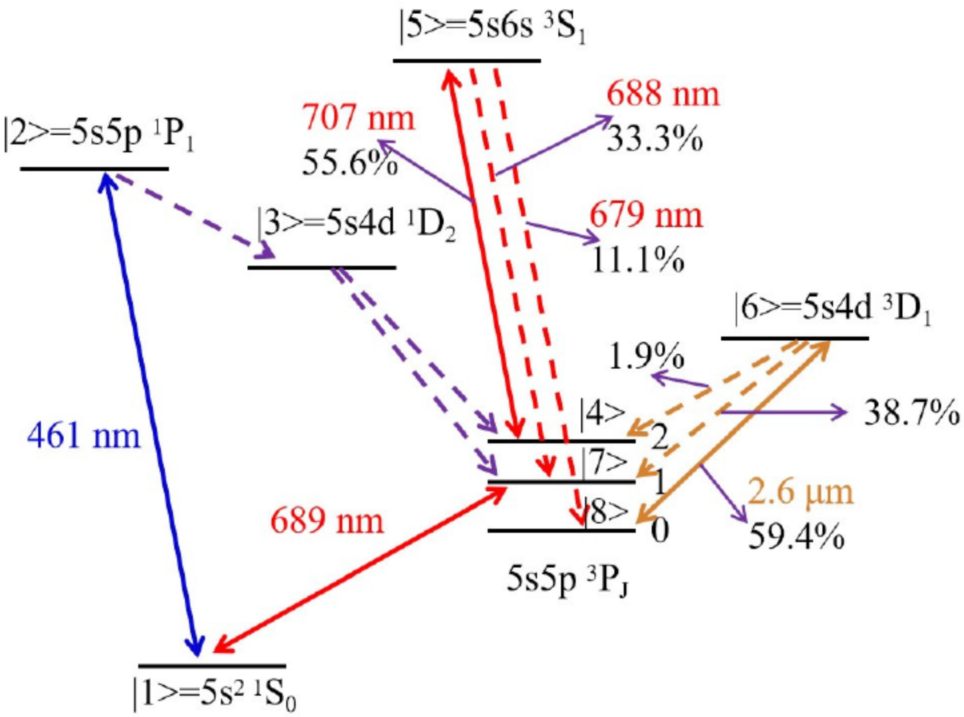

Figure 3: Diagram of electronic level structure of strontium-88[66]. The first cooling stage works on $|1\rangle \rightarrow |2\rangle$ at 461 nm. The second cooling stage works on $|1\rangle \rightarrow |7\rangle$ at 689 nm. 707 nm and 679 nm are used as repumping. However, this thesis will utilise the 707 nm and 2.6 µm ($|8\rangle \rightarrow |6\rangle$) for efficient repumping. The branching ratios of $|5\rangle \rightarrow |8\rangle\,|7\rangle\,|4\rangle$ are 11.1%, 33.3% and 55.6%, respectively, with $|6\rangle \rightarrow |8\rangle\,|7\rangle\,|4\rangle$ being 59.4%, 38.7% and 1.9%, respectively.

With $P(v)$ being the population of strontium atoms with a velocity v, m is the strontium mass, k_B is the Boltzmann's constant, T is the temperature of the oven. Since the velocities will be spread out then not every atom will be on resonance to the atomic transition. This is due to the Doppler effect given by $f = f'\left(1 + \frac{v}{c}\right)$. c is speed of light, f' is the frequency of the transition in the lab reference frame. The linewidth can be shown to be dependent on the temperature if equations 6 and the Doppler equation are combined:

$$\sigma_f = \sqrt{\frac{k_B T}{mc^2}} f_0 \tag{7}$$

The temperature of the oven in experiments is $\sim$ 830 K (560 °C) so it is expected that there will be Doppler broadening of $\approx$ 800 MHz for the $^3P_0 \rightarrow^3 D_1$ transition. Since this is a much larger number than the broadening due to LRI (a few kHz) then this broadening must be heavily reduced to get useful results.

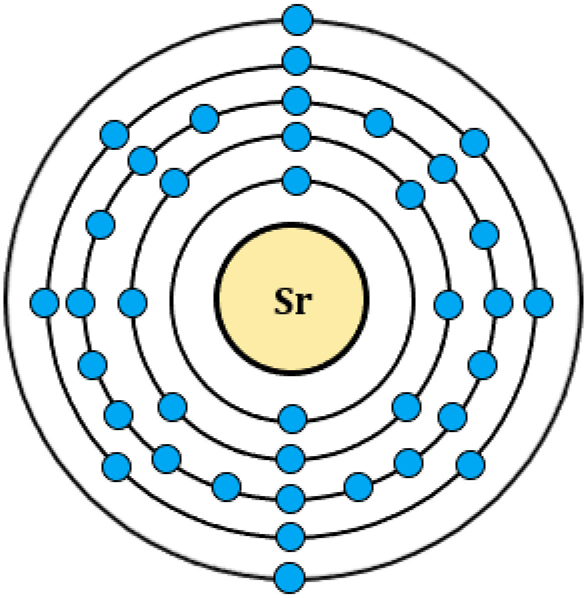

Figure 4: Electronic configuration of strontium: $1s^2 2s^2 2p^6 3s^2 3p^6 4^2 3d^{10} 4p^6 5s^2$.

2.1.2 LRI of Strontium (Sr)

Ground state strontium atoms (see Fig 4) ($5s^{21}S_0$) do not have first order dipole moments (neither magnetic nor electric) so it is able to interact with other atoms only through collisions that can be described with a Dirac delta function. LRI effects are done through coherent exchange of (virtual) photons which are provided by the abundant electronic structure of Sr. The particular transition of $5s5p^3P_0$ and $5s4d^3D_1$ corresponds to wavelength $\lambda = 2.6\mu$m and dipole moment 4.03 D. In order to realise this large dipole moment, a large lattice spacing of 412 nm is needed.

Due to the interatomic distances being small and the wavelengths being large, dipolar interaction will take place, meaning the very condition of high density needed to observe dipolar interaction will ultimately be the cause for its destruction because of the increased number of collisions. The strength of the interactions is dependent on velocity which in turn depends on the temperature. Collisions reduce the dipole interactions. To reduce collisions the MI is used to have 1 atom in 1 lattice site. With collisions reduced the dipole interactions will be dominant.

Long range interactions within strontium can be understood by looking at 1D chain of atoms that are trapped in a periodic lattice with an interatomic spacing of a (explained further in Chapter 3). When a photon excites an atom in the chain the system's evolution can be described by a master equation of a density matrix ρ:

$$\dot{\rho} = -\frac{i}{\hbar}[H, \rho] + D(\rho) \tag{8}$$

The system evolves with two components. The first term describes the conservative excitation moving along the chain and the second term is the dissipation showing the spontaneous transmission. The longer the wavelength or the smaller the interatomic spacing in the chain, the less the dissipative effect will be. If $a = 215$ nm in the transition from $^3P_0$ to $^3D_1$, the excitation lifetime is longer than the single atom's decay.

2.1.3 Bosonic Strontium

D. Yu[71] considers bosonic strontium ensemble, specifically strontium-88 atoms trapped in a 2-D blue-detuned hexagonal optical lattice with a wavelength of $\lambda_b = 412.8$ nm. It is assumed that the system is entirely in a Mott-insulator state so each lattice site only has one atom. The position of the α-th atom is given by:

$$\mathbf{r}_\alpha = \mathbf{e}_x \frac{1 - (-1)^\alpha}{\sqrt{3}} \left(\frac{\lambda_b}{2}\right) + \mathbf{e}_y \frac{2\alpha}{3} \left(\frac{\lambda_b}{2}\right) \tag{9}$$

The 2-D hexagonal lattice is chosen over 1-D lattice because the tiniest of reductions to the nearest neighbour distance can strongly increase the interatomic interactions due to dipole-dipole interactions being proportional to the 1/3 power of the separation between atoms.

The $(5s5p)^3P_0 - (5s4d)^3D_1$ transition (of wavelength $\lambda_a \simeq 2.6$ µm, the frequency $\omega_a = 2\pi c/\lambda_a$ and the spontaneous emission rate is $\gamma = 2\pi \times 46.18$ kHz), has a branching ratio just under 60% of the total decay rate of the $(5s4d)^3D_1$ state. ${}^3P_0 - {}^3D_1$ transition can therefore be approximately considered a closed atomic transition (as the ratio is greater than 50%).

2.2 Bose-Einstein Condensate

2.2.1 Achieving a BEC

An extremely important thermal phase transition[51], Bose-Einstein condensation (BEC) takes place at temperatures below what is defined as the critical temperature (also referred to as condensation temperature), T_c when bosons will accumulate in a single one-particle state, described by the condensate wave function. T_c is of the same order as the temperature which distance between particles is similar to the particles' thermal de Broglie wavelength. The de Broglie wavelength is defined by setting thermal energy equal to kinetic energy $k_bT/2 = \hbar^2k^2/2m$, where k_B is the Boltzmann constant, m is the mass of the particle and the k is the wavevector relating to the de Broglie wavelength via $k = 2\pi/\lambda_{dB}(T)$. In Fig 5 we can see how the temperature dictates the state of the bsosons' interactions with one another. As temperature, T, is high the bosons whizz around smacking into each other as if they were billiard balls, behaving classically. As the temperature drops, however, they behave a bit differently as λ_{dB} becomes closer to the spacing between bosons, so they exhibit a bit more wave-like behaviour.

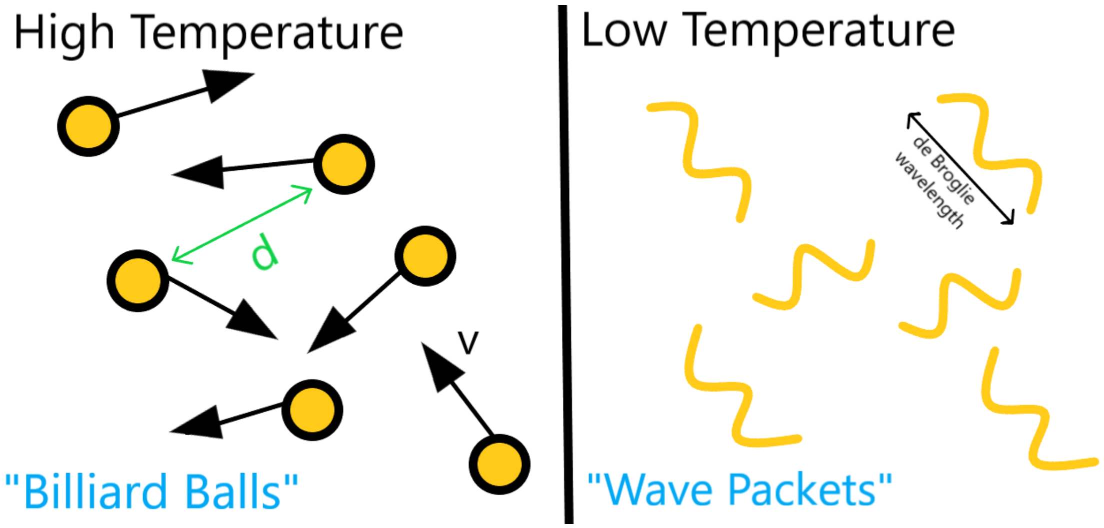

Figure 5: Left: High temperature bosons with an average separation of d collide at speed v with each other similar to billiard balls striking one another. Right: At lower temperatures, the particles behave differently as they are more wave-like. Their de Broglie wavelength is now large enough to consider them as wave packets as opposed to classical matter.

Once the temperature reaches the critical value, λ_{dB} becomes the same order as the spacing between the particles and so much more overlap occurs, as depicted in Fig 6. Once the temperature becomes cool to the point of absolute zero, all the wavelengths overlap so much that they become one giant matter wave, a macroscopic particle in effect.

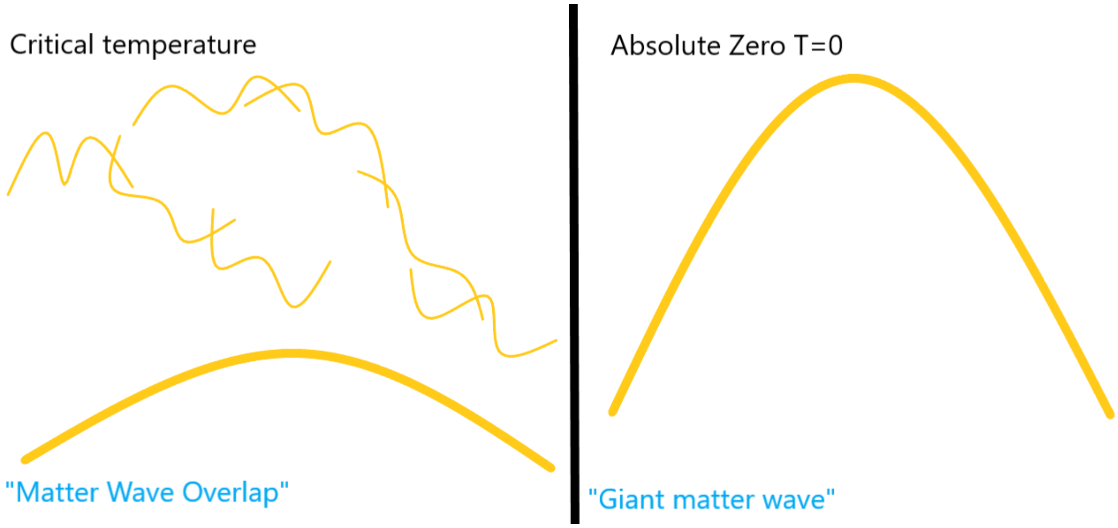

Figure 6: (Left): At the critical temperature the de Broglie wavelength is now of the same order as the separation between particles. Sufficient overlaps occur between them to consider them a matter wave. (Right): At $T = 0$ the entire ensemble of particles have overlapped to become one giant matter wave.

As identical bosons in a system have a symmetric wavefunction under exchange of the position of any two due to having integer spins, (unlike fermions that have half-odd-integer spin along with anti-symmetric wavefunctions), bosons can all occupy the same single-particle state. The transition temperature can be estimated using the following dimensional arguments. In a uniform gas of free particles, consider the mass m, the number of particles per unit volume n and Planck constant $h = 2\pi\hbar$. Using these three quantities to create a term dimensionally equivalent to energy results in $\hbar^2 n^{2/3}/m$. Then divide this energy by Boltzmann constant k and the estimate for condensation temperature T_c is:

$$T_c = C\frac{\hbar^2 n^{2/3}}{mk}$$

Where the numerical factor $C \approx 3.3$. Another way to relate the temperature of the transition to the particle density is to look at the de thermal de Broglie wavelength λ_T with the mean interparticle spacing on the order of $n^{-1/3}$. The de Broglie wavelength is defined by:

$$\lambda_T = \left(\frac{2\pi\hbar^2}{mkT}\right)^{1/2}$$

When the temperature T is big the de Broglie wavelength is small and the gas is classical. BEC in the ideal gas occurs when the temperature is low enough that $lambda_T$ becomes the same order as $n^{-1/3}$. In experiments, however, gases are not uniform due to being in a trap that usually has a harmonic-oscillator potential. If the number of particles is N then the density of the gas is given by N/R^3, R being the size of the cloud on the order of $(kT/m\omega_0{}^2)^{1/2}$,

ω_0 is the angular frequency of single-particle motion in the harmonic-oscillator potential.

By substituting the value of $n \sim N/R^3$ at $T = T_c$ into condensation temperature equation we get:

$$kT_c = C_1 \hbar \omega_0 N^{1/3}$$

Where $C_1 \approx 0.94$ is another numerical constant. Trap frequencies are typically on the order of 10^2 Hz which leads to angular frequency $\omega_0 \sim 10^3$ s^{-1}. If the number of particles lies between the range of 10^4 and 10^8 the transition temperatures will be in the range of 100 nK to a few µK.

2.2.2 Gross-Pitaevskii equation

The Bogoliubov prescription for the field operator $\hat{\Psi}(\mathbf{r}, t)$ can be rewritten as a classical field $\hat{\Psi}_0(\mathbf{r}, t)$ when considering a non-uniform interacting gas due to only considering lowest-order approximations and very low temperatures[79]. This is similar to a shift in quantum electrodynamics to a classical understanding of electromagnetism which is allowed if there are a large number of photons in the same quantum state. Since there are a large number of atoms which will occupy the same quantum state inside the BEC, the classical field is appropriate.

The field operator $\hat{\Psi}(\mathbf{r}, t)$ is given by:

$$i\hbar \frac{\partial}{\partial t} \hat{\Psi}(\mathbf{r}, t) = [\hat{\Psi}(\mathbf{r}, t), \hat{H}] = \left[-\frac{\hbar^2 \nabla^2}{2m} + V_{ext}(\mathbf{r}, t) + \int \hat{\Psi}^\dagger(\mathbf{r}', t) V(\mathbf{r}' - \mathbf{r}) \hat{\Psi}(\mathbf{r}', t) d\mathbf{r}' \right] \hat{\Psi}(\mathbf{r}', t) \tag{10}$$

The change of $\hat{\Psi} \rightarrow \hat{\Psi}_0$ can be performed if the Born approximation can be applied to the potential $V \rightarrow V_{eff}$ where V_{eff} is a soft potential that can give low-energy scattering properties like V can. Now assume that $\hat{\Psi}_0(\mathbf{r}, t)$ slowly changes over distances similar to that of the interatomic force so the variable $\mathbf{r}' \rightarrow \mathbf{r}$ to get the new equation:

$$i\hbar \frac{\partial}{\partial t} \hat{\Psi}_0(\mathbf{r}, t) = \left[-\frac{\hbar^2 \nabla^2}{2m} + V_{ext}(\mathbf{r}, t) + g \left| \hat{\Psi}_0(\mathbf{r}, t) \right|^2 \right] \hat{\Psi}_0(\mathbf{r}, t) \tag{11}$$

Here $g = \int V_{eff}(\mathbf{r}) d\mathbf{r}$. In terms of the s wave scattering length a the parameter g becomes:

$$g = \frac{4\pi \hbar^2 a}{m} \tag{12}$$

(11) is the Gross-Pitaevskii equation and the parameter $\hat{\Psi}_0$ has a similar role to that in the Maxwell equations for classic electromagnetism. The condensate wave function can be thought of as the de Broglie wavelength when approaching the classical limit.

2.2.3 Laser Cooling

This thesis utilises the phenomenon of laser cooling to help trap the Sr atomic flux beam. As mentioned in Chapter 1, laser cooling involves shining a light onto a counter propogating atom in order to reduce the speed of it. Even though a photon's momentum is not very big, the sheer number of them being absorbed and re-emitted will significantly reduce the atom's velocity given enough time. An anology often used to help imagine the event is that of throwing billions of tennis balls at a speeding train to slow it down.

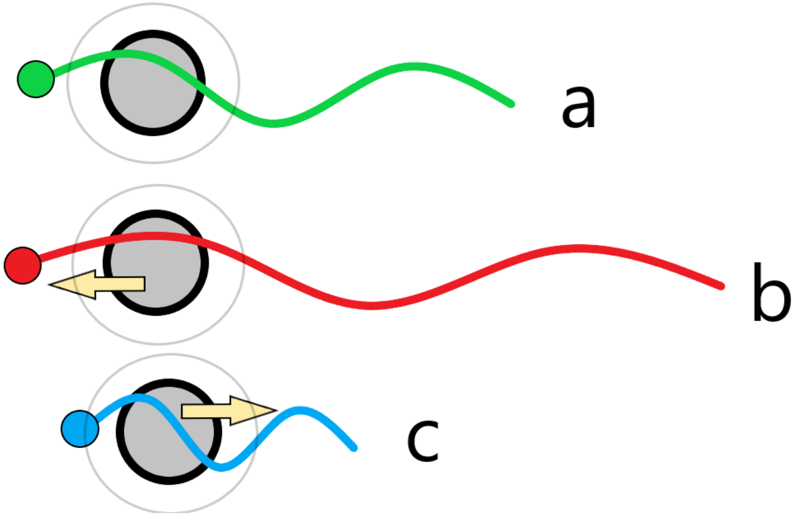

Figure 7: a) Stationary atom in lab frame sees a laser unshifted and does not absorb the photon. b) Atom is moving away from the laser and so it sees a red-shifted beam with no absorption of photon. c) The atom moves towards the laser beam and sees a blue-shifted beam that becomes on resonance with the transition and so the photon is absorbed. This momentum change causes the atom to slow down.

However, the right kind of light is needed to get this to work. The light must be of a wavelength such that when viewed from the atom's perspective, appears to be the resonant one to its' atomic transition. In Fig 7 we see the same laser light being shone on the same atom in three different scenarios. In a), the atom is stationary with respect to the laboratory reference frame and the light seen by the atom does not excite. In b) the atom moves away from the light, thus red-shifting it from its perspective and also not being absorbed by the atom. Lastly is c), where the atom is moving toward the light and blue-shifts it onto resonance with the atomic transition and thus can be absorbed.

Fig 8 shows what happens to the travelling atom after it absorbs a photon. In d) the atom's momentum is reduced from the combination of the opposing photon's momentum with its own. In e) the excited atom will emit the photon away but in a random direction, so over the course of many of these emissions the net change will be zero. Therefore the only contribution to momentum change will have been from the initial absorption of the photon

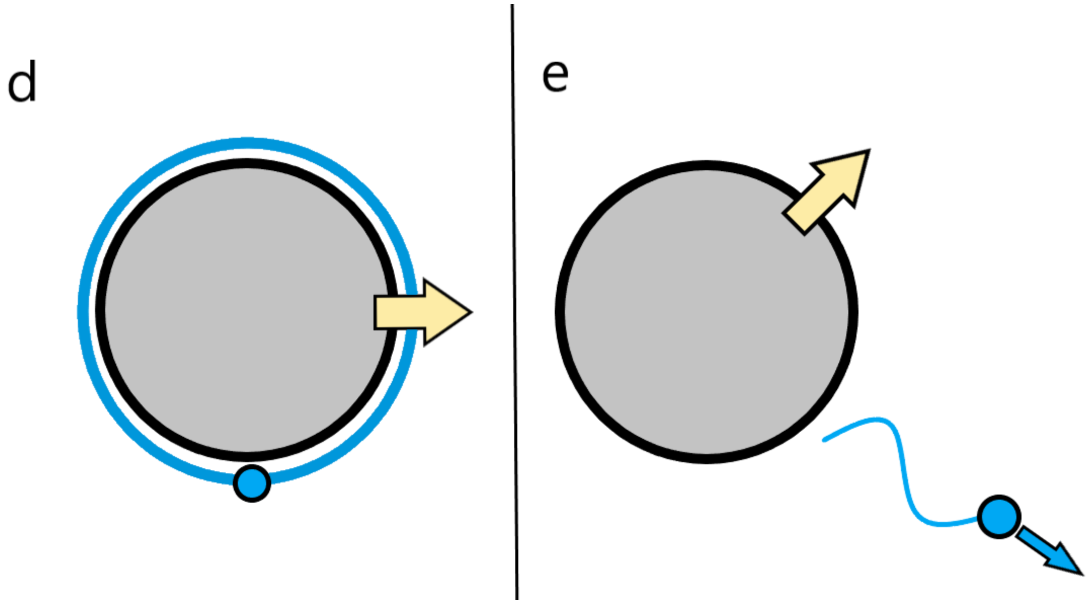

Figure 8: d) The atom moving toward the laser light absorbs the photon and its overall momentum decreases as it becomes excited. e) The atom de-excites and emits the photon in a random direction. Over the course of many of re-emissions, there will be zero net change to the momentum, so only the initial photon absorptions will be observed, thereby reducing the velocity.

and thus the atom's momentum will decrease in the axis of the beam direction.

2.2.4 Evaporative Cooling

This thesis aims to achieve LRI with Sr so it is necessary to prepare the ultracold sample in the desired state of a BEC. The experimental setup is designed with evaporative cooling in mind.

The origin of evaporative cooling comes from H. F. Hess[80] in 1986, to be used on spin polarised atomic hydrogen in order to achieve a BEC.

As mentioned earlier, laser cooling will be insufficient to get the required temperatures needed to achieve a BEC. Evaporative cooling further reduces the temperature of the ensemble of atoms by segrating the most energetic of them so the average kinetic energy of the remainder will be lower. To do this the trapped atoms potential well (Fig 10) will be gradually decreased (by reducing the intensity of the laser) so that those at the edges (i.e. highest energy) will be able to escape, drastically reducing the overall energy remaining since the atom that escapes will be at the end of the Maxwell-Boltzmann distribution (Fig Fig 11). The technique can be thought of as similar to blowing on a hot drink to reduce the temperature, after removing the hottest atoms there must be time allowed for the remainder to thermalise via collisions. In practice there are some differences than the depicted method. Instead of the potential changing the atoms leave the trap by undergoing radio-frequency transitions to untrapped states at a certain distance from the trap centre. Another thing to note is that cooling is carried out continuously rather than as a series of discrete steps.

$$\Gamma_c = \bar{n}\sigma\bar{v} \tag{13}$$

Where $\bar{n}$ is the density, σ is the cross-section and $\bar{v}$ is the average velocity. If the initial temperature of the gas is T and the target temperature is ηT, then the optimal evaporation speed must satisfy:

$$\Gamma_c\tau = \frac{\sqrt{2}e^{\eta}}{\eta} \tag{14}$$

Where τ is the length of the evaporation.

In Fig 9 the idea behind radio-frequency (RF) cooling is shown. This specific technique requires the manipulation of magnetic fields to kick out high energy atoms by flipping their spins. It is also often referred to as an RF knife as it slices the hotter atoms out of the trap. P. Bouyer[81] in 2000 used RF cooling on Rb-87 by coupling the trapping state to the non-trapping state using a radio-frequency field.

In this thesis optical evaporation will be chosen over RF cooling. This variation decreases the trap depth by ramping down the laser frequency as S. Chaudhuri[82] demonstrated in 2007. In that experiment, Rb atoms were trapped then cooled in a MOT, which was loaded from a continuous cold atom beam.

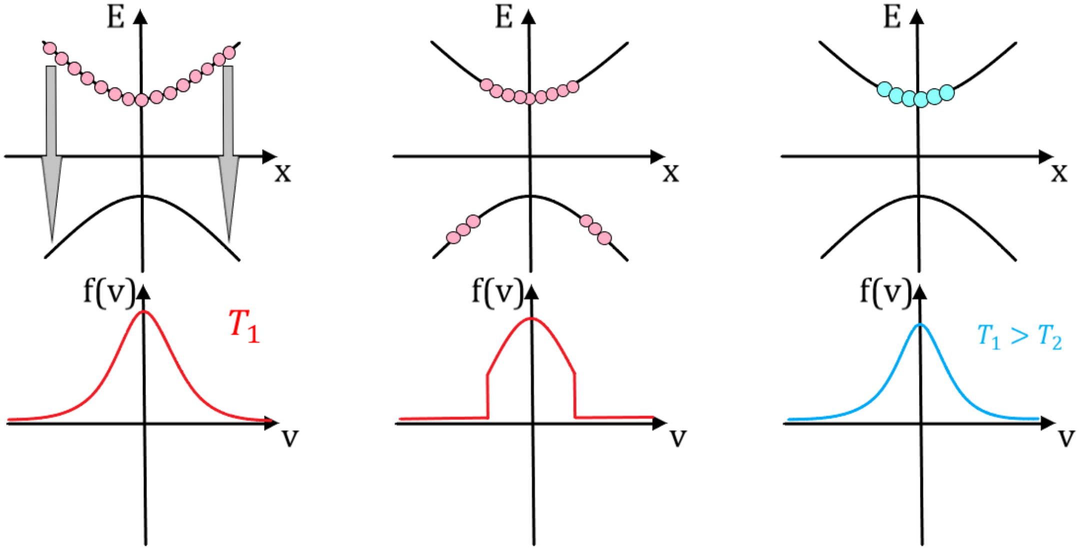

Figure 9: Forcing evaporation through the use of RF cooling. By changing the magnetic field the spin of the most energetic atoms can be flipped and thereby ejected from the ensemble trapped inside the magnetic field. The remaining atoms will then rethermalise and have a lower average temperature.

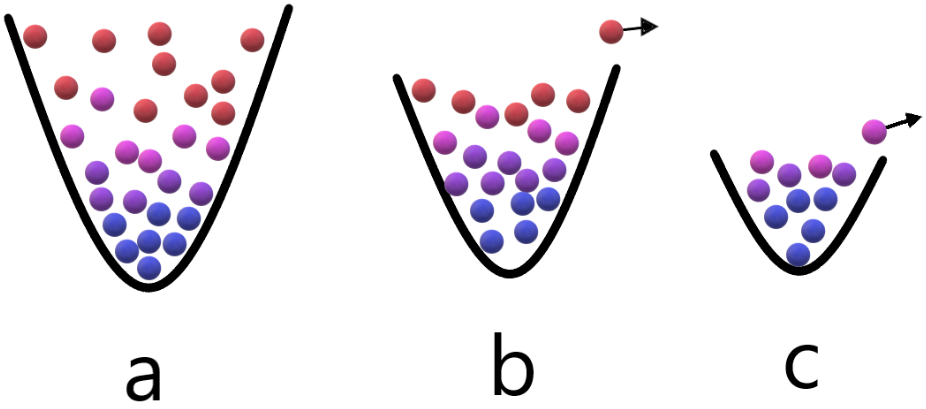

Figure 10: a) Trapped atoms in the potential well consisting of various energies. b) The trap is reduced and the highest energy atoms escape, carrying away a lot of energy with them. c) The trap is lowered even further and the remaining atoms have an overall lesser energy, thereby reducing the temperature of those remaining.

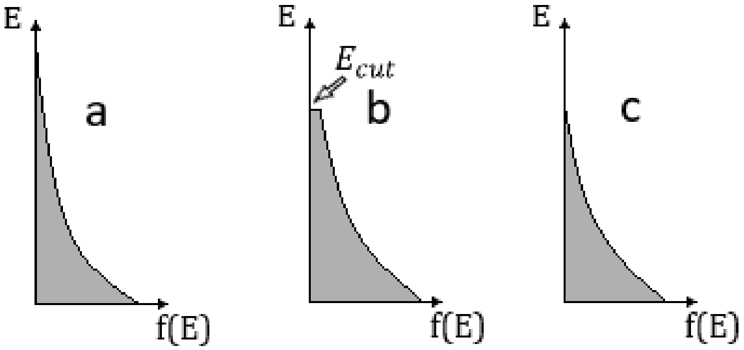

Figure 11: a) Initial Boltzmann distribution at T_1. $f(E) = \exp(-E/k_BT_1)$ b) truncated distribution after the cut, when the hot atoms have left. c) some time later after remaining atoms collide and regain a Boltzmann distribution at $T_2 < T_1$.

2.3 Strontium BEC

As mentioned earlier the Sr atoms being so close together might seem at first to promote dipole-dipole interactions but collisions with each other destroy this quickly. In order to maximise the dipole interactions they need to be placed in a Mott insulator state, a weird effect of materials that would normally have the traits of an electrical conductor but when measured they instead behave as insulators (particularly at low temperatures) due to electron-electron interactions.

When the temperature of the ensemble is low, the only parameter that is relevant is the s-wave scattering length. Looking at Table 1 it is evident due to the -2 atomic units for the elastic cross section of ^{88}Sr means it is not great at scattering photons with itself compared to the other isotopes, though it is useful for precision measurements[83]. For this reason it is preferrable to use ^{84}Sr for achieving the BEC. Ji-Cai Zhang (*et al.*)[84] investigated the elestic scattering properties of strontium atoms at ultracold temperatures. They looked at mixtures of many isotopes of Sr to obtain a large table of data, shown below in Table 1. The greatest value for s-wave scattering is a mix of ^{84}Sr+^{88}Sr which shows a scattering length of 1657 a.u., with pure ^{84}Sr being 123.

Even though the mixture of ^{84}Sr and ^{88}Sr would provide the greatest scattering length, it would mean having to set up two spearate BECs with each isotope, using one to cool the other. This would be very cumbersome and probably not necessary if only choosing one will be sufficient to demonstrate the LRI.

Table 1: Scattering parameters for different Sr isotopic combinations in units of a.u.[84]

	s-wave scattering length		Effective range	
	Quantum	Semiclassical	Quantum	Semiclassical
^{84}Sr+^{84}Sr	122.8	122.9	104.2	105.9
^{84}Sr+^{88}Sr	1656.8	1649.3	186.6	190.9
^{86}Sr+^{86}Sr	799.5	796.7	170.7	174.2
^{87}Sr+^{87}Sr	96.7	96.1	126.1	129.3
^{87}Sr+^{88}Sr	54.8	54.6	373.8	379.2
^{88}Sr+^{88}Sr	-2.01	-2.02	528997.1	538702.6

2.4 Cooling & Trapping

In this section, the idea behind trapping atoms is developed, starting with the concept of light scattering on a single atom. From the single atom then follows multiple atoms in the form of a beam that requires use of a laser to slow them down. The physics of the Zeeman slower are explained to make sure the laser has the best chance to slow the atoms via optical molasses. Only when the speed is sufficiently reduced can they then be confined to a central location in space with use of magnetic coils to form the Magneto-Optical Trap.

Conservation of momentum dictates that when radiation is absorbed by an object, there will be a momentum transfer. Since force is the same as rate of change in momentum then this will be the same as the rate at which the light imparts momentum $\hbar k$ which is also given by the energy $\hbar\omega$ divided by the speed of light c:

$$\frac{\hbar\omega}{\hbar k} = \frac{\omega}{k} = c \tag{15}$$

Radiation of intensity I will give rise to a force over an area A of:

$$F_{rad} = \frac{IA}{c} \tag{16}$$

Lasers are well-collimated single frequency light that are capable of slowing down atoms as depicted in Fig 12[86]. The size of this scattering force is equal to the product of the photon's momentum $\hbar k$ and the scattering rate R_{scatt}. From optical Bloch equations concerning the excitation of a two-level atom via radiation whilst being close to resonance on a transition which decays via spontaneous emission, it can be shown that the steady state population ρ_{22}, i.e. the fraction of atoms in level 2, is given by:

$$\rho_{22} = \frac{\Omega^2/4}{\delta^2 + \Omega^2/2 + \Gamma^2/4} \tag{17}$$

where Ω is the Rabi frequency, Γ is the decay constant and δ is the detuning. The steady state occurs when the times are greater than that of the lifetime of the upper level state ($t >> \Gamma^{-1}$). It can also be shown that as the driving fields become stronger $\Omega \rightarrow \infty$ then the population tends to balance at both levels and so leads to $\rho_{22} \rightarrow 1/2$ as the intensity increases.

The scattering rate is given by:

$$R_{scatt} = \rho_{22}\Gamma = \frac{\Gamma}{2}\frac{\Omega^2/2}{\delta^2 + \Omega^2/2 + \Gamma^2/4} \tag{18}$$

The frequency detuning δ is given by the difference of the laser frequency ω and atomic resonance frequency ω_0 when considering kv as the shift in frequency from the perspective of the atom with Doppler effect:

$$\delta_{\pm} = \omega - \omega_0 \pm kv \tag{19}$$

Using photon momentum $\hbar k$ along with the Rabi frequency and saturation intensity linked via the equation:

$$\frac{I}{I_{sat}} = \frac{2\Omega^2}{\Gamma^2} \tag{20}$$

the equation for the scattering force can be derived:

$$F_{scatt} = \hbar k \frac{\Gamma}{2} \frac{I/I_{sat}}{1 + I/I_{sat} + 4\delta^2/\Gamma^2} \tag{21}$$

Letting the intensity grow $I \to \infty$ shows the force is capped at $F_{max} = \hbar k\Gamma/2$. Spontaneous emission from both states occurs at a rate of $\Gamma/2$ due to the fact as seen earlier the population for ground and excited levels are 1/2.

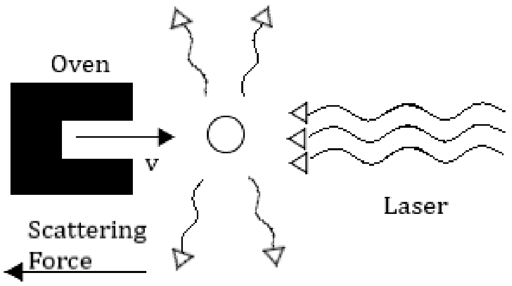

Figure 12: An atom emitted from the oven will absorb a photon which gives it a kick in the direction opposite to its motion and the scattered photons are emitted in random directions. The net effect is a force that slows the atom.

A single laser beam will slow down an atom to the point of reversing direction but if instead a pair of counter-propagating beams with a frequency red detuned from the transition could be used then the Doppler effect increases the probability of the beam interacting with the atoms from the opposing direction, which will cause them to slow down.

Fig 13 below shows a right-moving atom with two counter-propagating beams. The beam opposing the atom's motion appears to be of a higher frequency in the atom's reference frame, likewise, the beam parallel to the atom's motion is of a lower frequency. If the beam is red detuned from the resonance frequency, the counter-propagating beam is Doppler shifted closer towards the resonance, thereby increasing the probability of that beam interacting with the atom.

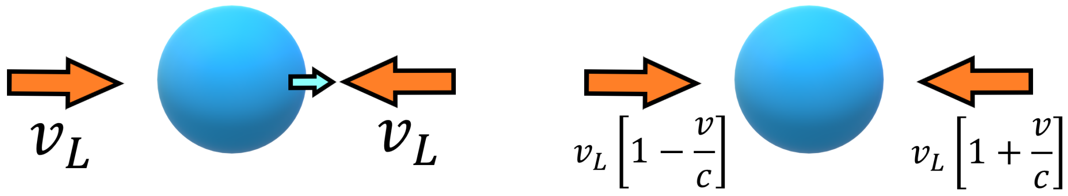

Figure 13: (Left): the atom in the laboratory reference frame. (Right): the atom's frame of reference. The beam that originates from the positive z-direction will interact mostly with the atoms situated at $z > 0$ which results in the atom being restricted to one axis.

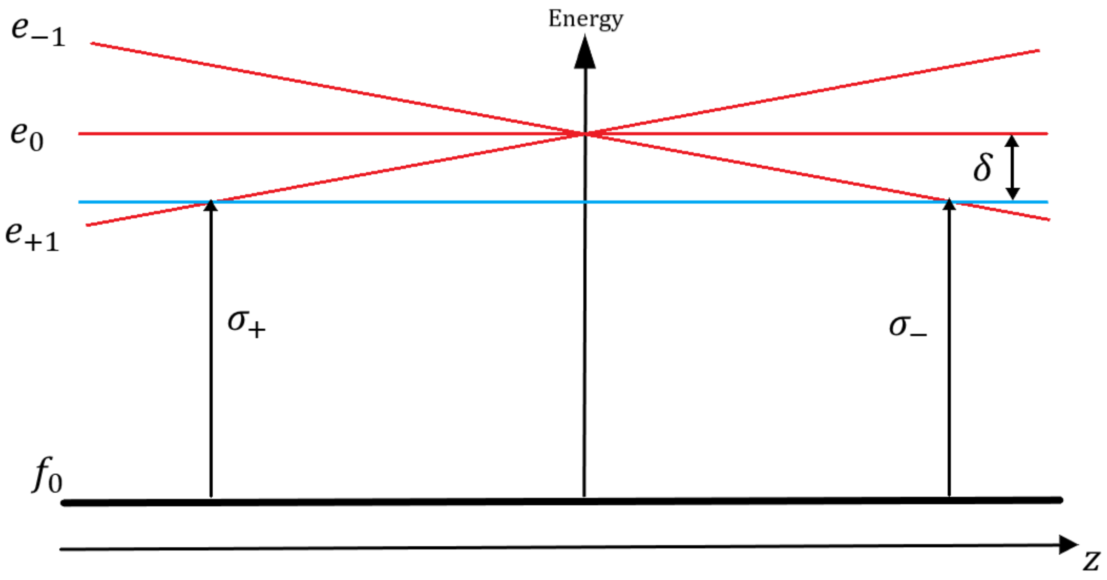

Figure 14: The effect of a magnetic field in MOT. The MOT is applied to an atom with a $J = 0$ to $J = 1$ transition. The splitting δ depends on the position. Two counter-propagating beams of circularly-polarized (σ_+ and σ_-) light hit the atom and the selection rules for transitions between the Zeeman states causes an imbalance to the radiative force from the laser beams. This effect moves the atom back towards the centre of the trap.

2.4.1 Light Matter Interaction

If a photon of wavevector k interacts with a 2-level atom that has a mass of m then the photon will provide a momemtum change of $\hbar k$ that will give rise to a recoil velocity on the atom of:

$$v_r = \frac{\hbar k}{m} \equiv \frac{h}{\lambda m} \tag{22}$$

The excited atom will eventually eject the photon in any radial direction with equal probability which will cause recoil to the atom with opposite momentum. When multiple photons in a beam undergo this interaction with the atom, the average direction for emission is isotropic, meaning there is no net change to velocity via photon emission. The only momentum change therefore would come from the initial photons absorbed by the atom, a deceleration in the direction of photons' vector $\vec{k}$:

$$\vec{a} = \frac{\vec{F}_{scatt}}{m} = \rho_{22}\frac{\hbar\vec{k}}{m\tau} = \rho_{22}\frac{\vec{v}_r}{\tau} \tag{23}$$

As seen in equation (17) ρ_{22} can be considered as the probability, P, for the atom to absorb the photon, τ is lifetime of the transition which is related to the reciprocal of decay constant Γ.

In Fig 12 the deceleration of the atom will be given by:

$$\frac{dv}{dt} = v\frac{dv}{dx} = -a \tag{24}$$

with $a > 0$.

Now let the atom be two-level with ground state $|g\rangle$ and excited state $|e\rangle$ (where g corresponds with level 1 and e with level 2 from the prior Bloch equations) with energy difference of $E_e - E_g = h\nu_0$ and consider if the atom interacts with a monochromatic plane wave with intensity of I and a frequency of ν_L. Multiplying the rate of spontaneous emissions $1/\tau$ with the probability of the excited state being filled will give the number of absorption and spontaneous emission cycles, measured in photons/second.

$$P = \frac{1}{2}\frac{\frac{I}{I_{sat}}}{1 + \frac{I}{I_{sat}} + 4\frac{\delta^2}{\Gamma^2}} \tag{25}$$

with $\Gamma = \frac{1}{2\pi\tau}$ is the natural width (in Hertz)[97].

Specifically using ^{88}Sr as the atom, with mass of $\approx$ 87.9 a.m.u and a photon on resonance with the $^1S_0 \rightarrow {}^1P_1$ transition (see Fig 15), wavelength 461 nm. By substituting these numbers into the recoil velocity equation the result is 1.5×10^{-3} m/s. The photon is re-emitted after $\approx 5 \times 10^{-9}$ s vacating the atom for another photon to enter which could lead to a deceleration of 285 km/s^2. This gives an idea of what kind of setup is needed for the main experiment in this thesis. There needs to be a 461 nm laser counter-propagating to the Sr beam but the Doppler shift needs to be taken into account. This will be combined with another device called the Zeeman Slower which will help atoms absorb the laser light over a range of speeds. This same laser light will also be used to help trap the atoms when they finally come to rest at the desired location in the centre of the MOT.

2.4.2 Zeeman Slower

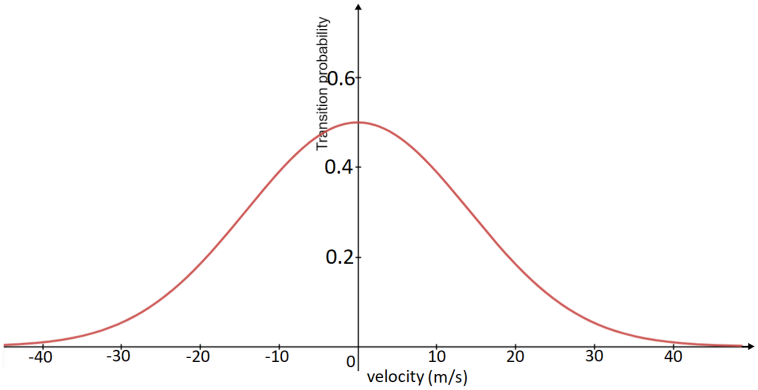

Figure 15: Transition probability vs velocity of atoms for $^1S_0 \rightarrow ^1P_1$ on Sr.

The probability of the laser interacting with an atom is dependent on its velocity, therefore only a very specific range of velocities can be retarded using a single frequency (monochromatic) beam. To slow down more atoms one can use a technique known as chirping[91], whereby the frequency of the laser is increased rapidly as the atom slows down. Another technique, power/frequency broadening involves an increase of the width of laser frequency and lastly using a magnetic field gradient along the direction of the flight path can change the frequency of the transition, which is the Zeeman slower. The Zeeman slower technique is preferred here as it gives a continuous stream of cold atoms and at low power too.

By increasing the temperature of an atomic source to > 650 K, the number of atoms in the flux will increase. The Maxwell-Boltzmann distribution of velocities in this case would suggest that only a small fraction of atoms will be directly captured inside the MOT so the Zeeman slowing method will be necessary to increase the percentage loaded within the MOT. It would be possible to also use a two-dimensional MOT but the requirements would be additional power for the lasers and a longer loading time of 5.5 s[92] in comparison to 0.5 s from a Zeeman slower[93]; factors that will affect the final number of atoms captured in a 3D MOT. The additional equipment needed for the 2D setup would introduce more complexity to the system and there would need to be realignment periodically as well[95].

The δ in (19) and (25) will change in a magnetic field to:

$$\delta = \omega - \omega_0 - \vec{k}.\vec{v} - \frac{\mu B(z)}{\hbar} = \gamma - \vec{k}.\vec{v} - \frac{\mu B(z)}{\hbar} \tag{26}$$

Where $\gamma = \omega - \omega_0$ is the gap of the laser frequency with the transition frequency. The term $\mu = (g_e m_e - g_g m_g)\mu_B$ is the transition magnetic moment, $g_{e,g}$ is the Landé g-factor for the excited and ground state whilst $m_{e,g}$ is the magnetic quantum number[94]. The maximum deceleration takes place on resonance (when $\delta = 0$). So the magnetic field will need adjusting in the parallel (z) direction to the velocity of the atom so the light stays on resonance with the transition the whole journey along the slower:

$$\delta = 0 = \gamma - \vec{k}.\vec{v}(z) - \frac{\mu B(z)}{\hbar} \longrightarrow B(z) = \frac{\hbar}{\mu}\Big(\gamma - \vec{k}.\vec{v}(z)\Big) \tag{27}$$

Therefore if the deceleration were constant:

$$B(z) = \frac{\hbar}{\mu}\left(\gamma - |k|.\sqrt{\frac{2|a|z}{m}}\right) \tag{28}$$

Now using (23) and (28), $\delta = 0$ and $P = \frac{1}{2}$:

$$B(z) = B_0 - \frac{1}{\mu m}\sqrt{\frac{\hbar^3 |k|^3}{2\tau}\frac{I/I_{sat}}{1 + I/I_{sat}}} \tag{29}$$

$B_0 = \frac{\hbar}{\mu\gamma}$ is the offset of the field which is necessary to keep the laser inside the Zeeman slower from interacting with the atoms upon exiting. If this did continue interactions then more decelerations would occur to force atoms to rest and then reverse direction and therefore will not enter the capture region.

Conventional Zeeman slowers are created with current-carrying coils with a specific winding geometry in order to get the correct spatial distribution along the atomic flow axis[96]. Later in Chapter 4 the innovative setup for the experiment will involve a robust and simple method to achieve the same effect.

If there is a gradient larger than that in (29), atoms do not have the time needed to slow down to keep resonant with the incident light. In a coil or magnet there can be imperfections which will change the profile of the field and there will also be fluctuations in the laser light beam. The Zeeman slower in the experiment therefore has a lower gradient than the one above. Atoms will interact with the laser in regions where $\frac{\vec{k}.\vec{v}+\mu Bz}{\hbar} \approx \gamma$; therefore higher veolocty atoms interact earlier than lower velocity atoms. This will compress the velocity distribution and also reduce the average speed.

2.4.3 Doppler Cooling Limit

The force from a single laser can be expressed as:

$$\mathbf{F} = \mathbf{F}_{abs} + \delta\mathbf{F}_{abs} + \mathbf{F}_{spont} + \delta\mathbf{F}_{spont} \tag{30}$$

The scattering force $\mathbf{F}_{scatt}$ is equivalent to the average of all the forces from absorption of photons. Meanwhile the average of all the forces from spontaneous emission are zero. There will be fluctuations for both of these, however, which are given by the $\delta\mathbf{F}_{abs}$ and $\delta\mathbf{F}_{spont}$ terms.

Spontaneous emission can be in any direction so the overall direction can be modelled as a random walk (Brownian motion). Over a period of time, t, the mean square velocity increases as $\overline{v^2} = R_{scatt}t \times {v_r}^2$. The number of steps N over the time period is $N = R_{scatt}t$. Considering the z-direction only gives:

$$(\overline{{v_z}^2})_{spont} = \eta {v_r}^2 R_{scatt}t \tag{31}$$

Every recoil kick will have a $\hbar k \cos\theta$ along z with the $\eta = \langle\cos^2\theta\rangle$ as the angular average, with isotropic cases $\eta = \frac{1}{3}$. The fluctuations in absorbtion come about as the atom doesn't always absorb the same amount of photons in the time t. If the scattering obeys Poisson statistics then the fluctuations about the mean have a standard deviation of $\sqrt{N}$. The 1D random walk caused by the fluctuations in absorption have a velocity spread described in (31) but lacking the η factor due to all the absorbed photons originating from the same direction:

$$(\overline{{v_z}^2})_{abs} = {v_r}^2 R_{scatt}t \tag{32}$$

So the effects via average fluctuations in the force from absorption $\overline{\delta\mathbf{F}}_{abs}$ are given for a single laser. If there are two counter propagating lasers (e.g. left and right) then the effects will likely cancel on the atom, however the fluctuations' effects are cumulative. Since the atom is just as likely to absorb a left moving photon as a right moving photon then the random walk will only be along the direction of the beams.

If an atom is moving alongside one beam and against the other then the Doppler effect would make the atom experience different forces from these beams. If the atom were stationary it would not experience this differing force from the beams. The total force from this arrangement is given by:

$$\begin{aligned} F_{molasses} &= F_{scatt}(\omega - \omega_0 - kv) - F_{scatt}(\omega - \omega_0 + kv) \\ &\simeq F_{scatt}(\omega - \omega_0) - kv\frac{\partial F}{\partial \omega} - \left[F_{scatt}(\omega - \omega_0) + kv\frac{\partial F}{\partial \omega}\right] \\ &\simeq -2kv\frac{\partial F}{\partial \omega} \end{aligned} \tag{33}$$

For this equation $kv << \Gamma$ where the velocity is low. The force in (33) can be rewritten more simply as $F_{molasses} = -\alpha v$, where α is a damping co-efficient. The light is playing the same role that a viscous fluid would, providing friction with regards to a particle travelling through it and so this phenomenon is known as Optical Molasses.

The total of the two counter propagating forces will be the overall optical molasses force $F_{molasses} = F_+ + F_-$ where each force can be expressed as[87]:

$$F_{\pm} = \pm \frac{\hbar k \Gamma}{2} \frac{S}{1 + S + [2\delta_{\mp}/\Gamma]^2} \tag{34}$$

with $S = \frac{I}{I_{sat}}$ and so the addition of these becomes:

$$F_{molasses} \cong \frac{8\hbar k^2 \gamma S v}{\Gamma(1 + S + (2\gamma/\Gamma)^2)^2} \tag{35}$$

By differentiating (21), α is also expressed as:

$$\alpha = kv\frac{\partial F}{\partial \omega} = 4\hbar k \frac{I}{I_{sat}} \frac{-2\delta/\Gamma}{[1 + (2\delta/\Gamma)^2]^2} \tag{36}$$

In this equation the term $I/I_{sat} << 1$ and so has been omitted. This is due to optical molasses being applicable only when intensity is much lower than the saturation intensity so the force from each beam is treated separately. If low intensity from the beam is assumed, there is no cause for concern regarding excitation from one beam and stimulated emission from the other beam. To damp then the $\alpha > 0 \leftarrow \delta = \omega - \omega_0 < 0$ which would be akin to a red frequency detuning. Along the z-direction, Newton's second law of motion gives:

$$\frac{d}{dt}\left(\frac{1}{2}m{v_z}^2\right) = mv_z\frac{dv_z}{dt} = v_z F_{molasses} = -\alpha {v_z}^2 \tag{37}$$

In a setup where there are x and y counterpropagating beams as well, there will be a region where all of them overlap. In this region the kinetic energy, $E_k = \frac{1}{2}m({v_x}^2 + {v_y}^2 + {v_z}^2)$ and the velocities in all directions decreases:

$$\frac{dE_k}{dt} = -\frac{2\alpha}{m}E_k = -\frac{E_k}{\tau_{damp}} \tag{38}$$

This damping time $\tau_{damp} = m/2\alpha$ can be on the order of microseconds which would be how long it takes for atoms entering the region to be cooled, provided they are travelling at speeds that can be captured via optical molasses. One problem with (38) is that it may seem that energy will eventually become zero but this is due to ignoring any fluctuations in the force which cause heating. By detuning the laser to just below the transition frequency, the laser opposing the atoms' motion will be blue-shifted with regards to the atomic rest frame whilst the laser with the motion will be red-shifted away from resonance (mentioned in Fig 13). This can be used to make atoms interact more strongly with the opposing beam and slow down even more.

Including the force arising from fluctuations into (37) and having the scattering rate from two beams being $2R_{scatt}$:

$$\frac{1}{2}m\frac{d\overline{v_z{}^2}}{dt} = (1+\eta)E_r 2R_{scatt} - \alpha\overline{v_z{}^2} \tag{39}$$

with the term E_r being the recoil energy given by:

$$E_r = \frac{1}{2}m{v_r}^2 \tag{40}$$

The equation shows how the heating and damping terms balance when considering an atom in a pair of opposing beams. However, in typical optical molasses experiments there are three perpendicular pairs of laser beams. When considering these six beams it can be assumed that scattering occurs six times faster in the overlap region compared to one beam (also neglecting saturation). Symmetrical configuration means stimulated emission is isotropic and so the average angle leads to $\eta = \frac{1}{3}$. The $\overline{\delta\mathbf{F}}_{spont}$ is 3 times greater than two beams along a single axis so $1+\eta \to 1+3\eta = 2$ for this case. Therefore the kinetic energy from scattering becomes twice that of the recoil $2E_r$.

Setting the time derivative of (39) to zero leads to the six beam setup becoming:

$$\overline{v_z{}^2} = 2E_r\frac{2R_{scatt}}{\alpha} \tag{41}$$

Equipartition theorem leads to the energy relation $\frac{1}{2}m\overline{v_z{}^2} = \frac{1}{2}k_BT$ along the z-direction for kinetic and thermal energy. By inputting for α and R_{scatt}:

$$k_BT = \frac{\hbar\Gamma}{4}\frac{1+(\frac{2\delta}{\Gamma})^2}{\frac{-2\delta}{\Gamma}} \tag{42}$$

A minimum for this function occurs at the value $\delta = \omega - \omega_0 = -\frac{\Gamma}{2}$ where:

$$k_BT_D = \frac{\hbar\Gamma}{2} \tag{43}$$

This T_D is the lowest temperature possible from the optical molasses method and the equation itself is the Doppler cooling limit. If applying to strontium it can reach just 110 µK when using a 461 nm laser.

2.4.4 Magneto-Optical Trap

Beyond slowing down atoms in an optical molasses setup, the next step is to confine the atoms with a magnetic field gradient. Two coils with opposite direction currents can produce a quadrupole magnetic field but this alone is not sufficient to trap. The existence of this quadrupole magnetic field creates an imbalance in the scattering forces from the lasers. The radiation force from the side with the stronger laser is what actually traps the atoms. Fig 16 shows the effect on this special magnetic field shape. Fig 14 shows how the MOT is meant to work over a $J = 0$ to $J = 1$ transition as the centre of the coils has both fields opposed and symmetric so the field is $B = 0$. The field changes linearly short distances away from this null region.

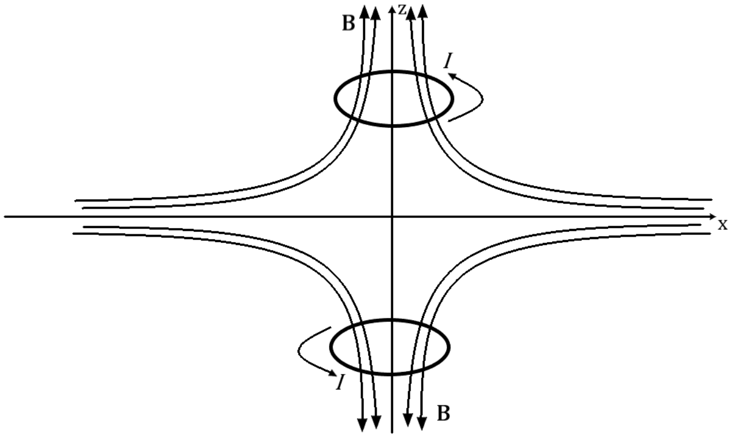

Figure 16: Two coils that have currents flowing in opposite directions which produce a quadrupole magnetic field. At the centre region the field is zero and the magnitude increases linearly for all directions at small distances from the centre.

Going back to ${}^1\mathrm{S}_0 \rightarrow {}^1\mathrm{P}_1$ transition, if a linear magnetic field $B_z = B_0 z$ is active, the Zeeman effect will split the ${}^1\mathrm{P}_1$ state into sub-levels, depicted in Fig 14. If the two counter-propagating beams have opposite circular polarisation and red detuning, the beam originating from the positive z-direction will interacting mostly with the atoms situated at $z > 0$ and vice versa. The result of this is the atoms are restricted to the one axial direction.

2.4.5 Repumping laser

The ${}^1\mathrm{P}_1$ state is not guaranteed to decay back to ground state. Fig 3 shows how this state can also decay to the ${}^1\mathrm{D}_2$ state with a probability close to 1/12000. At this point an atom will either go to the ${}^3\mathrm{P}_1$ state with a probaility of $\frac{2}{3}$ or the ${}^3\mathrm{P}_2$ with probability $\frac{1}{3}$. Should the atom go to ${}^3\mathrm{P}_1$ it will have a lifetime of 21 µs before going back to ${}^1\mathrm{S}_0$ where it repeats the cycle. The ${}^3\mathrm{P}_2$ state, however, is much more long lived with a lifetime of 120 s meaning these atoms will not be going back to the MOT, so this calls for intervention via repumps. The atoms in this longer lifetime state can be sent to the 5s4d${}^3\mathrm{D}_2$ state with the use of a

3µm laser. From here the atoms will decay most likely to the $^3P_1$ state and some back to $^3P_2$. This is difficult to pull off due to the scarcity of such lasers for commercial use.

Atomic clocks make use of a 707 nm laser to pump the $^3P_2$ to the $5s6s^3S_1$ state where the atom can decay back to any of the $5s5p^3P_J$ states. Whilst 55.6% will return to the $^3P_2$ to be repumped again, the remaining two states will have probability 33.3% for $^3P_1$ and 11.1% for $^3P_0$, with a ratio of 3:1 for re-entering the cycle. The atoms entering $^3P_0$ can be pumped back to $^3S_1$ with the aid of a 679 nm laser so no atoms are lost.

The 679 nm laser can be swapped for the 2.6 µm clock laser which makes use of the clock transition, $^3P_0 \rightarrow ^3D_1$. From this state the atoms will decay to the ^3P_J manifold with probabilities 1.9%, 38.7% and 59.4% for J=2, 1 and 0 respectively. This is the chosen transition for this thesis due to its necessity in observing long range interaction. Later in this thesis the 707 nm and 2.6 µm lasers will be shown as a part of the final setup.

2.4.6 Red MOT

This specific technique first came about from H. Katori in 1999[88] who experimented with ^{88}Sr and then with ^{87}Sr[89] in 2003. Sometimes this second cooling stage may be called a “narrow-line MOT”, its purpose being to reduce temperature and increase the density (phase space) of the ensemble.

In the case of strontium-88 the 461 nm laser will allow the formation of the blue MOT with axial field gradient 50 G/cm[90] through the transition $^1S_0 \rightarrow ^1P_1$ which keeps atoms in the mK regime. After this pre-cooling stage the trapped atoms must then be transferred over to the red MOT using the $^1S_0 \rightarrow ^3P_0$ transition at 689 nm to push them into the colder µK regime (Fig 49 shows the timings). This is done by quickly reducing the field gradient to 3 G/cm whilst also red-detuning and broadband frequency modulating the 689 nm laser (to obtain a broadband red MOT). This transition has a linewidth of $\frac{\Gamma}{2\pi} = 7.5$ kHz and $I_{sat} = 3$ µW/cm^2. 10 ms afterwards the atomic cloud can be shrunk by changing the field gradient linearly to 10 G/cm over the course of 50 ms. The 689 nm laser will be broadened during this time to capture the atoms with velocities ranging over their Doppler profile so that after the 60 ms has passed the 689 nm laser is no longer frequency modulated and the broadband red MOT now becomes a single-frequency red MOT.

2.5 1D Lattice Trap

The experimental setup on the lab bench is that of a blue MOT; this section is to introduce the idea behind how the Sr atoms may be trapped in much cooler 3D optical lattices. The goal is to place the Sr atoms into a BEC through use of a 1 micron laser for evaporative cooling and a crossed dipole trap with 2 beams.

2.5.1 Dipole potential

An optical lattice confines the atoms with the electric field of a laser and the resulting induced electrical dipole of the atoms. Using a far-detuned laser, the resulting trap will be weaker than that of a MOT, but the optical excitation is able to stay low. Given the right setup, a conservative potential can be created that is insensitive to the internal state of the atoms. Therefore, the far detuned optical lattice makes for a good way to study the atom's internal state.

By considering the atom as a classical oscillator,[98] an atom placed in an oscillating electric field $E(r,t) = \hat{e}E_0 e^{-i\omega t} + c.c.$ (a laser beam) will experience an induced dipole moment $p(r,t) = \hat{e}P_0 e^{-i\omega t} + c.c.$. Electric field and polarizability are related by:

$$P_0 = \alpha E_0 \tag{44}$$

with α is the complex polarisability, dependent on the electric field's frequency, ω. The induced polarisability then creates an interaction with the electrical field and atom:

$$U_{dip} = -\frac{1}{2}\langle pE\rangle = -\frac{1}{2}\mathrm{Re}(\alpha)\langle E^2\rangle = -\frac{1}{2\epsilon_0 c}\mathrm{Re}(\alpha) I \tag{45}$$

$\langle\ \rangle$ represents the time average, $I = 2\epsilon_0 c\left|{E_0}^2\right|$ is the intensity of the electrical field.

This leads to a dipole force given by:

$$F_{dip}(r) = -\nabla U_{dip}(r) = -\frac{1}{2\epsilon_0 c}\mathrm{Re}(\alpha)\nabla I(r) \tag{46}$$

The power absorbed is given by:

$$P_{abs} = \langle \dot{p}E\rangle = \frac{\omega}{\epsilon_0 c}\mathrm{Im}(\alpha) I \tag{47}$$

Scattering rate is:

$$\Gamma_{abs}(r) = \frac{P_{abs}}{\hbar\omega} = \frac{1}{\hbar\epsilon_0 c}\mathrm{Im}(\alpha) I(r) \tag{48}$$

The Lorentz's model[99] of a classical oscillator leads to the equation:

$$\alpha = 6\pi\epsilon_0 c^3 \frac{\delta/{\omega_0}^2}{{\omega_0}^2 - \omega^2 - i(\omega^3/{\omega_0}^2)\Gamma} \tag{49}$$

Where ω_0 is the frequency of the transition, ω the frequency of the electric field and Γ the spontaneous decay rate.

Now substitute α in the interaction potential and power equation to get:

$$U_{dip}(r) = \frac{3\pi c^2}{2{\omega_0}^3}\frac{\Gamma}{\Delta}I(r) \tag{50}$$

$$\Gamma_{abs}(r) = \frac{3\pi c^2}{2\hbar{\omega_0}^3}\left(\frac{\Gamma}{\Delta}\right)^2 I(r) \tag{51}$$

$$\hbar\Gamma_{abs} = \frac{\Gamma}{\Delta}U_{dip} \tag{52}$$

with $\Delta = \omega - \omega_0$ being the detuning. Red detuning of light , $\Delta < 0$, leads to a negative potential (attraction) with the atom in the maximum intensity whilst for blue detuning, $\Delta > 0$, a repulsive potential (positive) is obtained and the atom is in the minimum intensity. The dipole potential changes with $\frac{\Gamma}{\Delta}$ but the scattering rate changes with $\frac{\Gamma}{\Delta^2}$. This means a largely detuned laser with high intensity can be used to keep scattering low.

2.5.2 Multi-level atoms

Real atoms used in experimentation have a more complicated electronic transition. The dipole potential generally depends on the specific sub-state of the atom. Multi-level atoms can be described with state-dependent atomic polarizabilities.
The polarizability of a state a, frequency ω_0 is given by:

$$\alpha_a = \frac{2}{\hbar}\sum_k |d_{ak}|^2 \frac{\omega_{ak}}{{\omega_{ak}}^2 - \omega_0} \tag{53}$$

with ω_{ak} being the frequency of transition from state a to the state k. d_{ak} is the dipole matrix element:

$$|d_{ak}|^2 = \frac{6\pi\epsilon_0\hbar c^3}{2{\omega_{ak}}^3}\Gamma_{ak} \tag{54}$$

Directly measuring the transition rate is hard so an alternative is to calculate the total decay rate via the state lifetime $\tau_a = \frac{1}{\Gamma_a}$. Now (53) can be rewritten as:

$$\alpha_a(\omega) = 6\pi\epsilon_0\hbar c^3 \frac{\omega_{ak}}{({\omega_{ak}}^2 - \omega_0){\omega_{cm}}^3} b_{ak} b_{M_{ak}} \Gamma_a \tag{55}$$

with b_{ak} being the branching ratio for transition rates bewteen the fine structure states. $b_{M_{ak}}$ is the normalised branching ratio. ${\omega_{cm}}^3 = \sum_n b_n {\omega_n}^3$ is the centre of mass frequency. $b_{M_{ak}} = 1$ for linearly polarised light.

2.6 3D Optical Trap

Light and matter interactions have resulted in the developments of techniques useful in many scientific fields. Light can be used to transfer momentum to particles on the microscopic scale and below which is useful way to manipulate them[100]. The earliest known use of a technique called optical tweezers (OT) was discovered by A. Askin[101], who along with others[102] managed to trap a single microscopic particle in three dimensions using a tightly focused laser beam.

2.6.1 Higher-dimensional lattices

These higher dimensional lattices can be realised with more than two beams superimposed with differing wave vectors[103]. Let ω be the frequency of linearly polarized beams which leads to electric field being:

$$\varepsilon = \sum_i \varepsilon_i \text{cos}(q_i.r - \omega t + \delta_i) \tag{56}$$

with δ_i being the phases. The square of the electric field, averaged over one period of the oscillation is:

$$< \varepsilon^2 >_t = \frac{1}{2} \sum_i \varepsilon_i^2 + \sum_{i<j} \varepsilon_i.\varepsilon_j \text{cos}[(q_i - q_j).r + \delta_i - \delta_j] \tag{57}$$

To get a potential that is periodic in two dimensions requires minimum two independent values of $q_i - q_j$, so three values of q_i are necessary (three interfering beams). As an example, three beams in a plane and all at 120°to one another generates a two-dimensional triangular lattice.

It can be easier to use more beams to create an optical lattice. Consider two pairs of linearly polarized, counter-propagating beams in the x and y directions. If both the x polarizations are the same and the y polarizations are the same but orthoganal to x then the resulting potential energy becomes $\propto \cos^2(qx) + \cos^2(qy)$, as the product $\varepsilon_i.\varepsilon_j$ is non-zero only for a pair of beams propagating along the same axis.

Such a potential makes up a square lattice, which has a lattice constant of $\pi/q = \lambda/2$. If a z-directional beam is added that is polarized and orthogonal to the other beams, a three dimensional simple cubic lattice potential.

2.6.2 Optical lattice laser

M. Takamoto alongside Katori in 2005 trapped atoms in optical lattices for the purpose of being quantum references. In order to have an accurate atomic clock, there must be no external influence on the measurement of atomic resonance $\Delta\nu$ at transition frequency ν_0. The fractional instability $\sigma_y(\tau)$ can be used to see how the clock performs, minimised by repeated measurements of the high-Q ($Q = \nu_0/\Delta\nu$) transition. Fractional instability is approximated using the Allan deviation:

$$\sigma_y(\tau) \approx \frac{\Delta\nu}{\nu_0\sqrt{N\tau}} \tag{58}$$

Here, N is the total number of oscillators measured in unit time, τ is the total measurement time. Takamoto linked the equation to improving the Cs (caesium) clock by choosing a transition with higher frequency ν_0, therefore making research into optical atomic clocks necessary. The design of the trap could also lead to better stability, if the extended coherent interaction time Δt were to increase then the Fourier limit linewidth would decrease according to the relation $\Delta\nu \approx 1/\Delta t$, all leading to a higher Q-factor.

Up until that point the best trap was a Paul trap, where a single ion would be trapped in a region smaller than the transition wavelength (in the Lamb-Dicke regime) by using the zero point of an electric quadrupole field. The problem with this setup was the strong Coulomb interactions between ions meant that only one ion could be used so according to (58) the fractional instability cannot be further decreased due to tiny N. To overcome this issue, it was thought of to use neutral atoms that wouldn't experience Coulomb interactions to that degree and therefore increase the N value. Lasers interfering with one another could be setup in a spatial arrangement to produce periodic trapping potentials for ultracold neutral atoms, which is what we know as an 'optical lattice' depicted in Fig 17. Here the standing waves produced by the interfering lasers will produce wells with a width less than that of the laser's wavelength λ_L.

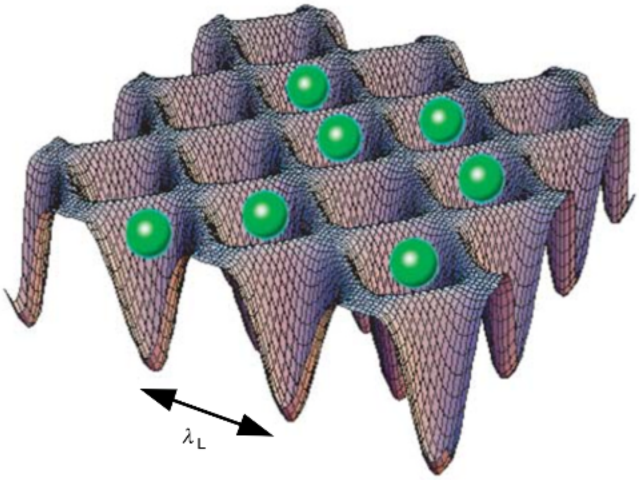

Figure 17: The lasers' interference pattern will create a lattice potential which traps atoms in a region that is even smaller than the optical wavelength λ_L.[105]

This optical lattice is able to contain atoms inside regions less than a micrometre with the periodicity leading to billions of micro-traps in a volume of 1 mm^3. Although these properties were advantageous for stability, there were issues with the lattice-trapping field modifying the atoms' internal states through a phenomenon known as 'light-shifts' (explained in Chapter 3). Only when these light-shifts could be cancelled was the idea for optical lattices further explored for atomic clocks.

The transition frequency ν of the atoms trapped in the lattice laser with an intensity of I is equal to the sum of the unperturbed transition frequency ν_0 and the light shift ν_{ac}:

$$\nu(\lambda_L, \mathbf{e}) = \nu_0 + \nu_{ac} = \nu_0 - \frac{\Delta\alpha(\lambda_L, \mathbf{e})}{2\epsilon_0 ch} I + O(I^2) \tag{59}$$

with the usual constants of ϵ_0 being permittivity of free space, c being speed of light and h is planck constant. The quantity $\alpha(\lambda_L, \mathbf{e}) = \alpha_u(\lambda_L, \mathbf{e}) - \alpha_l(\lambda_L, \mathbf{e})$ is the difference in the a.c. polarisabilities of the upper (α_u) and lower (α_l) states, both of which depend on the optical lattice wavelength λ_L and polarisation vector $\mathbf{e}$.

By making $\alpha(\lambda_L, \mathbf{e}) = 0$, the transition frequency becomes independent of the lattice laser intensity I and therefore would equal ν_0, provided the higher order $O(I^2)$ terms remain negligible.

In 2006, H. Katori[104] used standing laser radiation waves (an optical lattice) to trap Sr atoms in a periodic arrangement with dimensions being less than that of the wavelength of light. Letokhov first came up with the idea of reducing the Doppler width for the emission spectra of atoms by way of trapping them in a region of space with a size much less than the light's wavelength. Doing so would cause the Doppler broadening to be reduced strongly because of the Lamb-Dicke effect.

2011 continues Katori's[106] work on achieving an optical lattice as he reviewed the so called 'magic wavelength' that can make atomic clocks precise with measurements having $\sim 10^{-18}$ uncertainty due to states being affected by light shifts by the same amount. In this review he described how to overcome the light-shift problem in a similar way to the Takamoto[105] paper in 2005 but further expanded on this by explaining how the first atomic clocks attempted to use a 'red-detuned' magic wavelength of $\lambda_m = 813$nm from the $^1S_0 - ^3P_0$ state (ordinarily on resonance at 461 nm), which would have the effect of making the differential light shift $\Delta\nu_{ac}$ insensitive to the lattice laser frequency due to being so far off resonance:
$\frac{2\pi\Delta\nu_{ac}}{\Delta\omega_L} \approx -1 \times 10^{-9}$ for $I = 10$ kW cm^{-2}.

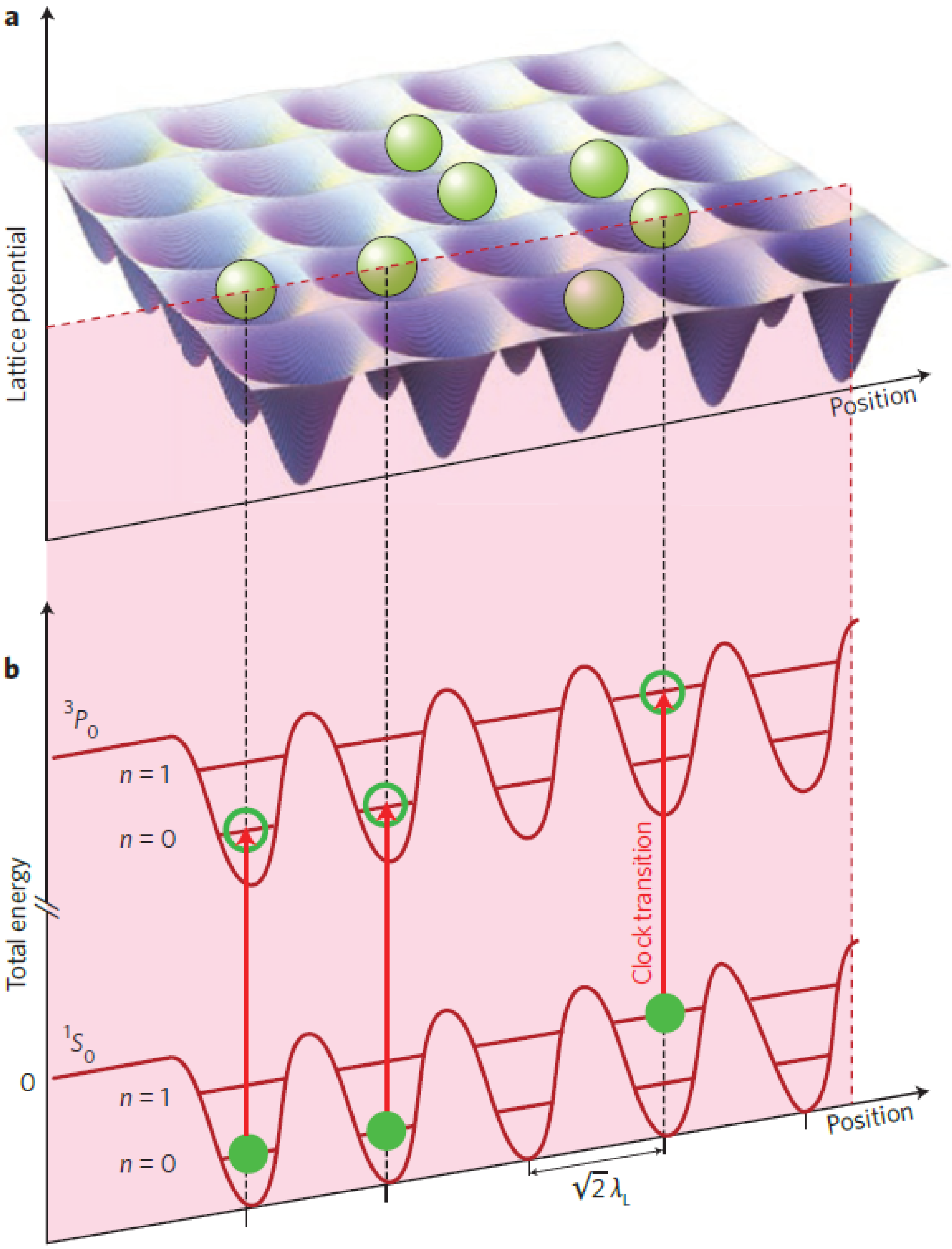

Figure 18: a) The intereference of the lasers causes potential wells with widths less than that of the wavelength of the laser light λ_L. b) Atoms can become excited from $^1\mathrm{S}_0 \rightarrow ^3\mathrm{P}_0$, the clock transition. Here the two states are equally energy shifted by the lattice potential. n denotes the vibrational states of the atoms inside the lattice potential.[106]

3 Theory

As mentioned in the introduction, the long range interaction (LRI) will be of utmost importance to the future of technological developments as well as the focus of this thesis.

3.1 Long-Range Interaction

The long-range interaction (LRI) is essential in studying the physics of condensed matter systems, with regards to strongly correlated phases of quantum matter. The previous chapter described how the conditions needed to observe this phenomenon would be achieved through use of MOTs, optical lattices and BECs, that would cool and trap the strontium atoms in a dense ensemble.

Due to Sr having two valence electrons (see Fig 4), it has a spectrum made of a series of singlet and triplet states. These two series have forbidden radiative transitions due to dipole constraints. This is very useful for technological advancements as there are consequential small transition line widths that allow for clocks and quantum processors to be made[107].

Consider starting off with Sr atoms in a Mott insulator state, and the wavelength of the lattice laser being set to $\lambda = 412.8$nm (blue-detuned magic wavelength), which leads to a lattice spacing of $a = 206.4$ nm (see Fig 19). At first, all the Sr atoms in the lattice are excited to the triplet manifold, one of which is the ^{3}P$_0$ metastable state (essentially its lifetime is infinite with regards to experiments) or the ^{3}D$_1$ state. Then the long range interaction between two Sr atoms comes about via resonant exchange of photons emitted along the ^{3}D$_1$-^{3}P$_0$ transition with a wavelength of $\lambda = 2.6$ µm.

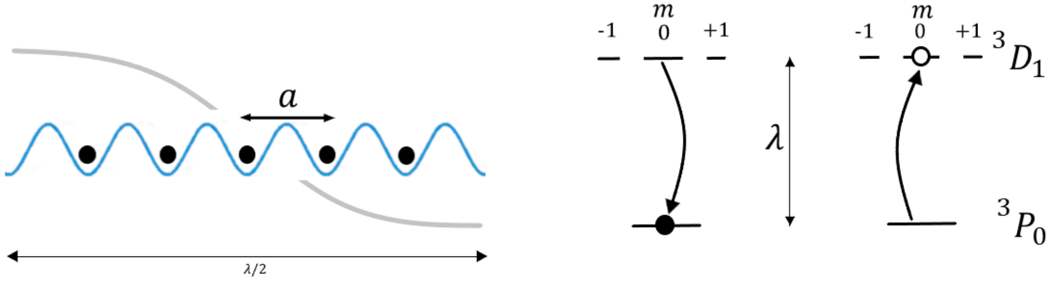

Figure 19: (Left) Atoms trapped in the optical lattice. (Right) The interaction between them is generated by the exchange of (virtual) photons on the transition between ^{3}P$_0$ and the three degenerate ^{3}D$_1$ states. λ is much larger than the typical interatomic spacing ($a = 206.4$ nm) at the magic wavelength.[107]

LRI is understood to apply only when the sample is very dense, when interatomic distances are much smaller than the wavelength of the transition. A specialised lattice setup incorporating small spacing and a long wavelength transition that Sr provides enables a platform on which to experiment with LRI whilst avoiding atomic collisions that ordinarily destructively interfere. This makes LRI itself fundamentally different to a conventional interaction where all atoms can be excited by the same laser (see Fig 2 when R is large). There is a relatively powerful dipole-dipole interaction, carrying over multiple lattice sites, when it comes to $^3\mathrm{P}_0$ metastable state and the three $^3\mathrm{D}_1$ degenerate states due to a transition dipole moment of $p = 4.03$ Debye.

3.1.1 Many-body Master equation

To begin deriving the many-body Master equation, the Hamiltonian of N Sr atoms coupled to the radiation field is needed. The vector transition operator for the k^{th} atom $\mathbf{b}_k = b_{kx}\hat{x} + b_{ky}\hat{y} + b_{kz}\hat{z}$ (position $\mathbf{r}_k$) where the transition dipole matrix elements are real and aligned along three cartesian spatial axes $\hat{x}$, $\hat{y}$ and $\hat{z}$.

The notation $b_{kj} = |P\rangle_k \langle j|$, $j = x, y, z$ where $|P\rangle_k$ represents the k^{th} atom in the $^3\mathrm{P}_0$ state and $|j\rangle_k$ the cartesian states of $^3\mathrm{D}_1$, related to the angular momentum ones $|m\rangle_k$ (with $m = -1, 0, +1$) as $|\mp 1\rangle = (\pm |x\rangle - i\,|y\rangle)/\sqrt{2}$ and $|0\rangle = |z\rangle$.

The Hamiltonian of the atomic ensemble, the radiation field (2nd term) and interaction potential (3rd term) is given by[107]:

$$H_{\text{af}} = \sum_{k=1}^{N} \hbar\omega_a \mathbf{b}_k^{\dagger}.\mathbf{b}_k + \sum_{\mathbf{q}\lambda} \hbar\omega_{\mathbf{q}} a_{\mathbf{q}\lambda}^{\dagger} a_{\mathbf{q}\lambda} + i\hbar \sum_{k=1}^{N} \sum_{\mathbf{q}\lambda} g_{\mathbf{q}\lambda} \left(a_{\mathbf{q}\lambda}^{\dagger} \mathbf{s}_k e^{-i\mathbf{q}\cdot\mathbf{r}_k} - \mathbf{s}_k a_{\mathbf{q}\lambda} e^{i\mathbf{q}\cdot\mathbf{r}_k} \right) \tag{60}$$

with $\mathbf{s}_k = \mathbf{b}_k^{\dagger} + \mathbf{b}_k$ where $\hbar\omega_a = 2\pi\hbar c/\lambda$ is the difference in energy from $^3\mathrm{P}_0$ to the degenerate $^3\mathrm{D}_1$ manifold, $\hbar\omega_{\mathbf{q}}$ is energy of a photon with momentum $\mathbf{q}$ and polarisation λ and $a_{\mathbf{q}\lambda}$ is the annihilation operator for this photon. Co-efficient $g_{\mathbf{q}\lambda} = p\sqrt{\dfrac{\omega_{\mathbf{q}}}{2\epsilon_0\hbar V}}\hat{e}_{\mathbf{q}\lambda}$, where V is the quantization volume and $\hat{e}_{\mathbf{q}\lambda}$ is the unit polarisation vector of the photon ($\mathbf{q}.\hat{e}_{\mathbf{q}\lambda} = 0$).

This leads to the Master equation[108] [109] describing the how the density matrix ρ of the atomic ensemble changes over time: $\dot{\rho} = -i/\hbar[H, \rho] + \mathcal{D}(\rho)$. The first term is dependent on the many-body Hamiltonian[107]:

$$H = \hbar\omega_{\mathbf{a}} \sum_{k} \mathbf{b}_k^{\dagger}.\mathbf{b}_k + \hbar \sum_{k \neq l} \mathbf{b}_k^{\dagger}.\overline{V_{kl}}.\mathbf{b}_l \tag{61}$$

The first term has the bare energies of the atomic levels whilst the second term describes the long-range and anisotropic dipole-dipole interaction, which is characterised by a coefficient matrix[107]:

$$\overline{V_{kl}} = \frac{3\Gamma}{4}\left\{\left[y_0(\kappa_{kl}) - \frac{y_1(\kappa_{kl})}{\kappa_{kl}}\right]\mathbf{I} + y_2(\kappa_{kl})\hat{r}_{kl}\hat{r}_{kl}\right\} \tag{62}$$

$\mathbf{I}$ is the identity matrix. $y_n(x)$ is the n-th order spherical Bessel function of the second kind. $\kappa_{kl} \equiv k_a r_{kl}$, with $k_a = \omega_a/c$ and $\mathbf{r}_{kl} = \mathbf{r}_k - \mathbf{r}_l = r_{kl}\hat{r}_{kl}$. The second term of the Master equation is dependent on the dissapator[107]:

$$\mathcal{D}(\rho) = \sum_{kl} \mathbf{b}_k.\overline{\Gamma_{kl}}.\mathbf{b}_l^\dagger - \frac{1}{2}\{\mathbf{b}_k^\dagger.\overline{\Gamma_{kl}}.\mathbf{b}_l, \rho\} \tag{63}$$

$$\overline{\Gamma_{kl}} = \frac{3\Gamma}{2}\left\{\left[j_0(\kappa_{kl}) - \frac{j_1(\kappa_{kl})}{\kappa_{kl}}\right]\mathbf{I} + j_2(\kappa_{kl})\hat{r}_{kl}\hat{r}_{kl}\right\} \tag{64}$$

The coefficient matrix Γ_{kl} describes the dissipative couplings among the atoms, $j_n(x)$ represents the n-th order spherical Bessel function of the first kind. The coherent and dissipative dynamics are very closely intertwined as they both come from the emission and absorption of photons. Since the wavelengths of the photons is long and the seperation is small, the coherent interaction is a lot stronger than the dissipation. Start by comparing the coherent interaction V_{12} to the dissipative rate Γ_{12}, with two atoms separated by distance d with induced dipoles aligned as $\uparrow\uparrow$. If $d = a$ then the ratio of $\frac{V_{12}}{\Gamma_{12}} \approx 5.7$. However, when the dipoles are aligned as $\rightarrow\rightarrow$ the ratio becomes 13.9, implying the Sr lattice setup is good for exploring many-body physics.

3.1.2 Light Shift

Fig 20 shows how the presence of a laser can shift the energy levels of an atomic transition but when the atom is trapped inside an optical lattice, the relative shift in energy levels of ground and excited state is zero. Using the laser wavelength as a reference λ_1 with the optical lattice laser being referred to as λ_2 we have a red-detuned optical lattice when $\lambda_1 < \lambda_2$ and a blue-detuned optical lattice when $\lambda_1 > \lambda_2$.

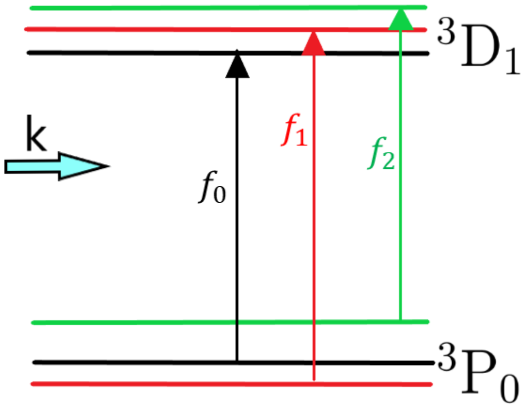

Figure 20: Black: The energy levels show the ground and excited state without any laser presence, with a transition frequency of f_0. Red: When the laser is introduced to the atom, the energy levels separate with differing amplitudes and direction, causing a new frequency transition f_1. Green: If the atom is first trapped inside of an optical lattice then when the laser causes light-shift in the energy levels, both ground and excited state shift by the same amount and direction, meaning there is no relative change to the transition i.e. $f_2 = f_0$.

Light-Shift cancellation

As mentioned earlier in Chapter 2, the optical lattice is able to use neutral atoms to allow multiple atoms to be trapped as opposed to having charged atoms trapped in magnetic fields (Paul trap). By designing the light-field potentials in a specific way, the light-field perturbations can be cancelled out. Since a single atom is confined in a trap less than the wavelength of the laser light, the first-order Doppler shift and collisional shift terms are significantly reduced, leading to a simulation of the single ion inside a Paul trap, the major difference being that millions of them can be present to improve the QPN limit by $1/\sqrt{N}$.

Generally, the electronic states of atoms trapped inside optical lattices would be energy shifted by light shifts but these can be negated with the use of the lattice field providing the exact same light shift for the two states in the transition. Equation 59 described the clock transition frequency in terms of the intensity of the laser I but in terms of the electric field E it becomes approximately (using electric dipole E1):

$$\nu(\lambda_L, \mathbf{e}_L) = \nu_0 + \nu_{ac} \approx \nu_0 - \frac{\Delta\alpha_{E1}(\lambda_L, \mathbf{e}_L)}{2h} E^2 + O(E^4) \tag{65}$$

The quantity $\alpha_{E1}(\lambda_L, \mathbf{e}_L) = \alpha_u(\lambda_L, \mathbf{e}_L) - \alpha_l(\lambda_L, \mathbf{e}_L)$ is the difference in the E1 polarisabilities of the upper (α_u) and lower (α_l) states. By manipulating the lattice wavelength λ_L and polarisation vector $\mathbf{e}_L$ in order to make $\alpha_{E1}(\lambda_L, \mathbf{e}_L) = 0$ the final observed frequency ν can equal ν_0 no matter the intensity of the laser ($\propto E^2$), provided that the higher order terms $O(E^4)$ remain negligible. The wavelength that this occurs at is called the 'magic' wavelength, λ_m.

An optical lattice configuration for the $^3\mathrm{P}_0$ state with all magnetic sublevels for the $^3\mathrm{D}_1$ state can be made by first considering a 1D blue-detuned optical lattice along the x direction. The positive frequency of the lattice field is given by[107]:

$$\mathbf{E}_b^{(+)}(x)e^{-i\omega_b t} = \varepsilon_b \left(\sqrt{\frac{2}{3}}\hat{y} + \sqrt{\frac{1}{3}}\hat{z}\right) \cos\frac{2\pi x}{\lambda_b} e^{-i\omega_b t} \tag{66}$$

ε_b is laser field amplitude, $\omega_b = \frac{2\pi c}{\lambda_b}$ is the laser frequency and c is speed of light in vacuum. Using this lattice field all of the $^3\mathrm{D}_1$ ($m = 0, \pm 1$) have the same ac polarizability $\alpha_D^b(\lambda_b)$. Using data[133] [134] [135] [136] for the electric dipole transitions pertaining to the $^3\mathrm{P}_0$ and $^3\mathrm{D}_1$, the values of ac polarizability as a function of lattice wavelength λ_b are calculated[70].

This means at a particular wavelength of light for an optical lattice, the polarizability of two atomic clock states will have the same value leading to both of them being changed by the same amount. When this happens there is no shift in the transition frequency compared to when there is not light present. The special wavelengths that satisfy the condition of no overall shift in transition are called magic wavelengths. The magic wavelength for Sr is $\lambda_{bm} \approx 412.8$ nm, the values for the polarizabilities $\alpha_P^b(\lambda_{bm}) = \alpha_D^b(\lambda_{bm}) \approx -0.76 \times 10^3$ a.u. The negative value means the atoms will be trapped in the minima of intensity for the lattice field. The 413 nm laser used in this thesis is shown in Fig 46.

3.2 Dipole-dipole interaction

A specific case for this phenomenon at high energies was explored earlier in Chapter 1 for the case of Rydberg atoms. Now the general case of two particle interaction is explored. Considering two particles 1 and 2 with dipole moments $\mathbf{e}_1$ and $\mathbf{e}_2$, with a relative position $\mathbf{r}$, the dipole interaction energy is[132]:

$$U_{dd}(\mathbf{r}) = \frac{C_{dd}}{4\pi}\frac{(\mathbf{e}_1.\mathbf{e}_2)r^2 - 3(\mathbf{e}_1.\mathbf{r})(\mathbf{e}_2.\mathbf{r})}{r^5} \tag{67}$$

C_{dd} is the coupling constant where $C_{dd} = \mu_0\mu_m^2$ for a particle that has a permanent magnetic dipole moment, μ_m, whereas $C_{dd} = \frac{\mu_e^2}{\epsilon_0}$ for a particle with a permanent electric dipole moment μ_e. μ_0 is the permeability of free space, ϵ_0 is the permittivity of free space. In a polarised setup where dipoles are aligned in the same direction (see Fig 21) z the expression becomes simplified as:

$$U_{dd}(\mathbf{r}) = \frac{C_{dd}}{4\pi}\frac{1 - 3\cos^2\theta}{r^3} \tag{68}$$

where θ is the angle between the polarisation direction and the relative position of the particles.

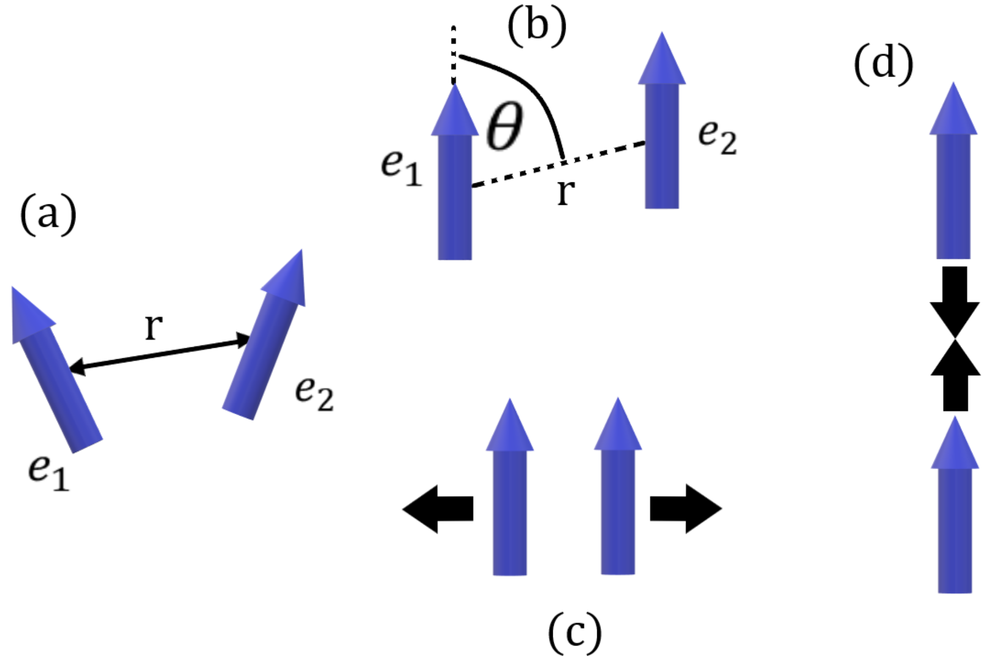

Figure 21: Two particles interacting via dipole-dipole interaction in the case of: (a) non-polarised, (b) polarised, (c) two polarised dipoles next to each other repel each other, (d) two polarised dipoles in head-to-tail arrangement attract each other.

The dipole-dipole interaction features a long range due to the $\sim \frac{1}{r^3}$ term and anisotropic characters.

Long range

Particles interacting at short range have an extensive enrgy in the thermodynamic limit whereas for long range interaction systems, the energy for one particle may only depend on the total number of particles. By considering:

$$\int_{r_0}^{\infty} U(\mathbf{r}) d^D r \tag{69}$$

where D is thr dimensionality of the system and r_0 is some arbitrary short distance cut-off. Looking at interactions that decay over large distances as $\frac{1}{r^n}$, the integral will converge for $D < n$ which implies a short range interaction. So the dipole-dipole interaction ($n = 3$) is long range in three dimensions but short range in one or two dimensions.

Anisotropy

The dipole-dipole interaction has angular symmetry of the Legendre polynomial of 2nd order $P_2(\cos\theta)$. For $0 \leq \theta \leq \frac{\pi}{2}$ the $1 - 3\cos^2\theta$ term goes from -2 to 1, therefore particles repel when they are side-by-side and attractive when head-to-tail. At the magic angle of $\theta_M = \cos^{-1}\frac{1}{\sqrt{3}} = 54.7°$, the dipole-dipole interaction disappears.

3.3 Reference Cavity

As the use of lasers will be paramount to achieve the MOT and BEC, it will also be necessary to run them for a long time, during which they must remain on resonance with as little deviation as possible. To do this effectively there must be a way to correct the frequency of a laser should it drift off target and this is where a frequency stabilisation system (FSS) will be used. The reference cavity will be the most important part of FSS, its purpose is to be a measuring stick to judge the wavelength of any incoming laser.

In the case of a resonator of length L, a standing wave can be formed only if its wavelength is an integer multiple of twice the resonator length, $2L$. Such a relation is given by:

$$nL = N\frac{\lambda_v}{2} \tag{70}$$

The constant n is the refractive index of the material in between the mirrors of the resonator, leading to the quantity nL which is the optical length of the resonator. N is an integer value called the longitudinal mode number with λ_v being the wavelength inside a vacuum. If nL were to change then λ_v changes with it which must be prevented by controlling the temperature and the refractive index. The temperature is related to thermal expansion which affects the length of the spacer whilst the refractive index can be affected by air pressure.

Let us consider first the temperature fluctuations, leading to the thermal expansion:

$$\frac{dL}{dT} = \alpha L \tag{71}$$

T being the temperature and α the coefficient of thermal expansion of the spacer. Differentiating (70) and substituting into (71) leads to a formula relating the change of resonating wavelength with the temperature change of the spacer:

$$\frac{d\lambda_v}{dT} = 2\alpha \frac{nL}{N} \tag{72}$$

As frequency, ν, is related to wavelength through $\lambda_v \nu = c_v$, where c_v is speed of light in vacuum, it is possible to take the temperature derivative and substitute into the above equation to get:

$$\frac{d\nu}{dT} = \frac{1}{2}\alpha \frac{N c_v}{nL} \tag{73}$$

The formula for fractional wavelength temperature sensitivity is given by:

$$\frac{d\lambda}{\lambda} = \alpha dT \tag{74}$$

The formula for fractional frequency sensitivity is similarly given by:

$$\frac{d\nu}{\nu} = -\alpha dT \tag{75}$$

Both of these fractional sensitivities do not depend on resonator length, wavelength nor refractive index, instead they behave similarly to the thermal expansion equation.

4 Experimental Setup

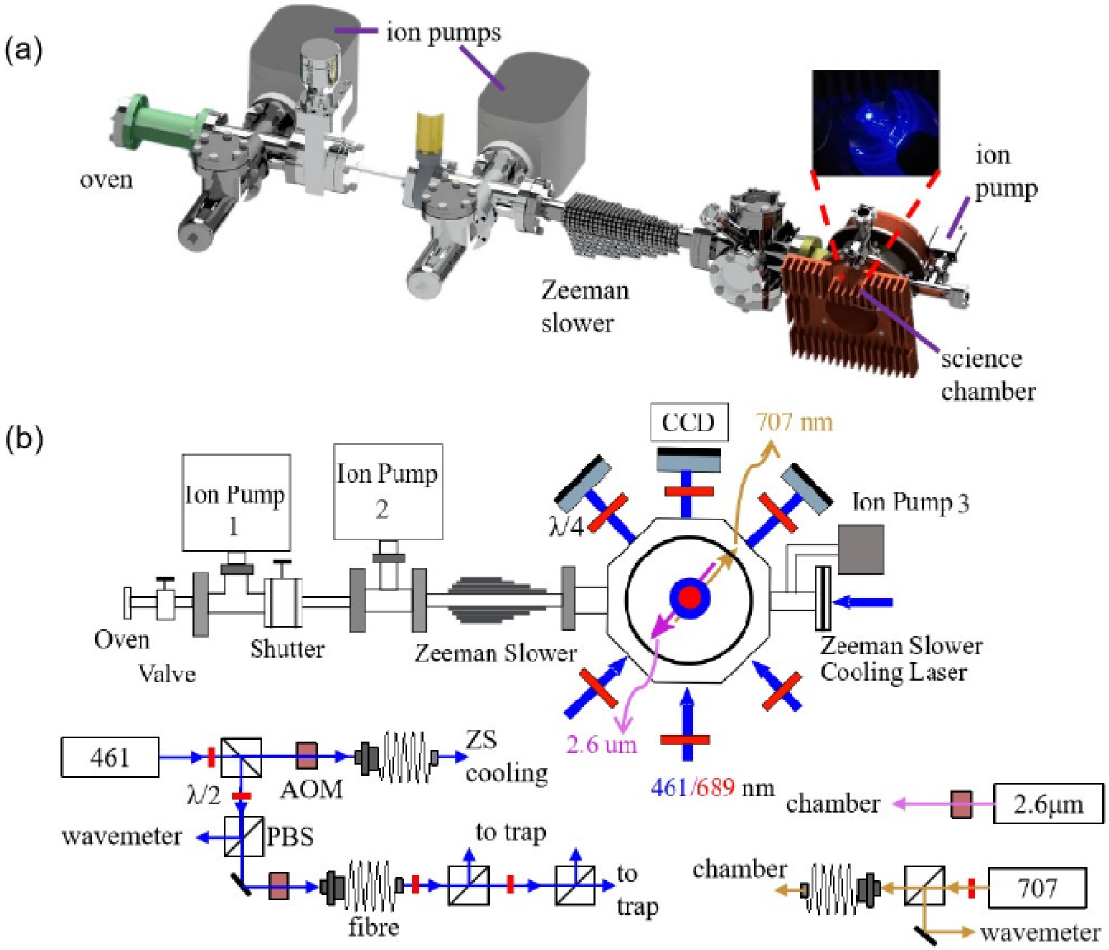

Figure 22: The experimental setup for cooling and trapping Sr atoms. (a) CAD drawing of the setup consisting of self-assembled Zeeman slower and the science chamber. Inset: a typical image of a blue MOT consisting of 9.8×10^8 atoms. (b) Schematic diagram of the experimental setup including the plan of cooling and trapping laser beams. Blue arrows represent 461 nm laser beams; The directions of 707 nm and 2.6 µm beams are pointed inward and outward, respectively; CCD, camera for taking images of atoms; 1/2, half-wave plate; AOM, acousto-optic modulator; PBS, polarization beam splitter; ZS, Zeeman slower.[66]

The entire setup for experimentation is depicted above in Fig 22 as both a CAD drawing and schematic diagram. Each individual component of the system will be explained next along with the pictures of the current iteration of the setup. Below is Fig 23 which will help with each step. (Further details found in Marco Menchetti's thesis[85]).

4.1 Vacuum System

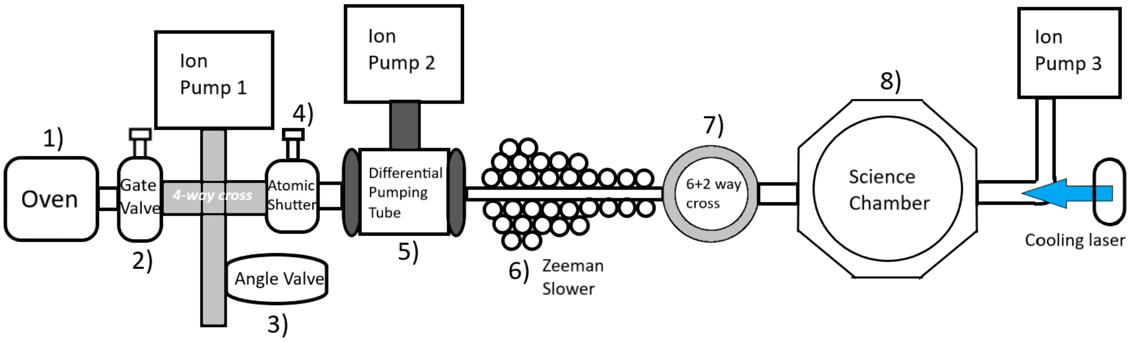

Figure 23: A drawing of the vacuum system setup assembled on the bench.

1) *Oven*: This oven (Fig 24) system design comes from the SOC 2 (space optical clock on the International Space Station) setup[19]. The strontium is kept in a stainless steel chamber before being heated (up to 560 °C) into a vapour that is funneled through capillaries forming it into a beam of around 10^{11} s^{-1} flux. It has been unchanged since before this thesis.

2) *Gate Valve*: The gate valve (Fig 25) follows the oven and controls whether the vaporised atoms can reach the rest of the system. It was installed before this thesis began.

3) *Angle Valve*: In the next stage is a four-way cross (Fig 25) connecting a 25 l/s ion pump and an angle valve to the beam. The angle valve is connected to a turbo pump for pumping down from 1 atm and the ion pumps take over from there to produce vacuum pressures in the range of 10^{-8} mbar. The pumps have been installed during this thesis, replacing the older ones.

4) *Atomic Shutter*: The atomic shutter (Fig 26) receives the collimated strontium beam before it reaches the science chamber. Turning it 90°will stop the flux. This component is unchanged since the thesis began.

5) *Differential Pumping Tube*: Immediately afterwards is the differential pumping tube (Fig 27). Its purpose is to create a pressure differential from one side of the system to the other. A second 25 l/s ion pump is used via a T-junction pipe (3-way) to the pumping tube. This is unchanged from before the thesis.

6) *Zeeman Slower*: The flux then encounters the Zeeman slower setup (Fig 28). It is comprised of an assembly of magnetic ball bearings attached to a stainless steel nipple. The magnetic field created from the outer magnet layer allows the Zeeman slower to slow down the atoms to the required trapping speed through the aid of the cooling laser. This has been broken down and reassembled many times throughout the project.

7) *8 way cross*: Exiting the slower, the beam meets the 8 way cross (Fig 29). The cooling laser at the far end of the setup will be visible here. It would be possible to setup a 2D optical molasses at this point to further confine the beam but due to the atom number being around $10^8 - 10^9$ it is not necessary. This component is unchanged from the start of the thesis.

8) *Science Chamber*: The ultimate destination of the atomic source is the science chamber (Fig 30). Here the 6 beams of the 461 nm laser form the 3D trap for the strontium. It is kept under vacuum from the final ion pump from saes group. It is a NEXTorr Z 200 model, 58 g, 57 W and side lengths 91 mm. It is capable of pumping heavy elements like N_2 at 80 l/s and lighter elements like H_2 at 290 l/s. Much of this chamber had been reconstructed towards the end of this project.

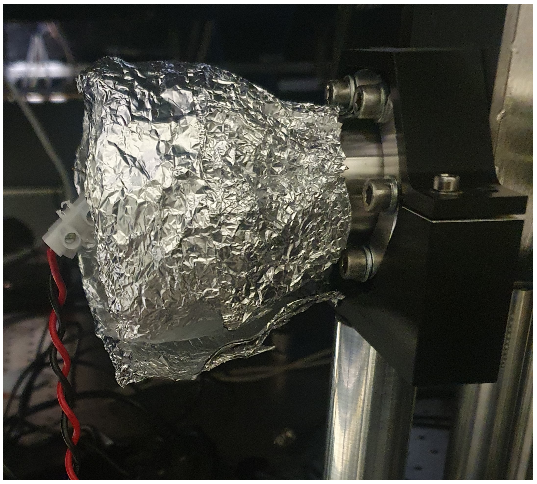

Figure 24: The strontium source encased in the ceramic heater and aluminium shielding.

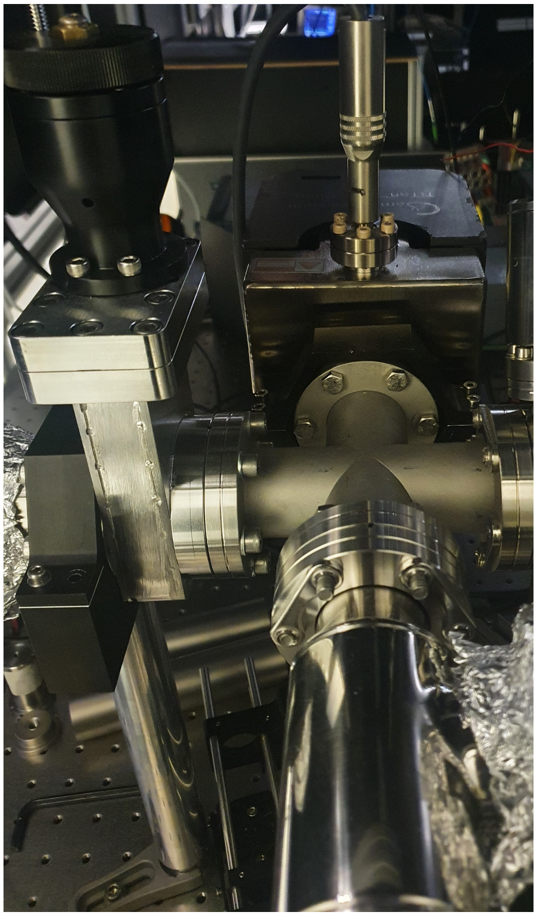

Figure 25: The gate valve, the 4-way cross, the 25 l/s ion pump and the angle valve.

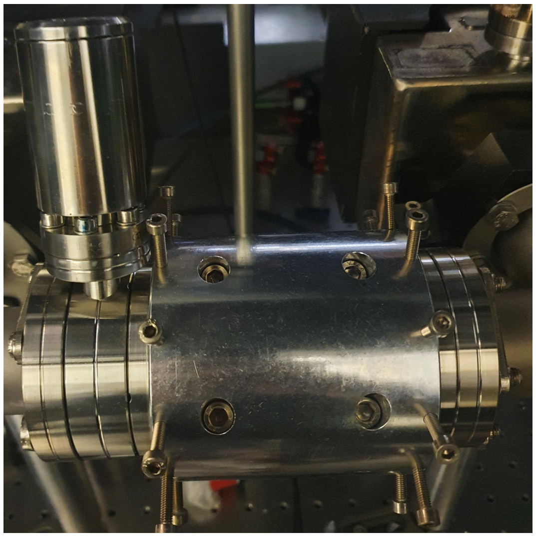

Figure 26: The atomic shutter.

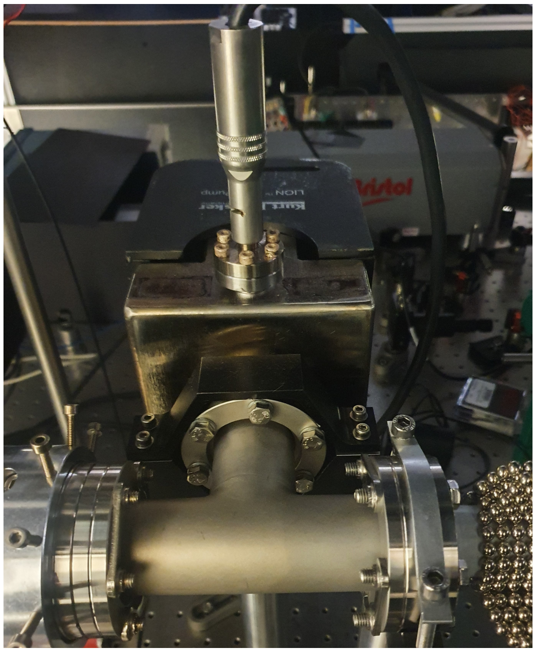

Figure 27: The differential pumping tube. It has 10 cm length and 5 mm diameter and is part of a 3-way connector with a 25 l/s ion pump.

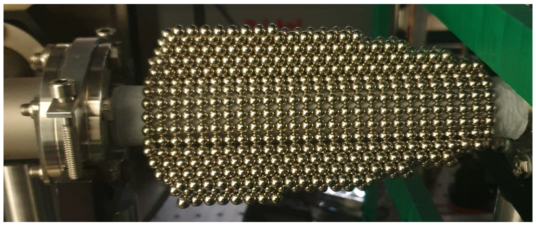

Figure 28: The cylindrical arrangement of the NdFeB magnetic balls leads to a zero magnetic radial field from the central axis. The strength of the field decreases from left to right as the number of ball bearings decreases which is suitable for the changing speed of the Sr atoms.

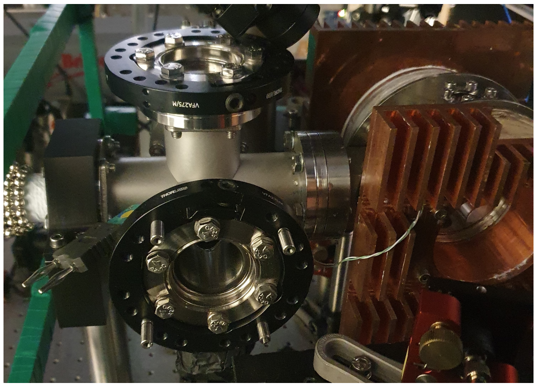

Figure 29: The 8 way cross. It has Kodial glass windows around it that provide a hermetically-sealed lens with useful transmission characteristics across a wide spectrum.

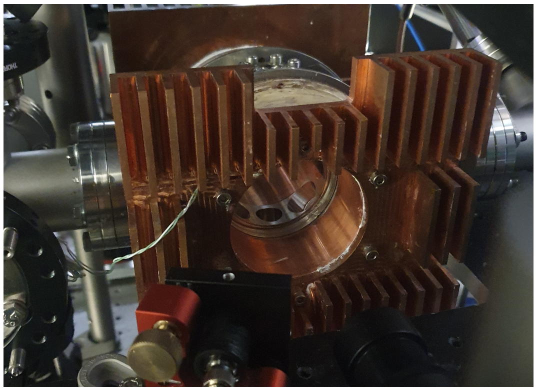

Figure 30: The science chamber. The atomic flux reaches the centre to be trapped and cooled in the MOT.

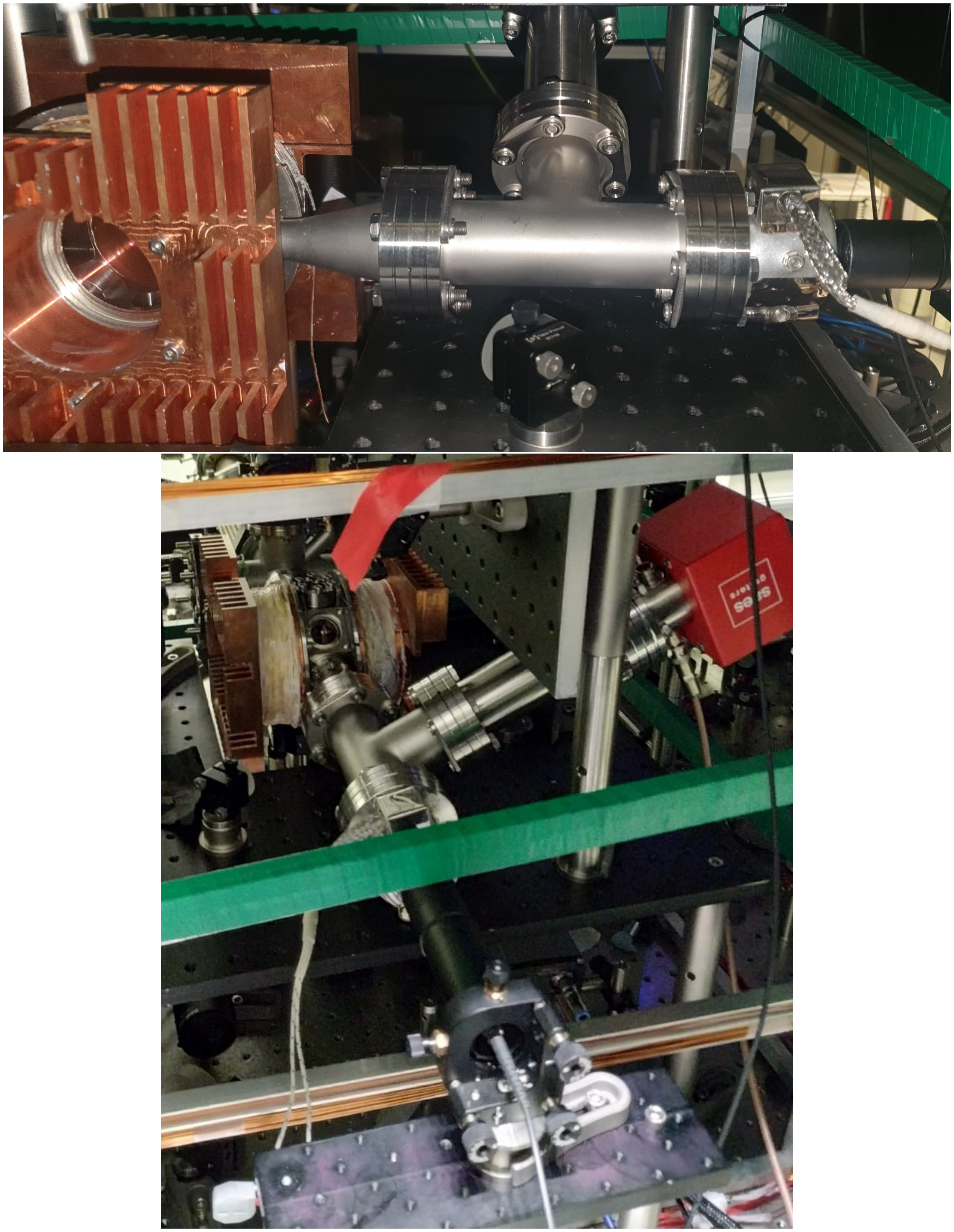

Figure 31: (Top): The 3-way T connecting to the Science chamber. (Bottom): NEXTorr Z 200 ion pump and the 461 nm Zeeman branch laser.

Motor-Valve setup

Earlier it was stated that the atomic shutter for the strontium beam needs to be manually twisted approximately 90°to go from closed position to open. Due to this manual controlling of the atomic flux into the science chamber, measuring and recording data about the strontium sample becomes unreliable as there is a significant time delay between the start of the python code and the twisting of the valve which is on the order of seconds. For this reason, a metallic sheathe was developed to fit around the exterior in which a small motor would be fitted and operated via computer, which would reduce the error caused by human operation.

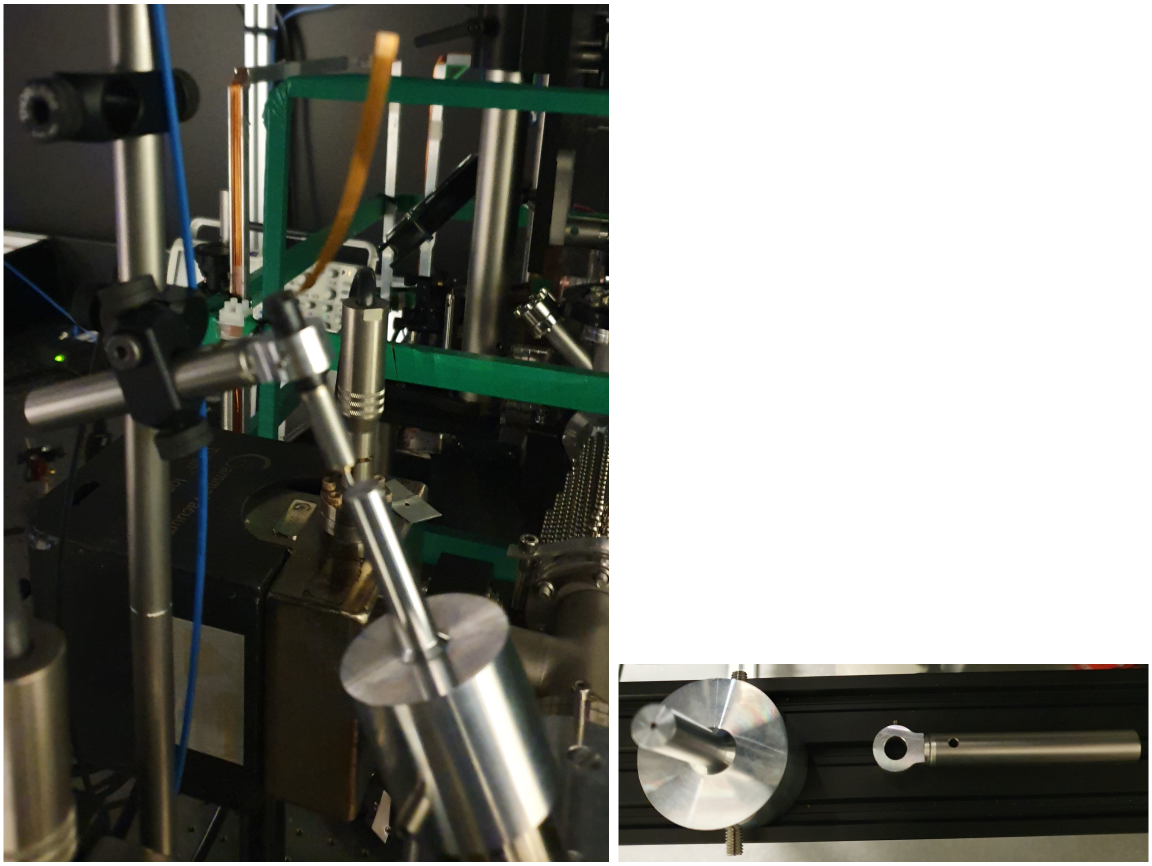

Figure 32: (Left) The motor attached to the shutter via an aluminium sheathe. (Right) The sheathe and metallic arm to hold the motor.

The motor and controller were provided by Faulhaber and work in conjunction with their software to operate it (see Fig 33[117]). The motor is Brushless DC-Servomotors Series 0824 housed in a black anodized aluminium with a nominal voltage of 6-12 V, maximum torque of 89 mNm, diameter 8mm and length 24.1 mm. The controller is part of the Motion Controllers Series MCBL 3002 F with hot-melt housing and screw terminals on the supply side and with flexboard connection on the motor side. It has a maximum continuous output current of 2 A and a peak of 3 A. The planetary gearhead comes from Planetary Gearheads Series 08/1 made from a metal and steel geartrain. It has continuous torque 60 nMn, intermittent torque 120 nMn and a length of 20.4 mm. This gives the assembly of motor and gearhead a combined 44.5 mm length as seen in Fig 34. One additional component needed was the adaptor board Accessories Series 6501.00136 that allows the whole assembly to be connected via mini USB cable.

Figure 33: (From left to right): The motion controller MCBL 3002 F. The motor 0824P012B. The planetary gearhead 08/1 gear ratio 1024:1. The adapter board MCxx 3002.[123]

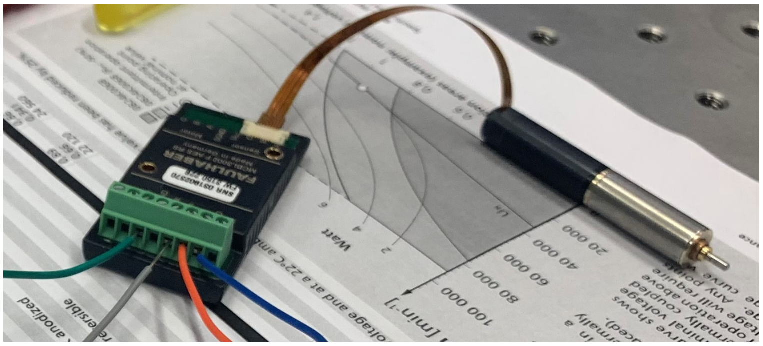

Figure 34: The planetary gearhead, motor and controller assembled together.

4.2 Magnetic Coil

4.2.1 Zeeman Slower

The Zeeman slower used in the experiment (Fig 28) is made from ball bearing magnets arranged in a hexagonal pattern[95]. The cylindrical arrangement has a net zero field along the atomic flux beam axis which can be changed with the additional fins that give it the desired magnetic field profile for slowing. This design is very easy to assemble and needs no external holder.

4.2.2 Coils

The MOT coils (Fig 35) are made using several coils of 1 mm copper filament with 330 turns. With a TTL signal, a switch between Helmholtz and an anti-Helmholtz configuration is enabled on the order of ms. Normally the coils are set to anti-Helmholtz configuration which generates about 50 G/cm of gradient near the centre. During this time the coil draws 4.5A, produces 127 W of power and stabilises at 48 °C. The external magnetic fields need to be eliminated to optimise the experiment. The compensation coils (Fig 36) used to do this are made of three pairs of coils, each having a square profile. Each coil is made with 90 turns of 1 mm copper wire, all held in position by an aluminium frame. The size and position of these compensation coils are large to allow access to the chamber and also cover a large area around the MOT. They had been installed before this thesis began by Marco Menchetti.

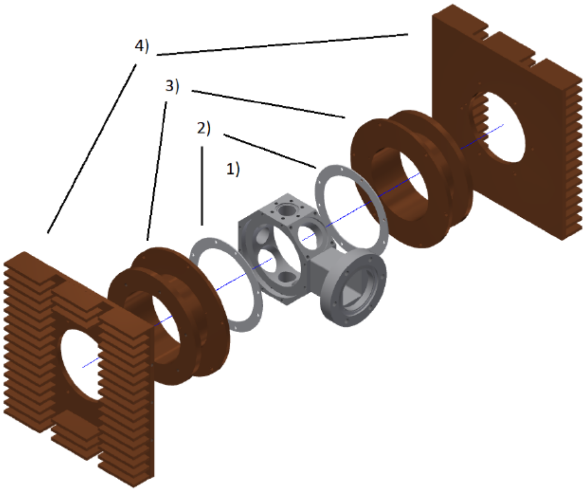

Figure 35: 1) Titanium science chamber, 2) thermal isolator, 3) copper support for coil, 4) heat sink[85]

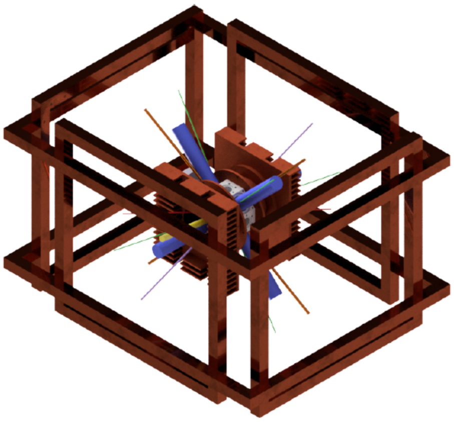

Figure 36: The compensation coils surrounding the Science chamber.[85]

4.3 Laser Systems

4.3.1 Distributed Feedback (DFB) Laser

Most lasers (such as Fabry-Perot) are not efficient in the sense that there are multiple close wavelengths outputted either side of the desired setting, albeit with lower power. The type of laser being used in this experiment is a distributed feedback laser which does not suffer this problem - it emits only a single wavelength. The addition of a grating above the active layer of the laser is what sets it apart from others. It has a zig-zag composition with spacings and refractive index designed to only allow one wavelength of light to be reflected back whilst others pass through unperturbed, thereby feeding back the desired wavelength throughout the whole laser into the cavity. This where the "distribution" of the feedback comes from and so only this light wavelength builds up and eventually released from the cavity. The addition of the grating is more expensive though but the value comes from being able to use more signals in the space of fewer wavelengths which is key in modern optical networks.

DFB lasers have a resonator that is entirely made of a periodic structure that behaves as a distributed reflector in the wavelength range of laser action, containing a gain medium which amplifies the power of light. The periodic structure is usually made with a phase shift in the middle of it. The structure is made of two interconnected Bragg gratings with an optical gain within the gratings. The DFB laser also has multiple axial resonator modes, with one mode usually favoured in terms of losses. Single frequency operation is often easily achieved, in spite of spatial hole burning as a result of standing wave pattern inside the gain medium. Due to large free spectral range, wavelength tuning without mode hops can be done over a range of nanometers.

In a fibre laser the distributed reflection is within a fibre Bragg grating, usually only a few mm or cm. It is a very simple and compact single-frequency laser fibre which leads to low intensity and phase noise levels. Our laser, semiconductor DFB, has the corrugated waveguide built above the active region, requiring time-consuming regrowth techniques. The typical power outputs are tens of milliwatts whilst the linewidth is a few hundred MHz, with wavelength tuning often possible over several nm.

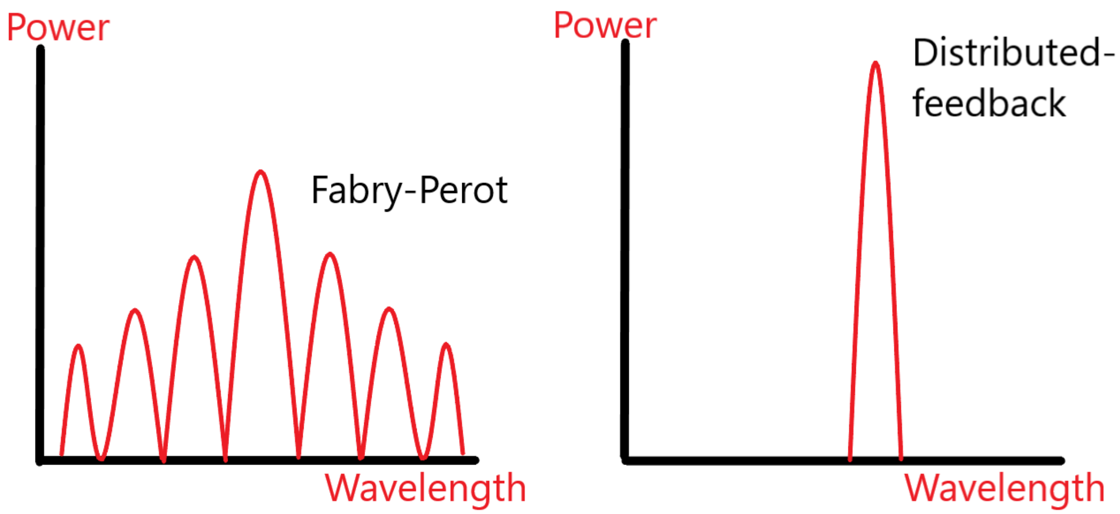

Figure 37: Fabry-Perot lasers have their power split between multiple wavelengths either side of the desired one whereas the distributed feedback laser will have its power only go to one specific wavelength.

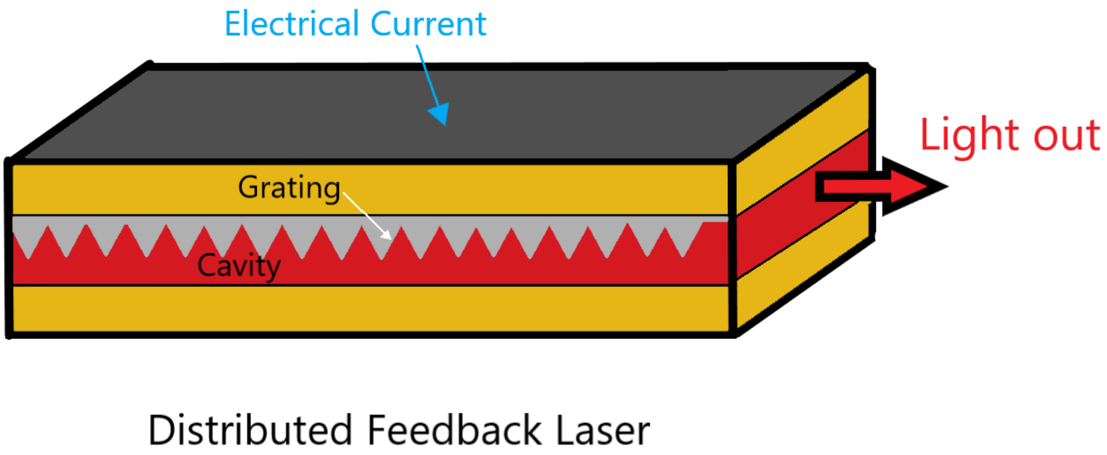

Figure 38: The corrugated layer above the active layer of the laser with a specific refractive index and space of the gratings are designed to reflect only one wavelength of light. This wavelength of light then continues to reflect and build up in intensity within the whole of the cavity layer. This ”feedback” of the light back into the cavity is ”distributed” across the whole laser which the laser is named after.

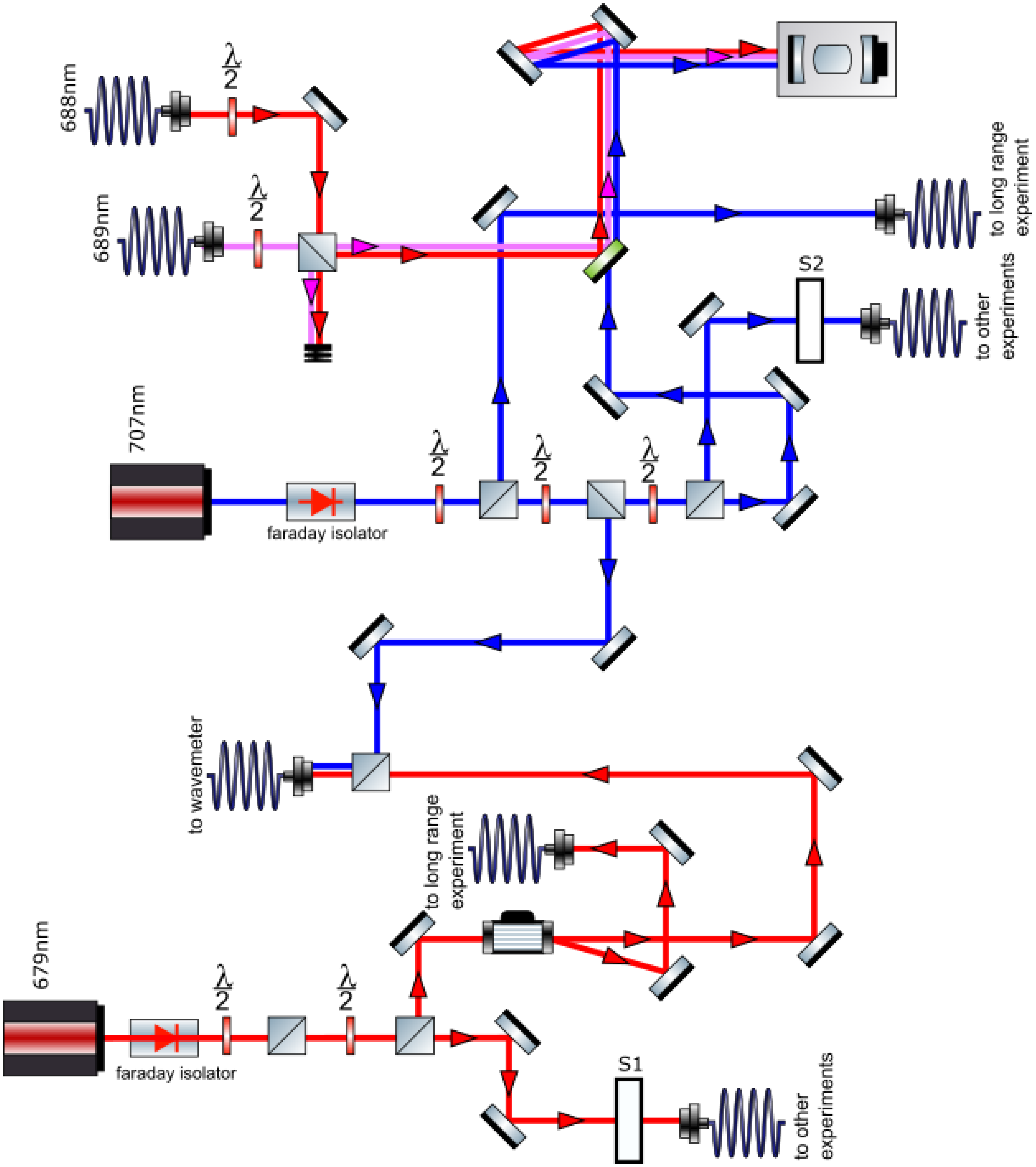

Figure 39: The repump lasers adapted from Marco's setup[85]. The 707, 689 and 688 nm lasers are not actually locked into a cavity but they can be. As of now they are locked to a wavemeter. S1 and S2 are shutters controlling the 679 nm and 707 nm beam of the other experiments, respectively.

4.3.2 Pre-Cooling/Blue MOT/Detection - 461nm laser

The 461 nm laser is responsible for not only providing the blue MOT but also the Zeeman cooling beam and detection for the camera. The main (M squared lasers) Ti:Sapphire laser at 922 nm is followed by a cavity doubler that doubles the frequency to 461 nm and with 550 mW of power. The power is split into four branches using several polarising beam splitters (PBS) and half waveplates ($\lambda/2$). The first branch goes to the Zeeman slower, the second forms the MOT beams, the third goes to the wavemeter for monitoring and the fourth is sent to other experiments in the cold atoms group. The frequency is locked at +19 MHz from the transition by a PID loop controlled by the wavemeter. The wavemeter (WSU2 from highfinesse) has a resolution of 500 kHz and is calibrated using a SLR-780 rubidium reference laser.

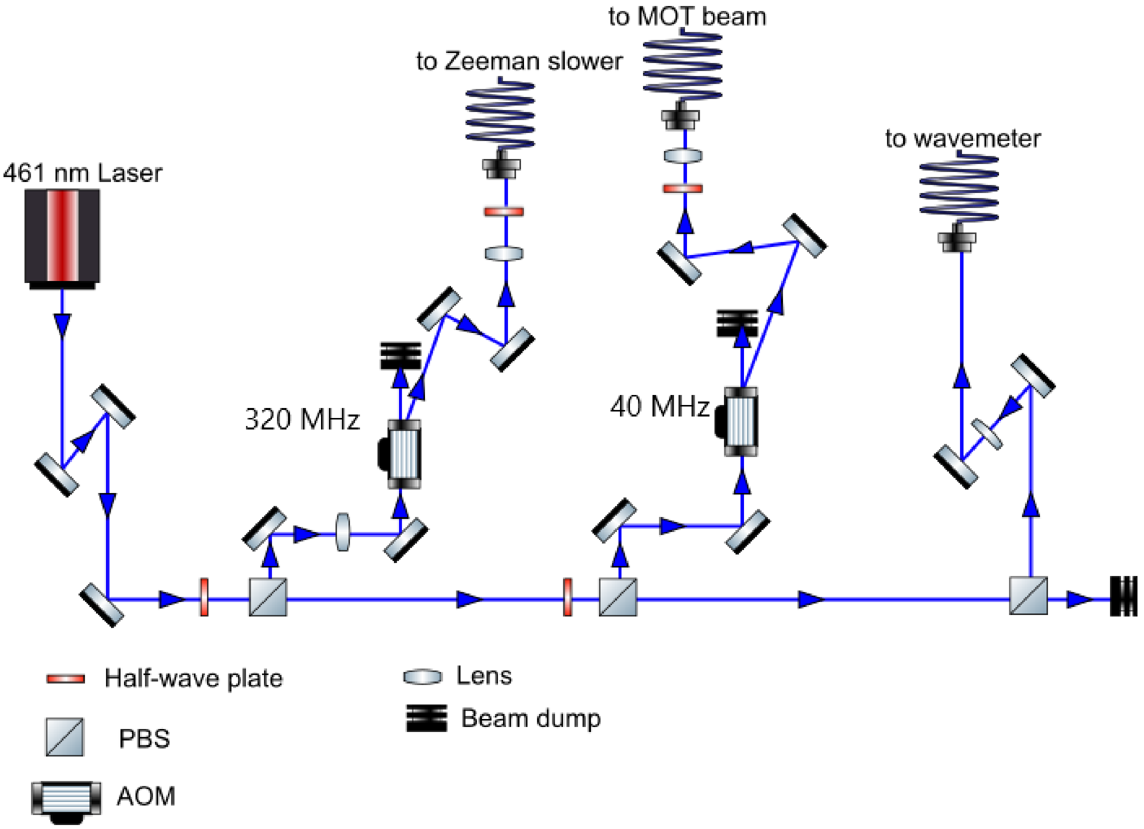

Figure 40: The 461 nm laser is divided into 3 branches that go to the Zeeman slower, MOT science chamber and finally the wavemeter. The beam that is sent to the MOT is subdivided into 2 beams, one for the main use of MOT and the other is the probe beam headed towards the camera.

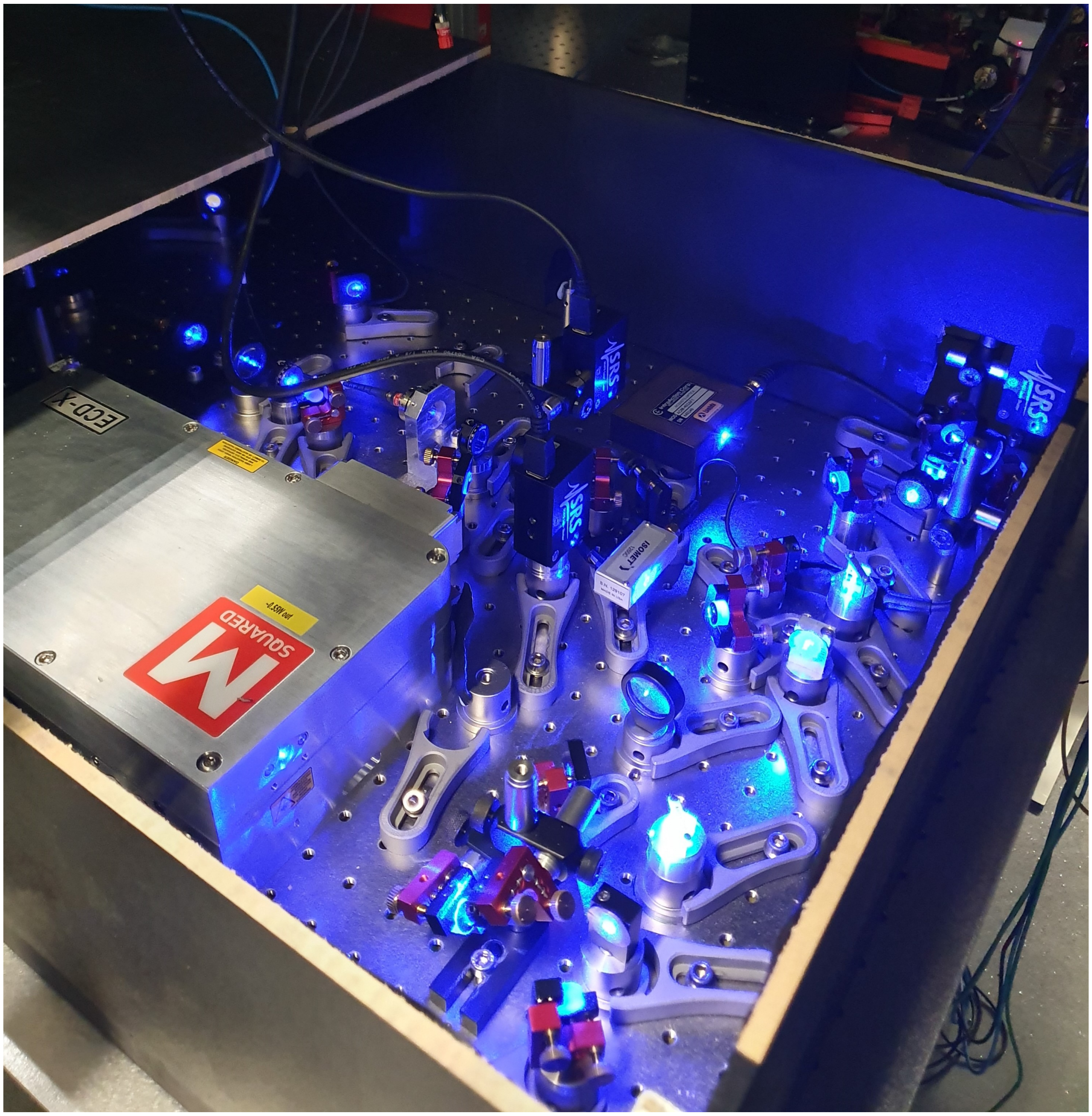

Figure 41: The ECD-X 461 nm laser enclosure setup on the optical bench. The optics can be shielded from above with a wooden lid.

Along the Zeeman branch (see Fig 40), the light enters into an acousto optical modulator (AOM) which is set to -320 MHz generated from a direct digital synthesizer (EVAL-AD9959). Just after the AOM a laser shutter is placed. The laser polarisation is aligned with the Polarization Maintaining (PM) fibre's fast axis by utilising a $\lambda/2$ plate just before the coupler. At the other end of the fibre, the emitted light is 45 mW and passes through a $\lambda/4$ plate, expanded to 20 mm and then focused to 75 cm in order to maximise the intensity at the Zeeman slower and have a minimum at the MOT. The whole array of optical components can be seen in Fig 41.

The cooling laser is controlled by a 40 MHz AOM. Just like the Zeeman branch, the polarisation of the beam is for the fast axis of the fibre with a $\lambda/2$ plate and lens. Exiting this fibre (see Fig 42) another PBS is placed to increase the polarisation purity of the 461 nm light which then overlaps to the 689 nm laser path through the use of a long pass dichroic mirror (DMLP567). These beams then split into three with more PBS and $\lambda/2$ plates to be circularly polarised with achromatic $\lambda/4$ plates. The three beams enter the science chamber at right angles to one another and upon exiting they are then reflected by an arrangement of mirrors and $\lambda/4$ plates, reversing direction and polarization simultaneously. The overall effect is to provide 6 beams into the MOT.

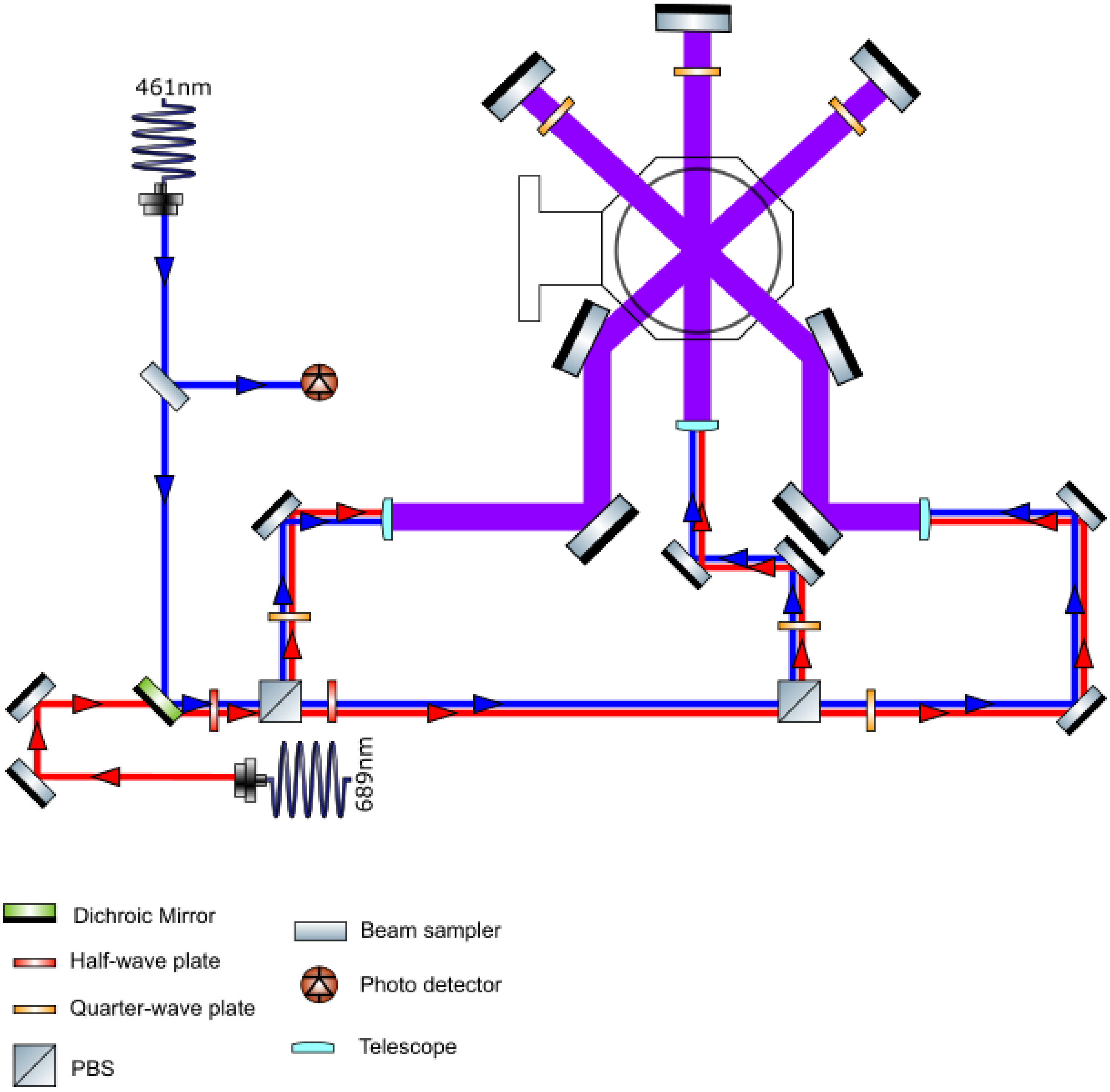

Figure 42: Delivery system to the Science Chamber of the MOT beams. The 3 widened beams going into the chamber are retro reflected from the other side to give in effect 6 beams in 3 dimensions, creating the MOT.

4.3.3 Second Cooling - 689nm laser

The 689 nm laser is a commercial ECDL laser connected with a Tapered Amplifier (TA). Before the TA the power is only 10 mW. The total power of the main laser is 250 mW. The optics are on their own separate breadboard which has shock absorbing feet. The main beam is split using a PBS with one branch going to the wavemeter whilst the other passes through a roughly 80 MHz AOM which is needed to set the beam to the correct frequency and applies 1.6 MHz modulation during the broadband cooling phase. After this it goes into a polarization maintaining (PM) fibre that sends the light to the science chamber. Further details concerning the 689 nm laser can be found in Marco's setup.

4.3.4 Repump - 707nm laser

The home built repump laser is used for moving atoms from $^3P_2$ to $^3S_1$ state. The 707 nm laser is sent to several areas: the science chamber through optical fibre, the wavemeter, a cavity and for other groups' usage. The final power in the science chamber is 2.5 mW with a beam waist 3 mm.

4.3.5 2.6 µm clock laser

This 2.603 µm laser with power 7 mW is also home built. It consists of a PIN diode that provides the initial laser and then a Bragg grating for refinement (see Fig 43).

The beam encounters an AOM at 40 MHz which controls the efficiency of the output beam. Changing the voltage will change the power of the 2.6 µm light. Due to being in the infra-red range of light, it is not visible which causes problems in alignment. To align the beam requires the use of a liquid crystal detector card which will change colour when exposed to different temperatures, revealing the location of the beam with a darkened spot. In this setup (shown in Fig 44) though, there is an additional 679 nm laser beam which has been overlapped with the 2.6 µm laser that can be toggled on and off with use of the flip mirror. A nice coincidence is that this additional laser is resonant to $^3P_0$ - $^3S_1$ transition so the effect will be seen in the MOT. Correct alignment results in more atoms present in the MOT. The laser is subdivided into three paths with the aid of a beam sampler. One path leads to a wavemeter, the second goes to a photodiode for checking power and the third is the main beam power towards the science chamber.

2.6 µm stabilization cavity

Here the Pound-Drever-Hall (PDH)[110] technique of frequency stabilisation used for locking the 2.6 µm cavity will be explained. As of this moment the laser is free running and prone to drastical changes in frequency at any moment during use. Commercial lasers have their own way of restoring the frequency back to normal, perhaps using an input signal that will correct the output laser frequency, but this is simply too slow. A separate cavity is incorporated

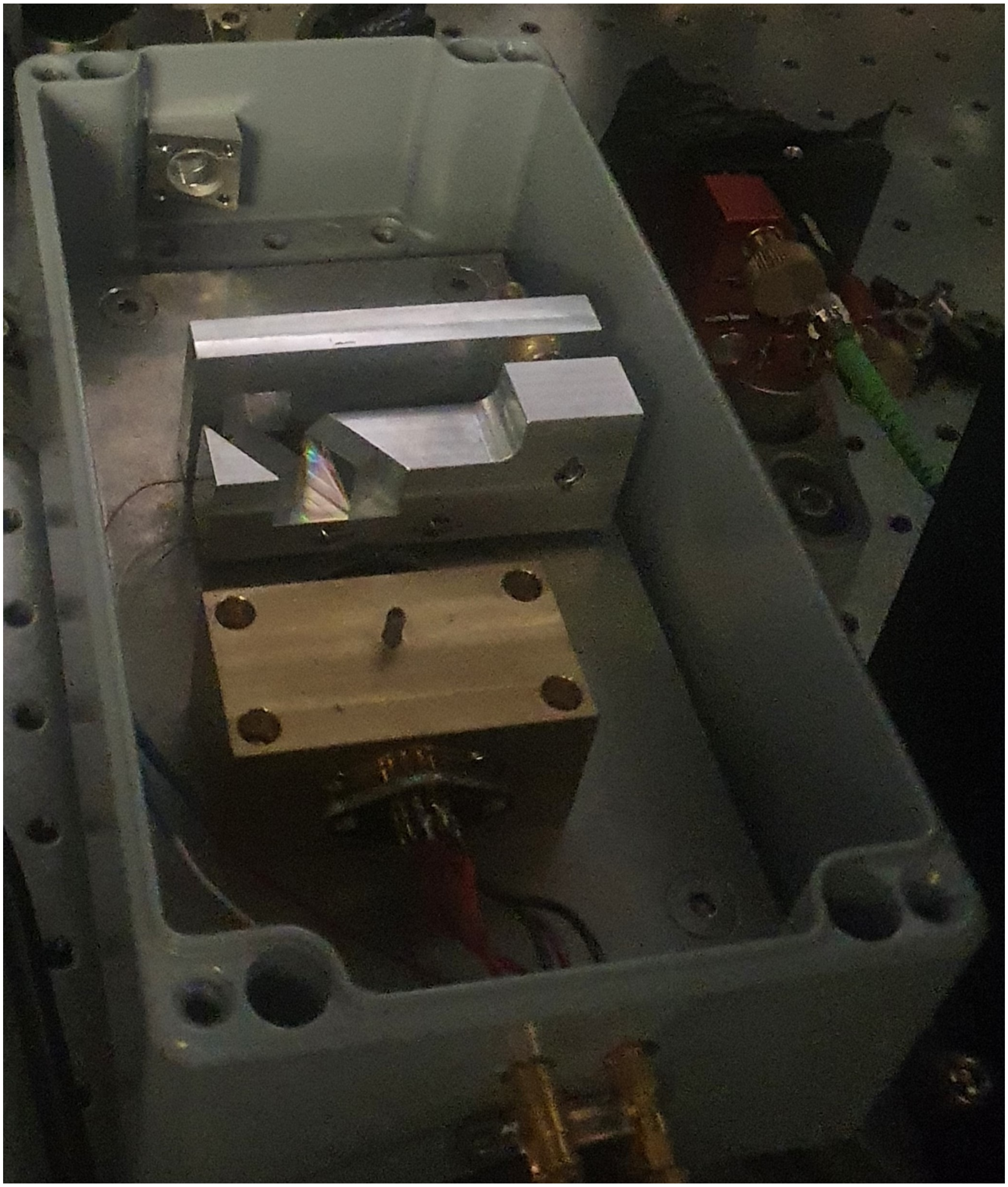

Figure 43: The inside of the 2.6 µm laser.

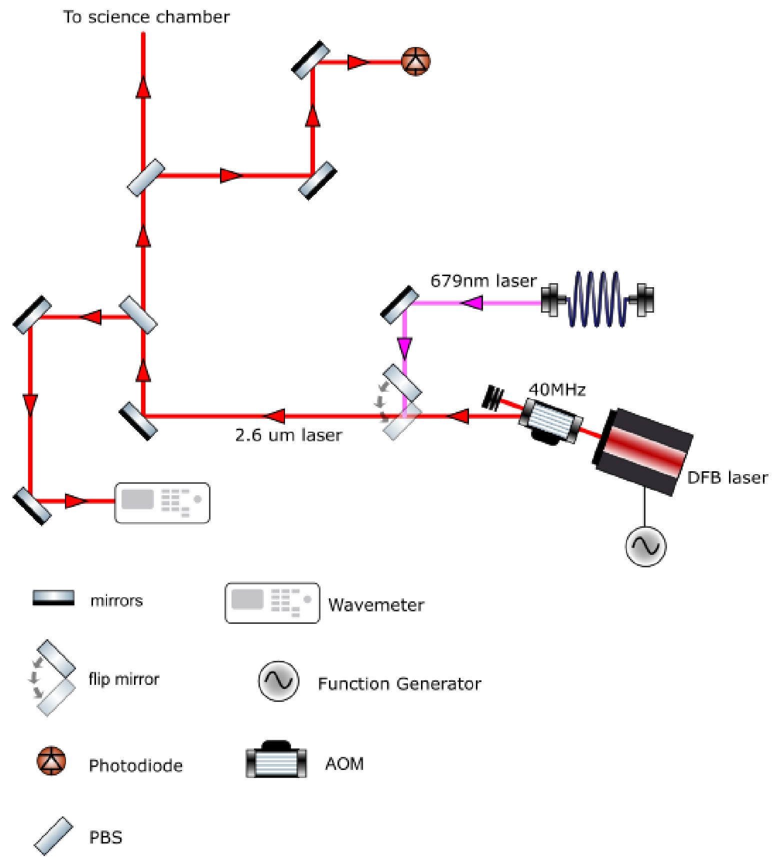

Figure 44: A recreation of the 2.6 µm setup from Marco's thesis[85]. The laser is sent through an AOM at 40 MHz and the -1 order branch is used to send to both the wavemeter for monitoring, a photodiode and the science chamber. A flip mirror allows the 679 nm laser to be overlapped with the invisible 2.6 µm in order to align with the mirrors and it too will increase the number of atoms in the MOT.

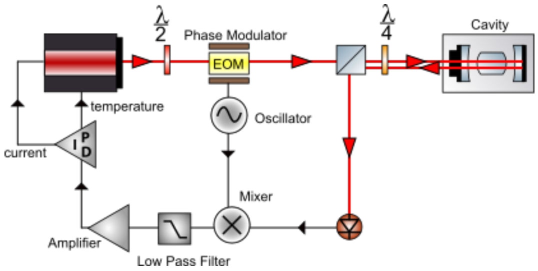

Figure 45: The 2.6 µm setup on the lab bench. Two waveplates, a $\lambda/2$ and $\lambda/4$ are needed to focus the beam into the chamber. The PID circuit used to lock the laser has two feedback signals for temperature and current. Temperature is used for slow locking and the current is used for fast locking.

into the lab bench which will aid the speed of frequency restoration.

The length of the cavity will be resonant to the 2.6 µm laser frequency. Some methods may try to keep the reflected light intensity constant in order to maintain constant frequency[111]. The optimal frequency gives the largest intensity of reflected light but a reduction in light can come from going above or below resonance which is why the derivative of the the reflected light is used instead thanks to its anti symmetry about resonance.

Fig 45 shows a possible setup. The laser light will enter into an Electro-Optical Modulator (EOM) to vary the phase as opposed to frequency which can be easier to do. The light will enter the cavity and after bouncing around it eventually exits the same way it entered to give the reflected beam. The reflected beam is then guided into a photodetector which in turn provides a signal. This signal along with the EOM oscillator signal is entered into a mixer to be compared. The mixer will subtract the two signals and then this resultant error signal is sent to a low pass filter to remove unwanted noise. The error signal is then passed through a servo amplifier to be inputted into a PID circuit. Depending on whether the error signal shows a shift above or below resonance, the PID will send a signal to the input port on the laser to correct the frequency back onto resonance.

The PID will only send a signal when the difference between oscillator and photodiode signals is outside a certain acceptable range i.e. when the laser is no longer locked. The proportional parameter P determines how large the outputted signal is to the laser which will be proportional to the error signal. The integral paramter I determines the time for adjustment which ideally should be a few seconds for correcting. Finally the derivative parameter D looks at how the error signal changes over time to make longer term adjustments.

4.3.6 813nm laser/412nm laser

This 813.4 nm laser can ouput a maximum of 3 W, with 1 mW being used for the wavemeter, whilst the remaining laser power goes to a high power PM fibre (see Fig 46). The final 1 W of power exiting is then passes a 20 mm lens after which the beam is sent to a 200 mm lens, leading to beam waist of 50 µm. When the beam reaches the other side of the chamber, a 75mm lens collimates the light to hit a hot mirror (FM01) to be reflected back tightly. The lens also collects the fluorescence of the atomic cloud used in spectroscopy.

The 813 nm laser is frequency doubled to become a 412 nm laser used for the optical lattice. The optical lattice is blue-detuned from the 698 nm laser used on the $^1S_0 \rightarrow ^3P_0$ transition. By trapping the atoms in the lattice, the 698 nm laser will not be able to light-shift the energy levels relative to one another and so the 698 nm laser can continue to be on resonance.

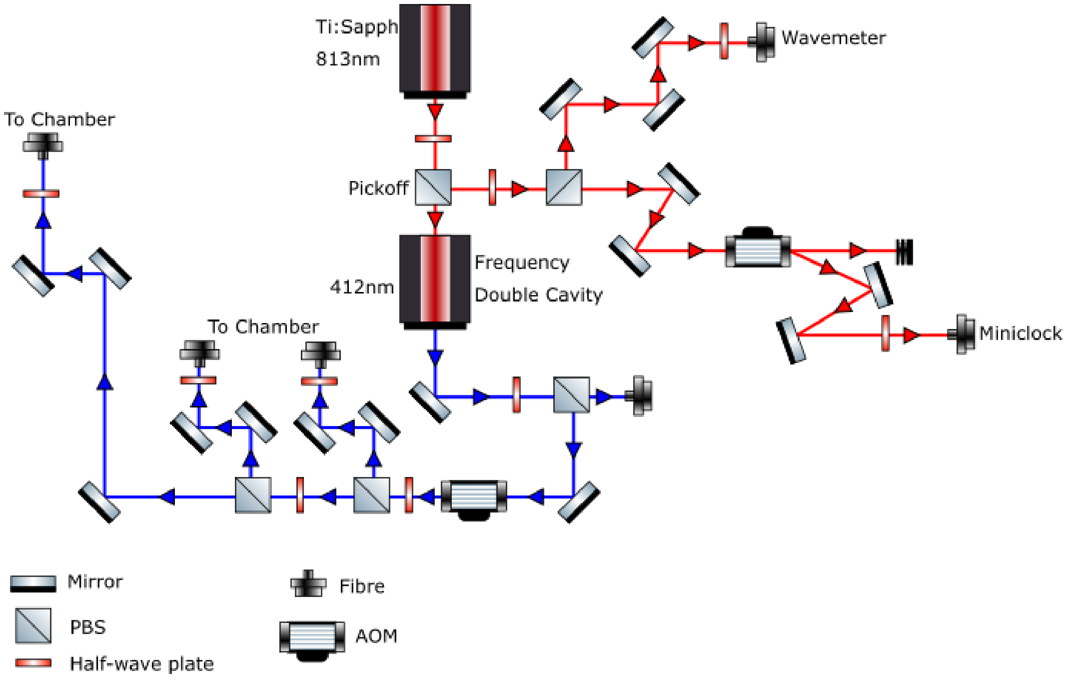

Figure 46: 813 nm nm laser is split to be sent off to the miniclock system and wavemeter. The remaining branch is frequency doubled to become 412 nm for use in the optical lattice. The AOM for the 412 nm branch will be from ISOMET (M1002-T110L-2).

Fig 20 shows how the presence of a laser can shift the energy levels of an atomic transition but when the atom is trapped inside an optical lattice, the relative shift in energy levels of ground and excited state is zero. Using the laser wavelength as a reference λ_1, optical lattice laser λ_2 we have a red-detuned optical lattice when $\lambda_1 < \lambda_2$ (blue-detuned for $\lambda_1 > \lambda_2$).

4.3.7 Dipole laser - 1.06 µm laser

There are many methods that experimentalists may use to gain a sample of ultracold dense atoms but the optical dipole trap has an advantage over them as it does not require the use of a magnetic field and a low number of optical excitations that can yield a tightly confining trapping potential[117]. These properties make it possible to use to obtain a BEC.

Other groups trying to create BECs in dipole traps have used CO_2-lasers[118] in single beam or cross-beam configurations[119] [120] [121]. There can be disadvantages to using longer wavelengths such as 10.6 µm at the necessary high powers as there would need to be optical components that can handle this light which are very hard to get. A wavelength closer to 1 µm is commercially available and does not suffer the aforementioned drawbacks. Prior systems using this wavelength have had some unexpected losses in atom number especially when using cost-efficient high-power multifrequency laser like fibre lasers. Experiments trapping ^{87}Rb in a BEC are few due to complicated setups employed[122], such as shiftable lenses allowing a compression of the trap which compensates the lower power available.

This setup starts off with the atoms in the MOT and then loaded into a crossed dipole trap with the 1064 nm lasers from Azurlight systems (see Fig 47) perpendicular to one another. Only the dipole laser intensity is increased during the evaporation process. In Fig 48 the beam is split into two beams with polarising beam splitters and an AOM at 80 MHz regulates the power for each beam. After the laser exits the fibre, a lens will be placed in front of both beams to focus them into the MOT. The beam waist can be easily varied here by changing the lenses. As the MOT loading phase occurs, the dipole lasers are turned on to maximum power (20W).

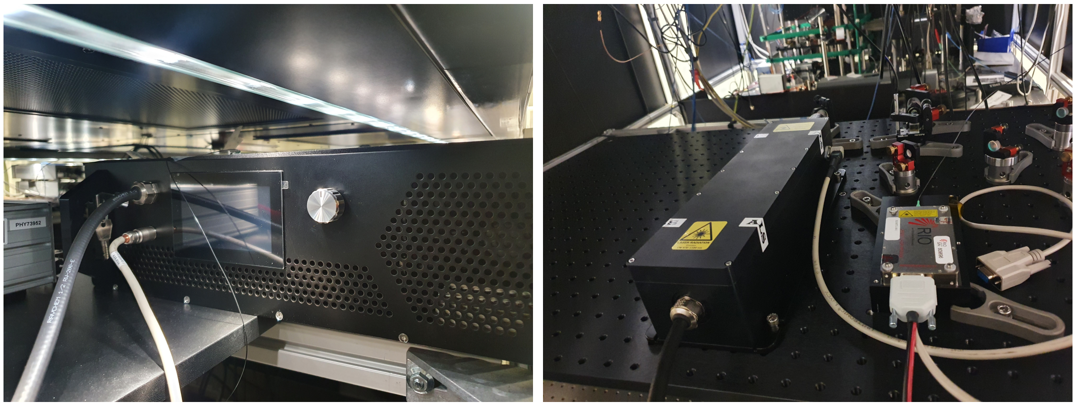

Figure 47: Azurlight systems 1064 ± 0.5 nm laser. It can operate at a maximum of 50 W, single frequency linewidth <50 kHz with ultra-low noise <0.02% RMS. It has beam diameter 10±0.2 mm, short term power stability < ±0.3% and long term power stability (8 hours)< ±0.5%. (Left) Laser controller with multi-turn potentiometer. (Right) The laser head 330×115×80 mm.

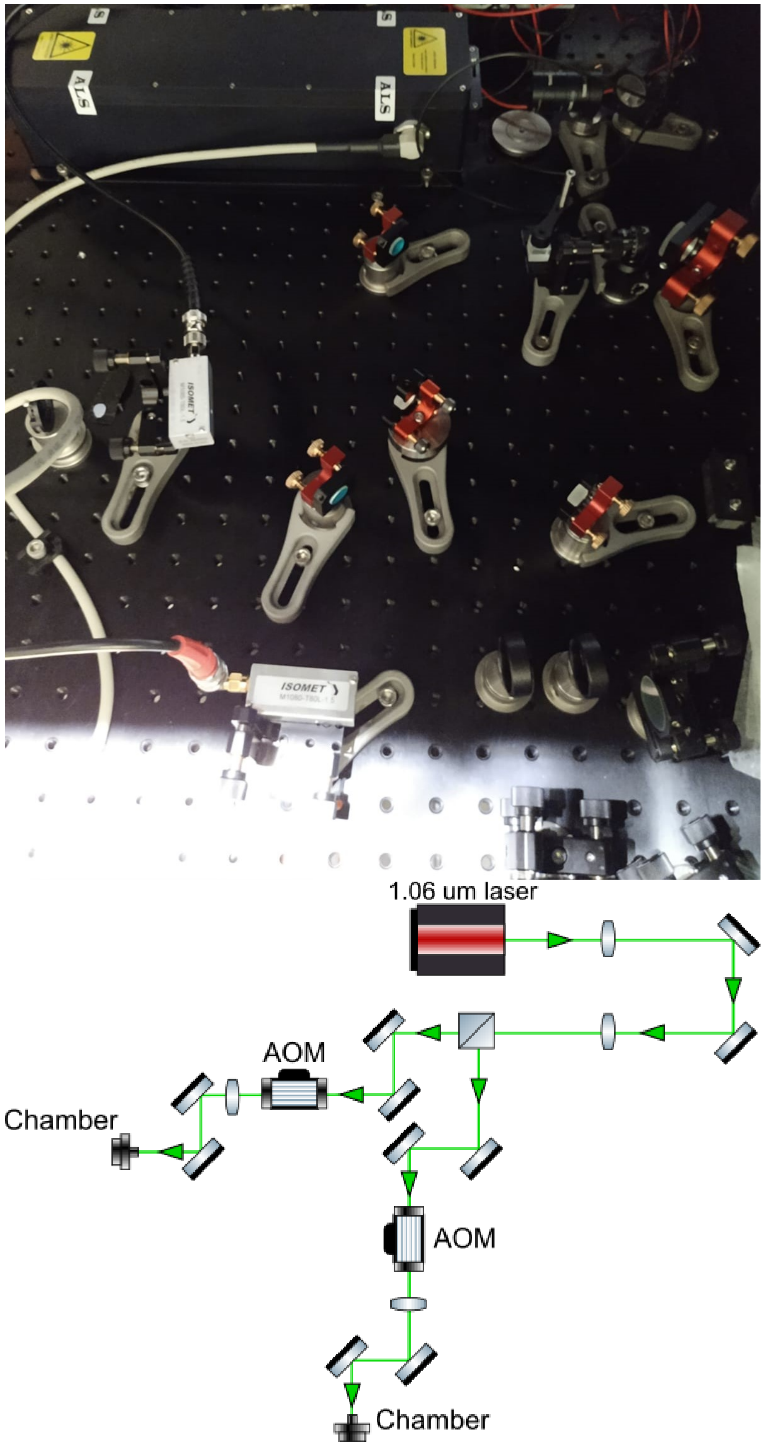

Figure 48: (Top): The current 1.06 µm laser setup on the bench and (Bottom): drawing of the final setup of the 1.06 µm dipole laser.

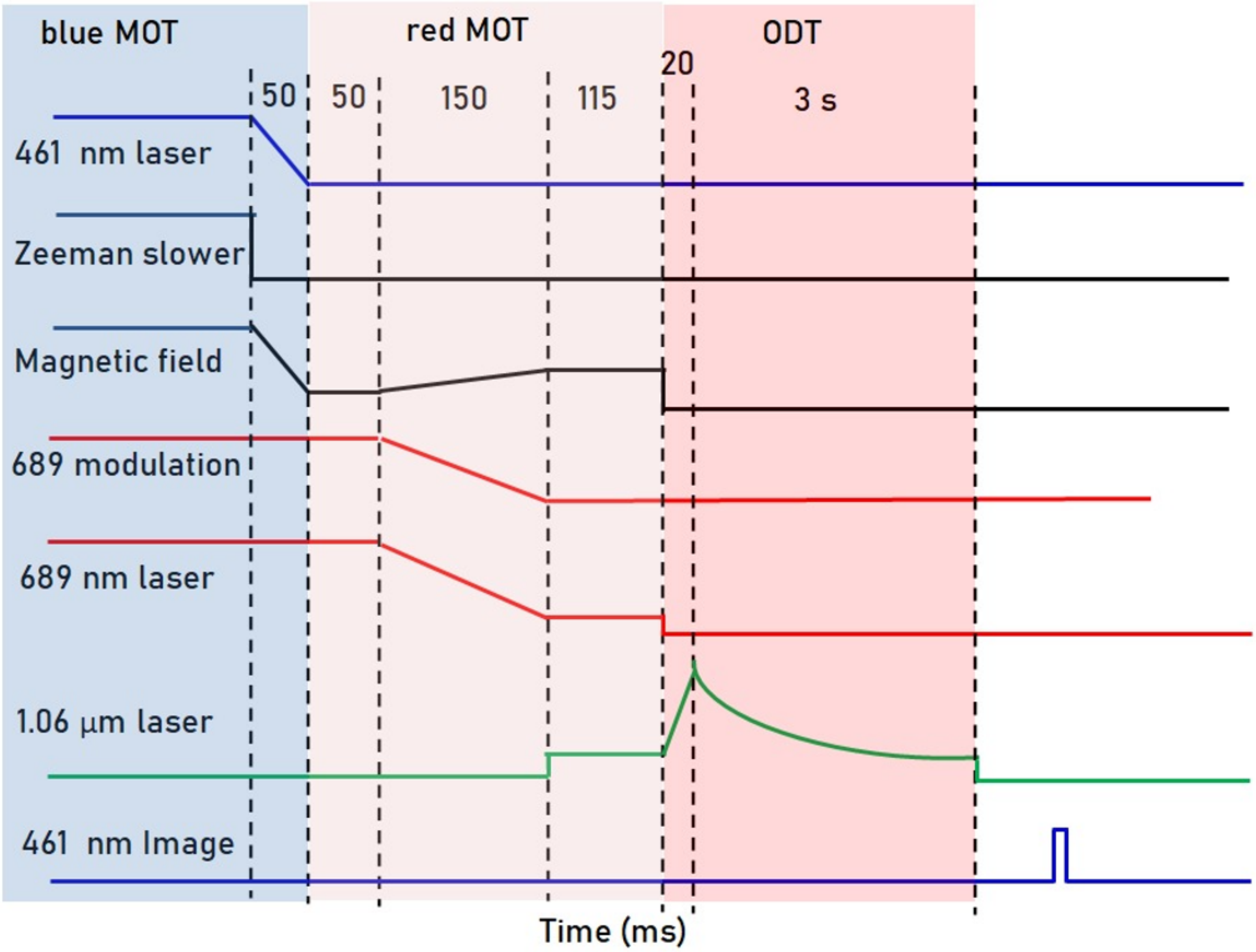

Figure 49: The timing sequence for the blue MOT →red MOT →optical dipole trap is shown.

Fig 49 shows the order in which this experiment can be performed. Starting from blue MOT over the first 50 ms the 461 nm laser is gradually turned off along with the magnetic field (the Zeeman slower is immediately turned off). Over the next 50 ms the broadband red MOT occurs before single-frequency red MOT sequence starts. Over the next 150 ms the magnetic field is very gradually increased and the 689 nm laser is reduced. The 1.06 μm laser is turned on now at low power over the next 115 ms to prepare for the optical dipole trap. For the first 20 ms of the ODT the dipole laser is ramped to high power and the 689 nm laser is turned off along with the magnetic field. Over the next 3 seconds the dipole laser power is gradually decreased to perform evaporative cooling before being turned off. Afterwards the 461 nm laser for the camera is turned to capture an image of the resultant atomic cloud.

Dipole laser characterization

The dipole laser can be extremely dangerous and major safety precautions were undertaken when operating at full power, including constructing a wall surrounding the optics. The data sheet that was packaged included some values for the display power and actual power for selected input currents in Table 2. The actual values for the 1.06 µm dipole laser on the lab bench is shown in Table 3. It is apparent enough that the output power for the bench cannot be tested further than 7 A as the power exceeds 20 W and would not be safe to collect further data to compare at this present time without further precautions.

Table 2: Front panel display calibration: List of input currents, display values for power and actual output power according to Azurlight systems. The pre-amplifier for their test had been set to 0.3 W.

Current (A)	Display Set-Point (W)	Power Out of the laser head (W)
0.72	0.26	0.15
1.0	0.6	0.50
2.0	3.4	3.35
3.0	6.6	6.60
4.0	9.85	9.90
5.0	13.1	13.10
6.0	16.2	16.20
7.0	18.6	18.60
7.25	20	20.00
7.36	20.6	20.60

Table 3: Actual input current, display power and output power for the dipole laser on the bench. The pre-amplifier was at 0.34 W.

Current (A)	Display Set-Point (W)	Power Out of the laser head (W)
0.73	0.3	0.35
1.0	0.59	0.64
2.0	3.38	3.57
3.0	6.29	6.70
4.0	9.85	10.3
5.0	13.15	14.30
6.0	16.5	18
7.0	19.4	21.6

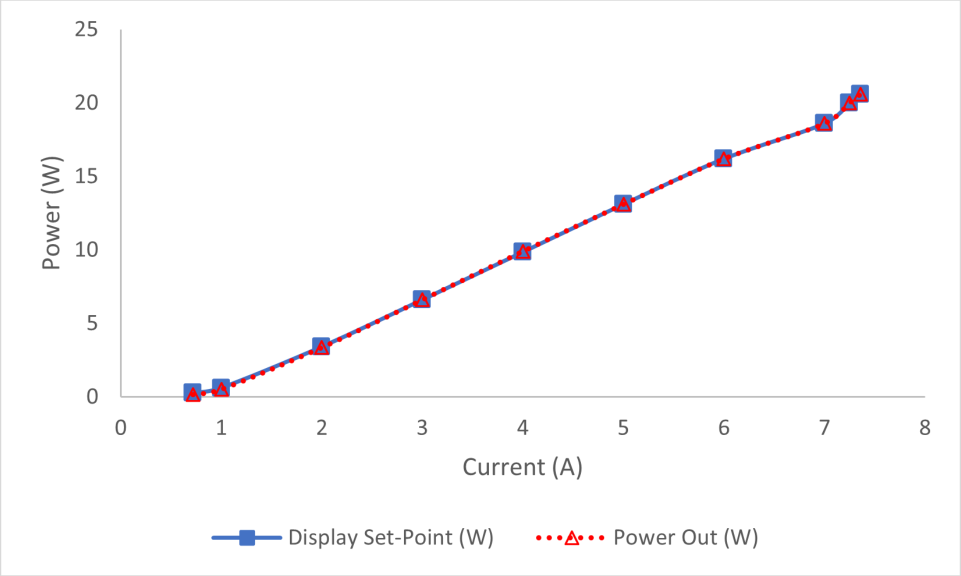

Figure 50: The values from Table 2 show a very strong overlap for the commercial laser display power and output power.

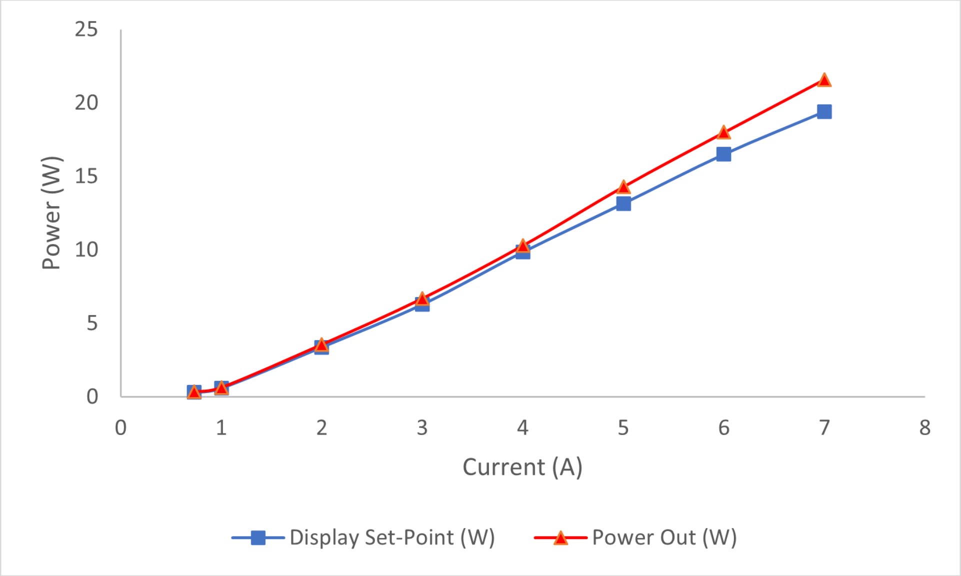

Figure 51: The values from Table 3 show the deviation between display power and output power for the setup in the lab.

4.4 Imaging

Flourescence imaging is the clustering of photons scattered from the atoms in the trap. Two images of the MOT are required: one for loading under normal conditions and the other is an image for the MOT loaded with the atoms. The difference between the two images leads to a quantitave value of the number of atoms in the trap. The software bundled with the camera allows taking a background measurement of fluorescence which is automatically used to generate a proper readout for the MOT.

The experiment makes use of the 461 nm lasers to fluoresce the atoms in conjunction with a 1-inch diameter lens with 75 mm focus, situated under the science chamber. 50 cm away the light is directed to the sensor of a Zyla 5.5 (Andor) camera (see Fig 52) with a 50 mm, f=1 lens. In between the lenses is a model FM01 Thorlabs heated mirror as well as a 70:30 beam splitter. This mirror is used to make the lattice and also filter unnecessary light from getting to the camera. Part of the light is branched using the splitter into a PMT tube, which has a better sensitivity than the camera, faster response time and also easier to operate. The PMT's disadvantage compared to the camera is that it does not provide information on the atoms' distribution.

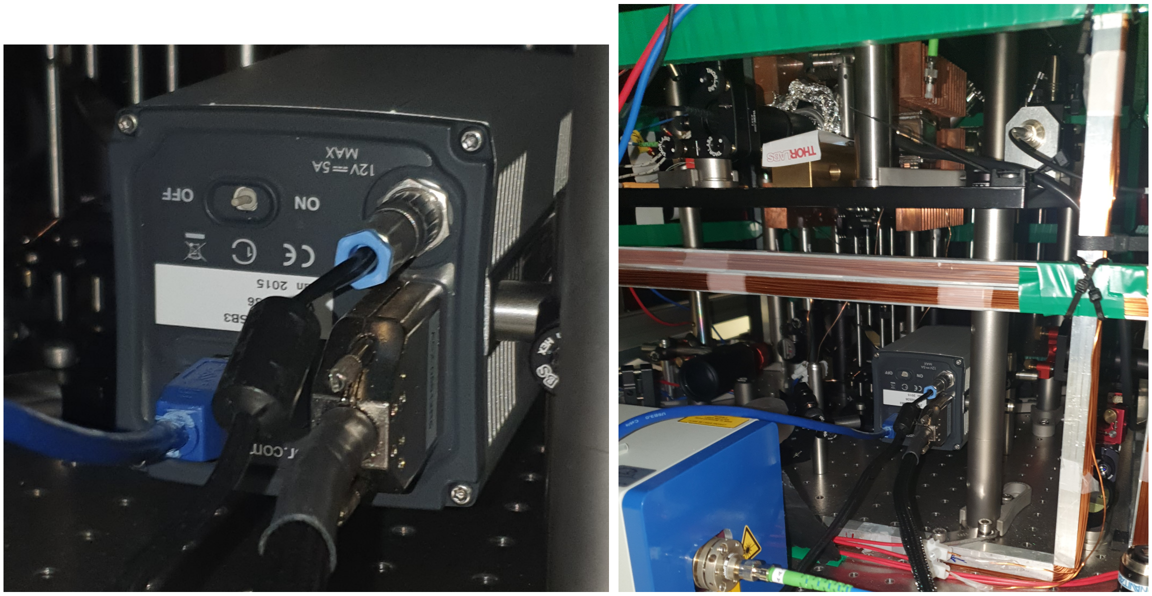

Figure 52: (Left) The Zyla 5.5 (Andor) camera used for fluorescence imaging. (Right) The camera positioned underneath the science chamber.

4.5 2.6 µm Chamber

As mentioned earlier, the 2.6 µm laser will increase the number of atoms present in the MOT but this can be further increased the more stable the laser is. To realise this, a cavity needed to be implemented that would make use of the PDH method via a temperature controller, regulated through a peltier element. A prior PhD student, Shruthi Viswam[112], had made a very similar chamber and so the basis of this design will begin the same and deviate where necessary. The cavity itself was assembled by Dr. Jonathan Jones and Freya Owen[131] where further details will be explained when that thesis is completed.

To start with, the optical reference cavity was made of an ultra-low expansion glass (ULE) 30 mm length cylindrical spacer with a 1 inch diameter, attached to the 2.6 µm rated mirrors (custom made by Layertec 150850 Fused Silica) either side of it (see Fig 53). The mirrors have a high reflectance (HR$>$ 99.98%) coating on one side and anti-reflection (AR$<$ 0.2%) on the other whilst the spacer has vent holes due to it being operated under vacuum.

ULE materials are often used for building reference cavities because they have very low coefficient of thermal expansion (CTE). This means when the temperature changes there is little change to the length of the material. The material that a cavity is made from will determine how it is affected by not only thermal expansion but air pressure changes as well.[113]

Even the smallest changes in cavity length will change the resonant frequency of the light trapped inside, dictated by the equations (see also section 3.3):

$$\frac{\Delta L}{L} = \alpha \Delta T \tag{76}$$

$$\frac{\Delta L}{L} = \frac{\Delta \nu}{\nu} \tag{77}$$

L is cavity length, ΔL is change in cavity length, α is the CTE of the material, ΔT is change in temperature, ν is resonance frequency and $\Delta \nu$ is change in the resonance frequency of the cavity.

The cavity length can be adjusted through the use of Thorlabs piezos (PA4JK 150 V, 3.5 µm Displacement, 3.0 x 3.0 x 3.0 mm) as an additional parameter, adjustable to account for any drift in the laser frequency. The epoxy glue was chosen instead of the optical contacting method because whilst the latter method made for a much more accurate cavity, it would not have the flexibility needed. One other point to consider was how stable it needed to be, with only 100 kHz to be accounted for, it seemed better to choose the epoxy method simply because of the difficulty in achieving a smooth flat surface for optical contacting. Optical contacting requires a high degree of flatness, only achieved through machining the surface to $\lambda/10$, although the payoff for doing this would be no additional material interposed inside the cavity, no changes to dimensions, less chance for outgassing at increasing temperatures and less stress on the cavity.

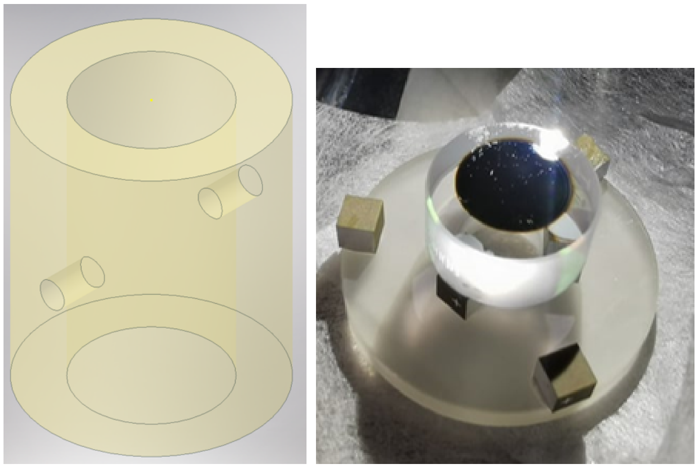

Figure 53: (Left) The ULE cylindrical spacer with vent holes. (Right) Mirror (Layertec 150850) and piezos (Thorlabs PA4JK) glued to disc.

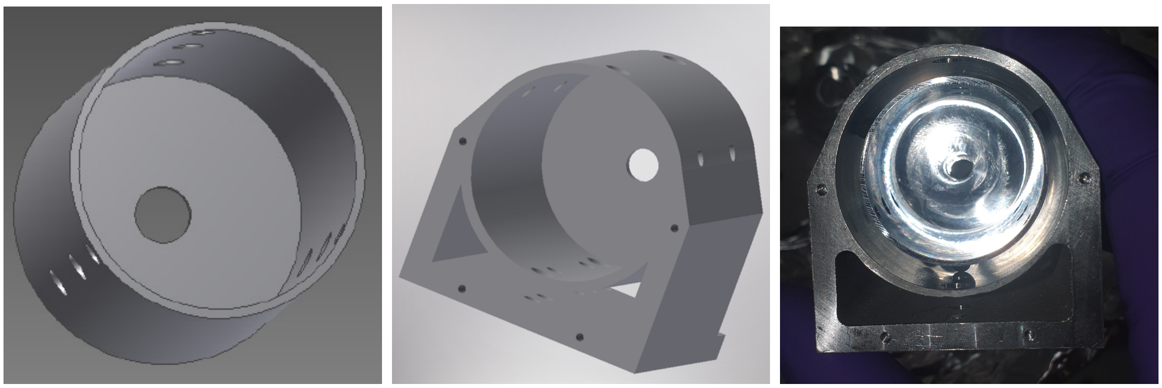

Figure 54: (Left) The inner can. (Middle) The outer can. (Right) The combination of the two as well as a viton ball inserted in between.

The cavity will be inserted into an aluminium inner housing (Fig 54), with the aid of 4mm viton balls. These viton balls provide rigidity to ensure the cavity remains in place, squeezed into 2 holes per column with a spacing of 120°(3 columns). This inner can is then inserted into an outer aluminium can using the same method, with 6 more viton balls pressed in between.

Underneath the outer housing is placed a peltier element (Thorlabs TEC3-6), designed to draw heat away from the interior and therefore stabilise the temperature of the cavity. The peltier element is regulated with a 10 kΩ resistor and connected to a temperature controller (Thorlabs T-Cube) which allows adjustment and monitoring (see Fig 55). Fig 58 shows the titanium chamber in both CAD and on the bench. The CAD drawing shows four holes at the edges which have actually been replaced with a single rectangular hole for clamping to poles on the bench. A transparent chamber is shown in Fig 56 where an optional copper base plate is placed beneath to aid the extraction of heat. Testing seemed to suggest that the base plate heats up too much to be used effectively with only one peltier element so this was axed from the final setup. Fig 57 is a simple diagram showing the plan for the final arrangement, with an additional peltier element placed outside the chamber but again this was scrapped due to time constraints.

Figure 55: (Left) T-Cube temperature controller. (Right) The TEC 3-6 peltier element.

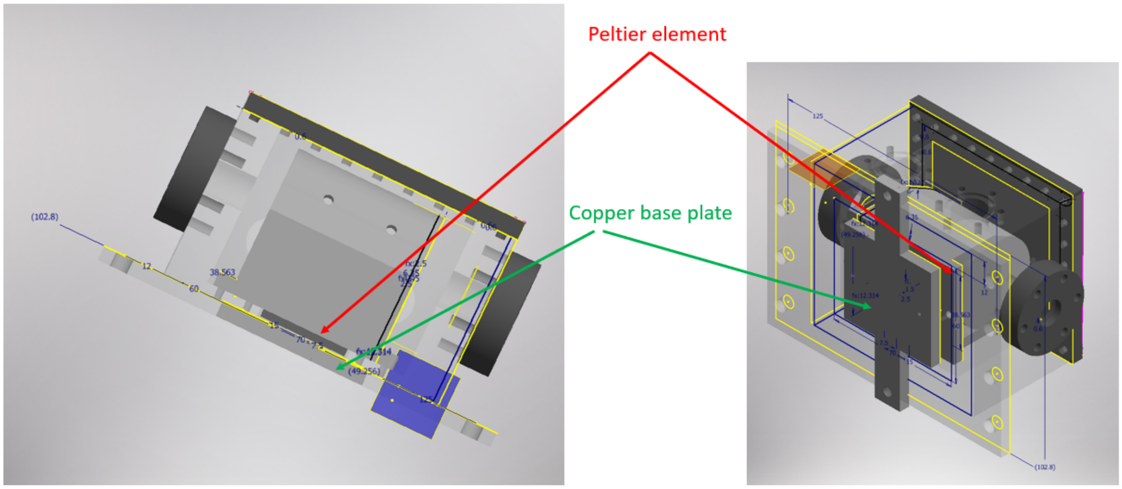

Figure 56: Titanium chamber hollowed out to show how the cavity housing, peltier element and copper base plate are to be fitted.

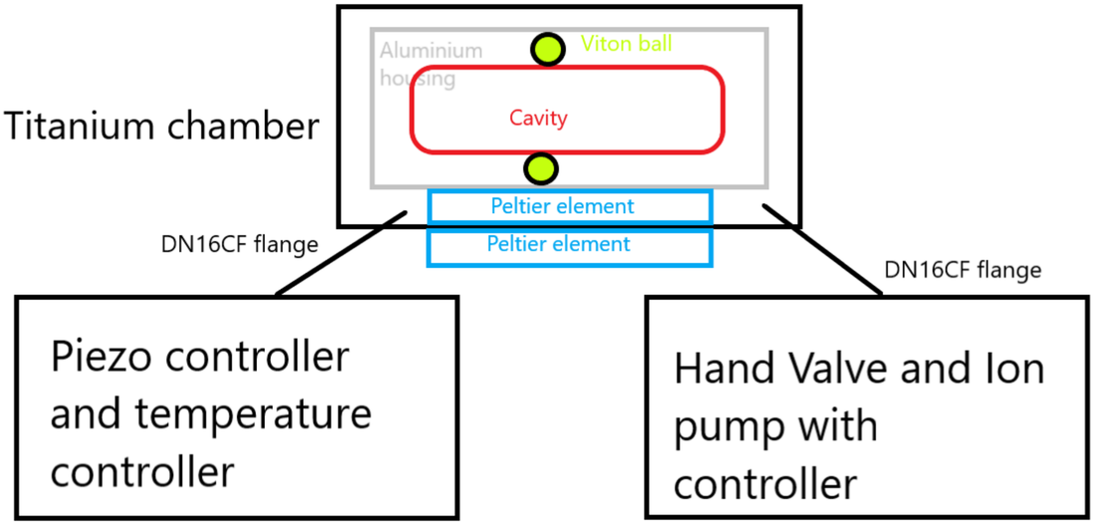

Figure 57: Basic sketch of the final assembly. Viton balls keep the outer housing bound to the inner housing. The temperature controller will feed into the PID loop for the PDH method.

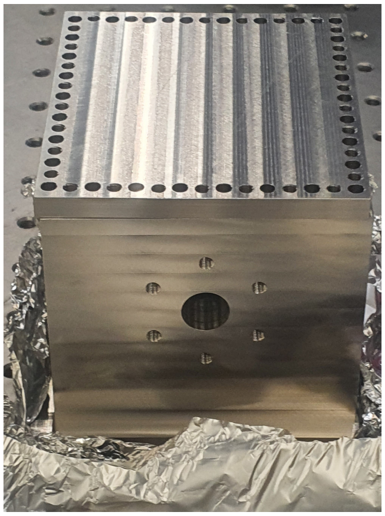

Figure 58: Front facing view of titanium chamber without windows attached.

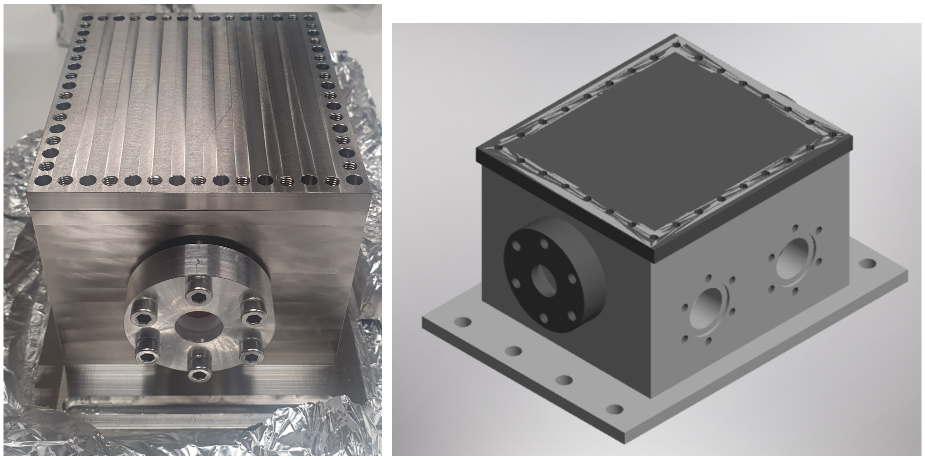

Figure 59: The window seal affixed to the chamber with teflon spacer and aluminium compression flange in both CAD and on the bench.

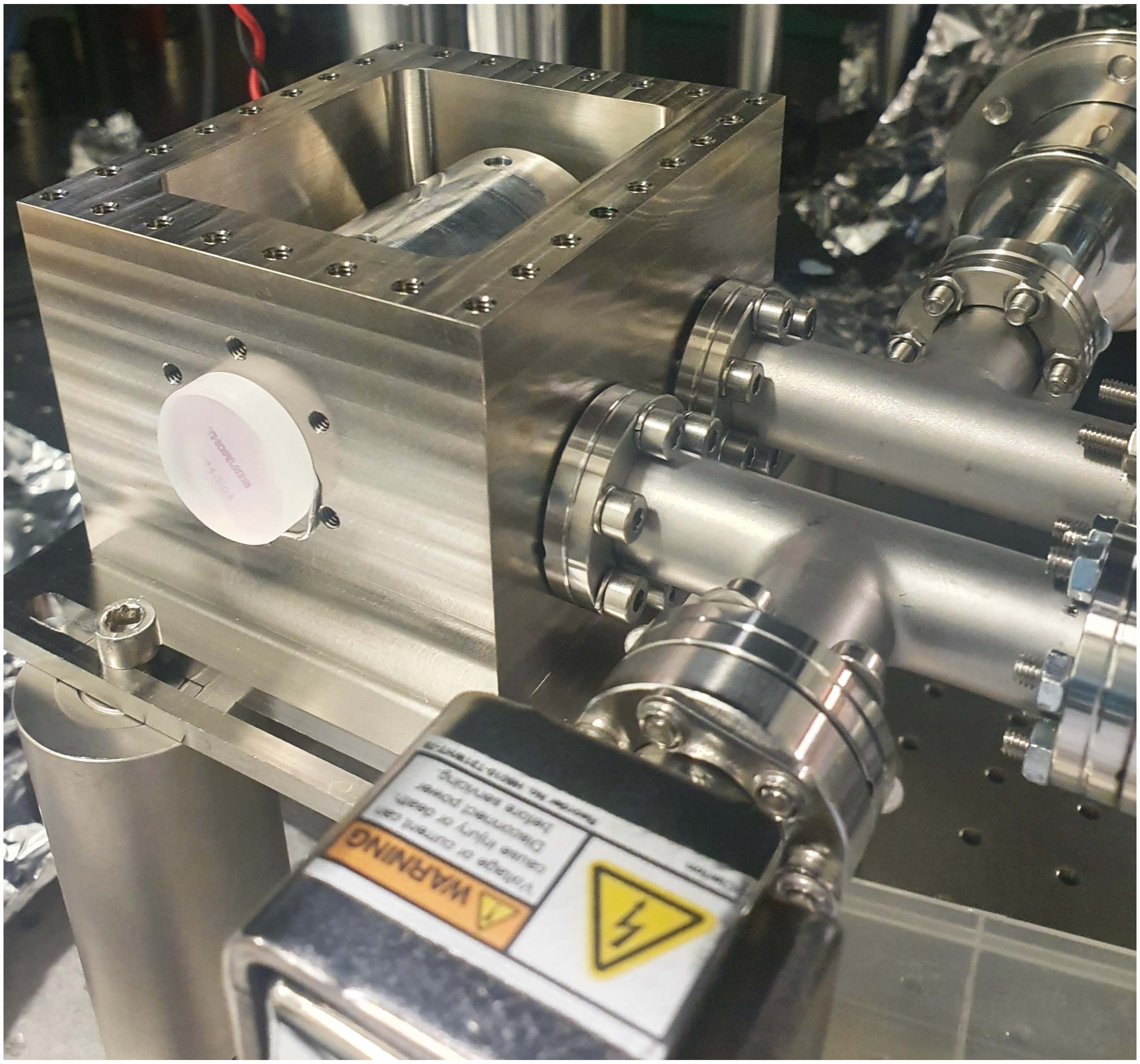

Figure 60: The chamber on the lab bench with the aluminium housing placed inside. The setup is raised about 10 cm above the lab bench by affixing M4 screws into the rectangular cutouts on the edge.

4.5.1 Vacuum Sealing

Once all the components are placed inside the chamber, it will be sealed up using indium which can hold a vacuum below pressures of 10^{-6} mbar[114]. This technique has been used in vacuum systems since 1957[115]. Indium is a soft metal, (with a melting point of 157°C and a CTE of 42×10^{-6}/°C) that can be flattened quite easily to create airtight seals for many materials such as quartz, ULE, germanium, pyrex, oxygen free copper. gold and titanium[116]. The seal will last for long time but can be removed with the use of acetone when needed. In one instance the windows needed to be removed and the use of a heat gun along with a flat edge could pry the indium sealing off the windows fused to the chamber. There was minimal damage to the windows, fortunately, but there is always a risk of shattering when using force.

All interior components need to be cleaned before the sealing process can begin as there will be no other opportunity to do so after the lid has been closed. The titanium chamber itself will be cleaned too as there must be no impurities or blemishes on the surface which can cause a failure in the vacuum seal when going to lower pressures. The workshop that made the chamber have machined it to be as flat and smooth as possible and then it must be cleaned thoroughly through the use of various methods which will now be explained.

The preliminary cleaning process begins with firstly, the chamber and aluminium housing being given a hand scrub with detergent followed by a rinse with tap water to get the large particles off and finally an ultrasonic bath in acetone for 15 minutes. This is necessary due to the way the parts were created after being machined by the workshop as there will naturally be residue from cutting. The final cleaning process consists of four ultrasonic baths, each lasting for 15 minutes starting with a soft metal detergent (as there are aluminium parts), distilled water, acetone and finally isopropanol. In between baths, each previous residue is rinsed away from the beakers that the components are placed in and then dried afterward. Once this cleaning is complete the parts are placed into an oven to bake away any moisture at temperatures exceeding >100°C over the course of a few days.

The indium wire (IN005130/62, Goodfellow Cambridge) must be cleaned as well with a light amount of force using optical tissue paper and isopropanol. Folding the tissue then squirting a few drops of isopropanol, the wire will be dragged through multiple times in a straight line, so as not to deform it, which could result in weakened sealing. The indium is then cut to the desired length, looped into a circle and then sliced at an angle to increase the surface area when pressing the two ends together. A teflon spacer inside an aluminium compression flange are tightened to the (WW30530-E1) fused silica windows (see Fig 59) which have the indium rings placed around the chamber exterior, whilst a large indium rectangle is placed on the top for the lid to be pressed down onto it. Both the window seal and the lid are fixed with M4 screws tightened equally. An optional extra was to use vacuum grease (LewVac A-GREASE-DC50) for ease of use but unfortunately this was unable to be done due to time constraints. One particular screw in the lid seemed to be particularly stubborn to remove during testing so future chambers ought to use this grease.

4.5.2 Vacuum System

Every component that will be inside the chamber will also be under vacuum and therefore must be able to maintain this pressure when in use or else this leads to an instability of the 2.6 µm laser. The two holes (ConFlat Flange vacuum joint) on the side of the chamber (Fig 58) are designed to conjoin with a DN16CF connection, in this case two LewVac FL-T16CF flanges.

The peltier element is attached to the base of the cavity (see Fig 62) using a vacuum epoxy (TS10) designed for low vapour pressures. It will also need to be connected using suitable wires designed for vacuum as the ones that come packaged with it will outgas so specialised copper wiring is needed (KAPTON® WIRE 0.25mm (30 AWG) 2kVDC 2A L=10m). In addition the solder used must also be suitable for use within vacuum (4-6337-8817 Vacuum solder from Mouser).

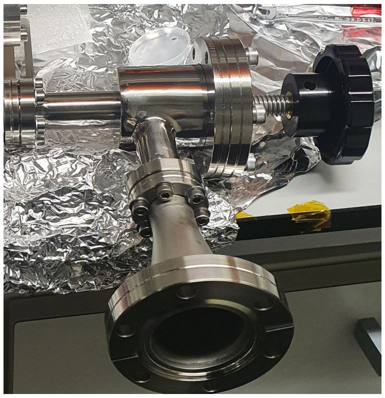

Figure 61: DN16CF Hand Valve.

The interior of the chamber needs to be evacuated of not only air but other smaller elements that may be present, in order to achieve the lower pressures required for stability of the laser. To start with, a turbomolecular pump is used to pump down to a pressure of about 10^{-2} mbar. One side of the chamber will have a stainless steel CF-R rotatable flange (see Fig 61) to be used with this turbomolecular pump which can handle pressures as low as 10^{-10} mbar. Afterwards, the 2.5 l/s ion pump (Mini TiTan MiniDI1VMNNN) is turned on that will reduce the pressure even further to around 10^{-7} mbar, controlled through the use of a DIGITEL controller (SPC-1-P-S-1-UK230-E-S-N). This setup did not need the use of a further vacuum getter pump although one could be used to absorb active gases and reduce the size of the overall setup if desired.

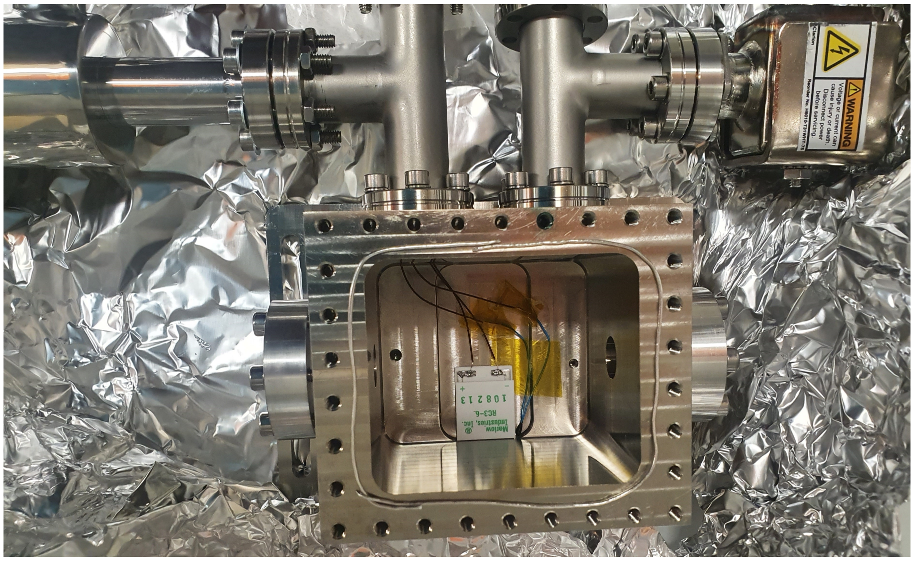

Figure 62: The peltier element (TEC3-6) inside the base of the chamber. The ion pump and feedthrough system for the piezos appear on the top-right whilst the top-left has the peltier element wiring and turbomolecular valve attached.

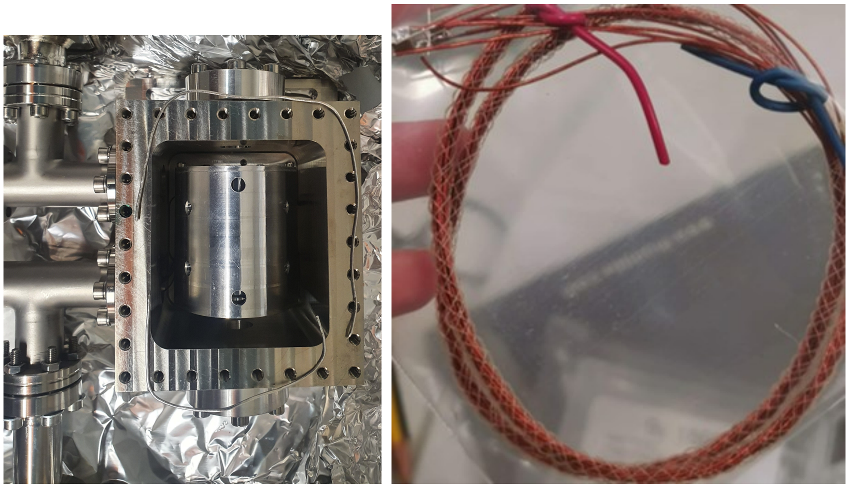

Figure 63: The aluminium outer shell inserted above the peltier element inside the chamber. The LEWVAC feedthrough C9KIT-16CF attached to piezos will be fitted to the tee flange branching to the ion pump.

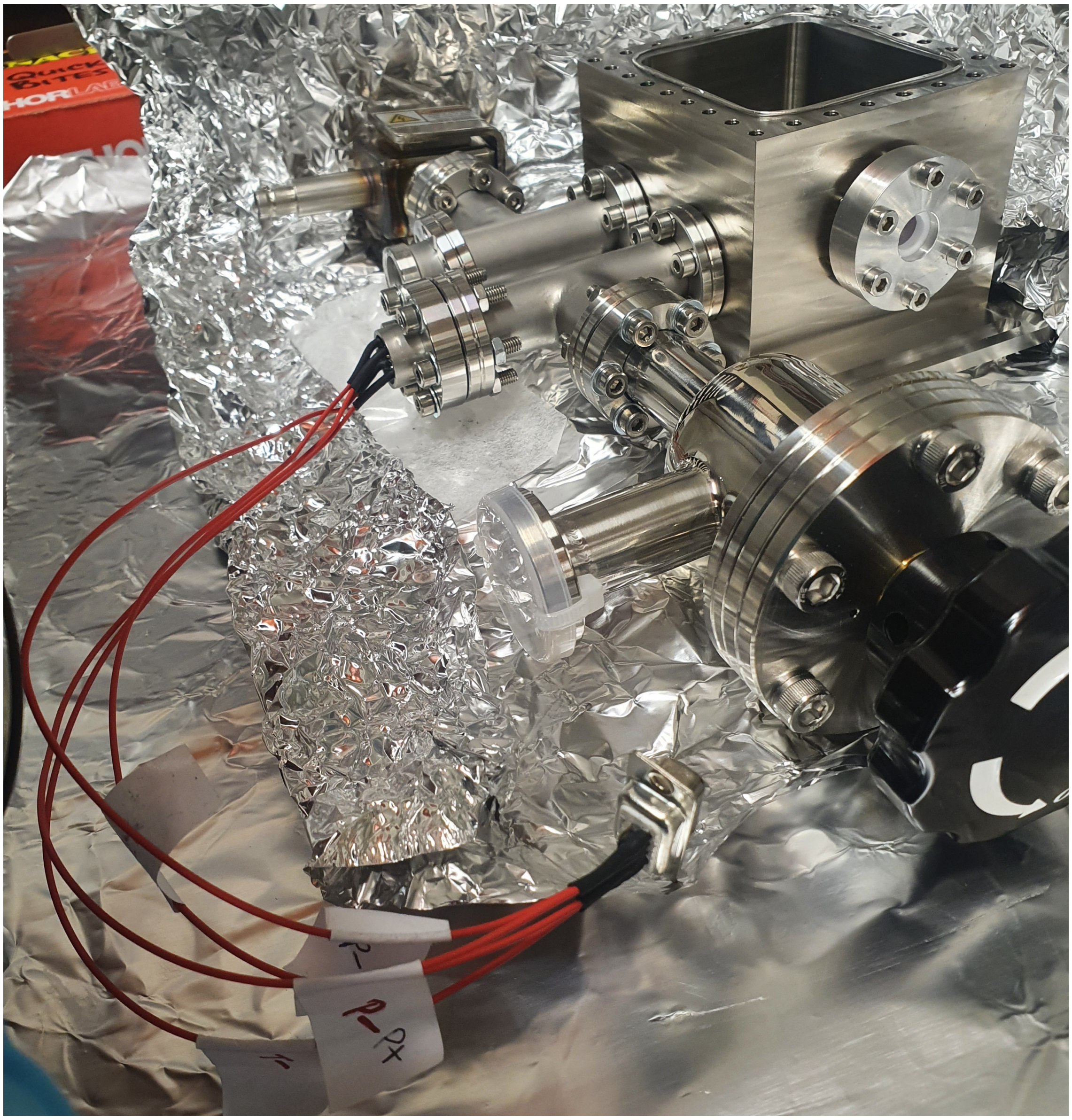

Figure 64: The peltier element's wiring coming out of the DN16CF tee attached to a D-sub connector for use with the temperature controller. The DN16 valve ultra high vacuum is attached the other end of the tee.

4.5.3 Cavity finesse

Finesse is a characteristic of cavities defined as the number of times light will oscillate between the sides before being transmitted or absorbed, determined by how reflective the mirrors used are. Loss, scattering, roughness or non-uniform coating on the mirrors will contribute to the finesse:

$$\mathcal{F} = \frac{\pi}{2\sin^{-1}(\frac{1-R}{2\sqrt{R}})} \tag{78}$$

If $R \approx 1$ by using a Maclaurin series expansion this will become:

$$\mathcal{F} = \pi\frac{\sqrt{R}}{1-R} \tag{79}$$

with R being the mirror reflectivity. The equation ignores other factors that may affect the finesse so only R is dominant. Using the HR value for the constructed cavity yields a value for finesse $\mathcal{F} \sim 15000$.

4.5.4 Temperature drift

The cavity must be maintained at a constant temperature to prevent any drifting of the frequency. The peltier element inside the chamber connects the floor of the aluminium housing to the chamber's floor to aid the flow of heat to the environment till the set temperature is achieved. When using the temperature controller in conjunction with a well defined thermistor, the interior temperature of the chamber and therefore the cavity can be determined. The 10 kΩ thermistor (TDK model number B5786150103F040) is placed inside the chamber along with the peltier element to gauge the temperature with a PID servo loop. The temperature changes according to the Thermistor Beta equation:

$$\frac{1}{T} = \frac{1}{T_0} + \frac{1}{B}\ln\frac{R}{R_0} \tag{80}$$

where T is the ambient temperature in Kelvin, T_0 is room temperature, B is the beta constant, R is the thermistor resistance at ambient temperature and R_0 is the thermistor's resistance at T_0. By using $T_0 = 298.15$ K, $B_{25/100} = 3988$ K, $R_{25} = 10$ kΩ an equation for the temperature in Celsius can be obtained related to the thermistor resistance:

$$R_T = R_{25}\text{exp}\left(\frac{3988}{T+273.15} - \frac{3988}{298.15}\right) \tag{81}$$

The equation is graphed in Fig 65 which uses the ratio of thermistor at room temperature R_{25} and the current resistance R to a temperature T using the Celsius scale. Due to the way beta constants work, the thermistor loses accuracy outside the 25°C - 100°C range but this should be sufficient for experimental use.

The whole assembly of the temperature controller alongside the chamber under vacuum is shown in Fig 66.

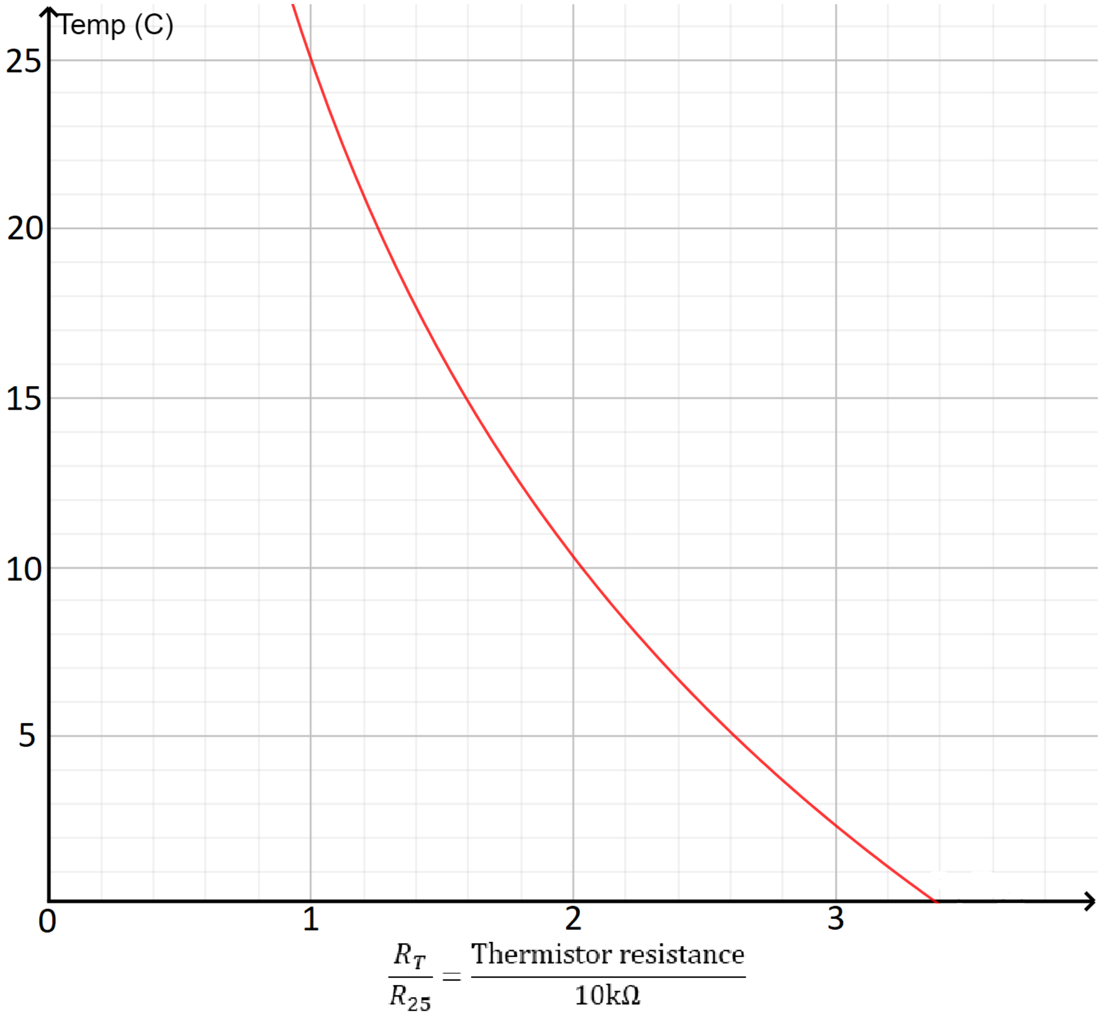

Figure 65: A graph showing the temperature in degrees Celsius versus the ratio of the thermistor's resistance (R_T) and 10 kΩ resistor (R_{25}).

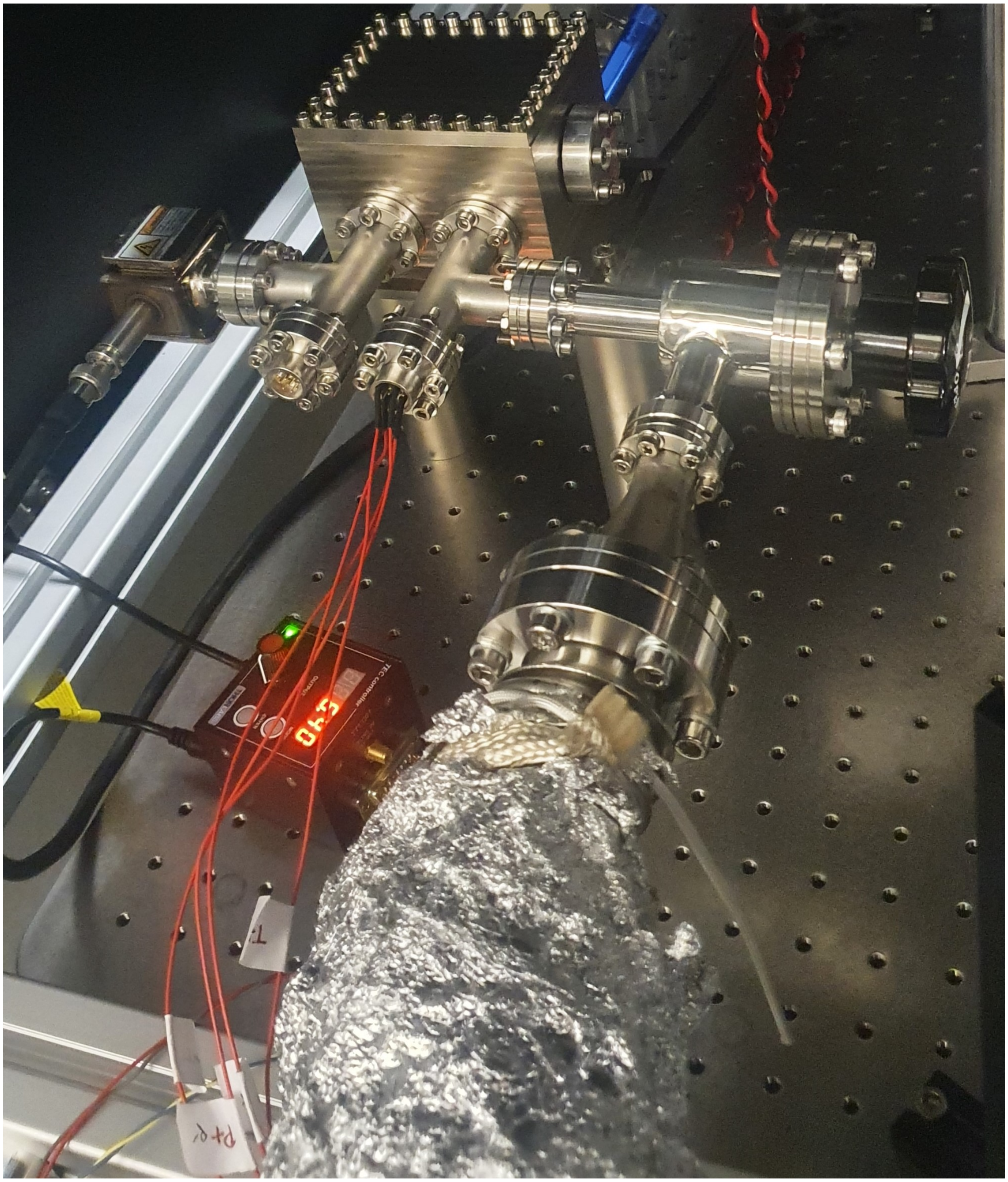

Figure 66: The T-Cube in operation with the assembled chamber raised on the lab bench near the atomic oven. The ion pump is connected through the use of 628-5617 4 pole connections to a DIGITEL controller.

5 Results

5.1 Zeeman slower characterisation

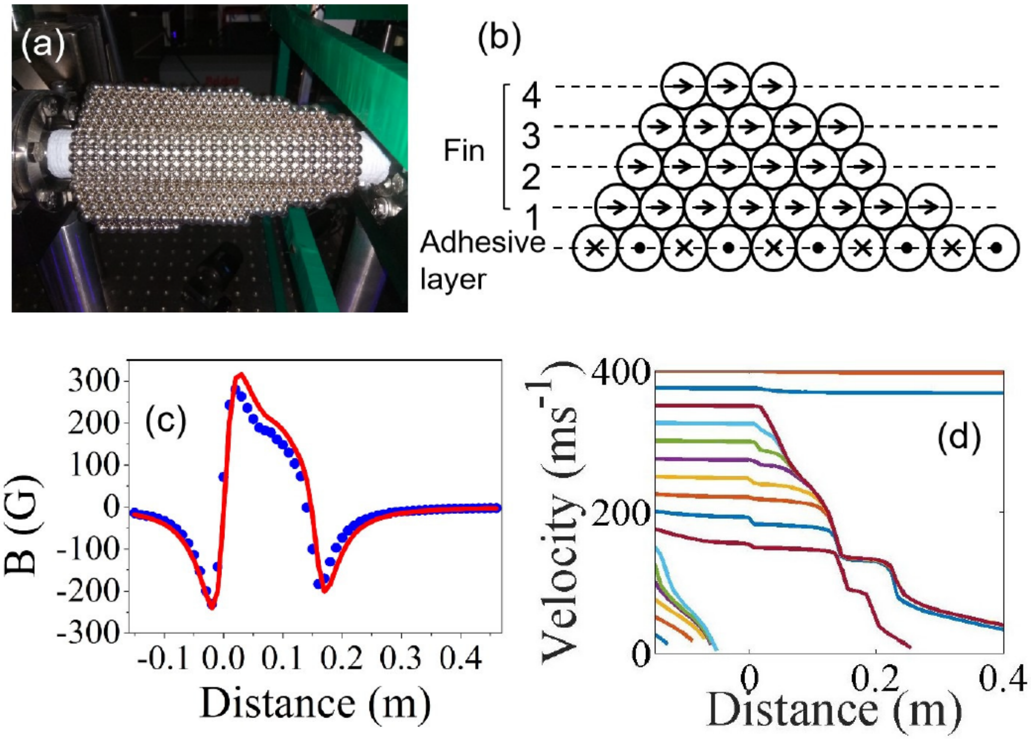

Figure 67: (a) Self-assembled Zeeman slower. (b) Side view of the structure of each fin. (c) The measured (blue dots) and simulated (red curve) longitudinal magnetic field profile of the Zeeman slower. (d) Simulation for the trajectory of atoms with different initial velocities. Plotted by a velocity step of 25 m/s. The centre of MOT is located at the position of 40 cm away from the start of Zeeman slower.[66]

The specific field needed in this experiment was achieved by first building an 'adhesive' cylindrical inner layer of the ball bearings to go around the vacuum nipple and then attaching 'fins' to the to outside as depicted in Fig 67(a). The fins are constructed using five layers of spherical magnets, each layer has: $2 \times 26, 2 \times 23, 2 \times 19, 2 \times 15$ and 2×8 magnets respectively. The first magnet of each layer is located between the first two magnets of the lower layer, leading to a slowly decreasing magnetic field profile. Fig 67(b) shows the side view of the fins. An individual ball bearing has diameter 6 mm and is magnetised the same way along the z-axis, the axis along the atomic beam. Each fin is spaced symmetrically 120° to each other around the cylinder and the z-axis. Fig 67(c) shows the measured magnetic field profile along the z-axis. The Gaussmeter used (GM07 HIRST) limits the accuracy to $< 1\%$. The Zeeman slower is placed between 0 and 15 cm of the z-axis where the magnetic field is positive and has an effective slowing. When the magnetic field is high and negative, it will also have a slowing effect in close proximity to the Zeeman slower. The field can be profiled by using the equation:

$$B_z = \frac{\mu_0 M}{4\pi} \sum_{i=1} \frac{2(z-z_i)^2 - (x-x_i)^2 - (y-y_i)^2}{[(x-x_i)^2 + (y-y_i)^2 + (z-z_i)^2]^{\frac{5}{2}}} \tag{82}$$

here, M is magnetic dipole moment, μ_0 is the vacuum permeability equal to 1.257×10^{-6} H/m, i represents the magnet in the i-th position and N is the total number of magnets, in this case 522. The simulated field and the measured field are in close agreement as seen in Fig 67(c). Testing required simulating the velocity distribution of atoms as they pass through to compare with the measured results of the beam after exiting the Zeeman slower. Fig 67(d) shows that atoms with velocities between 200 m/s and 350 m/s are slowed to be captured within the MOT at a location 40 cm away from when they are first slowed by the Zeeman slower. Anything traveling at speeds below 200 m/s stop well before reaching the trapping region in the MOT. The capture velocity could be increased with the use of more magnets.
Probing the $^1S_0 \rightarrow {}^1P_1$ transition with the use of the 461 nm laser, angled at 45°to the atomic flux allows measurement of the velocity distribution. The most likely velocity is 94 m/s and the width is 26 m/s by use of Zeeman slower. Before the Zeeman slower the velocities were 400 m/s with a width of 370 m/s, so the slower is having a large impact on the capture rate. Overall use of the Zeeman slower causes 34% of the atomic source to finally be caught.
The method of absorption spectroscopy to measure the speeds is the same as Marco Menchetti's thesis[85]. The oven setting is 2.48 A with the signal at maximum. The absorption signal is used to calibrate the fluorescence signal that is sent to a PMT that is set to take light emitted by the atoms. The fluorescence signal will then be used to measure the atomic flux at smaller current values, where the signal to noise ratio is too small to measure it using absorption spectroscopy.

5.2 Performance of MOT

Fig 68 shows the active blue MOT capturing a small cloud of Sr atoms in the middle of the Science chamber. The setup of the experiment requires the oven to be heated to 560°C which leads to an atomic flux of 2.8×10^{11}, able to be increased through more heating at higher temperatures. The 6 orthogonal 461 nm laser beams have a combined intensity of 19 mW/cm^2 ($\sim 0.5 I_{sat}$), a $\frac{1}{e^2}$ radius 10 mm and a detuning of -40 MHz (1.25Γ). The 707 nm and 2.6 µm repump lasers both have radius $\frac{1}{e^2} = 2$ mm, with a power of 1.2 mW and 2 mW respectively. The magnetic field gradient was 55 G/cm. In Fig 69 the sample of atoms in the gas cloud has been captured by the Zyla 5.5 camera and converted into an image using the bundled Andor Imaging software. The pixel data was converted into a spreadsheet and fed back into a graphing software to produce the image shown.

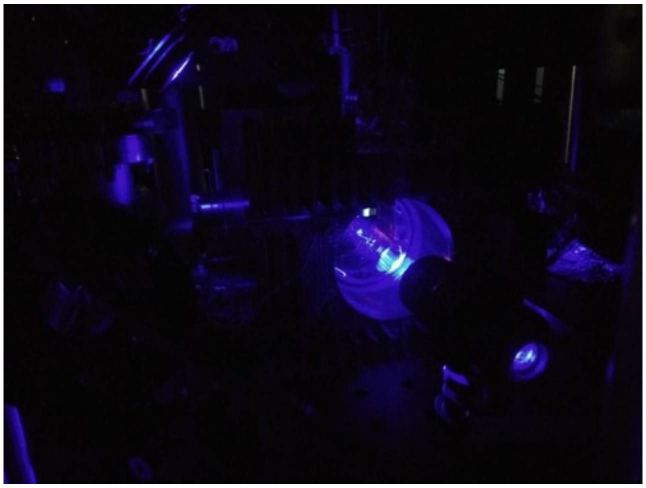

Figure 68: The active blue MOT. The small ball of gas in the centre of the science chamber is the atomic cloud fluorescence.

Time of flight

The time of flight (TOF)[124] method is used to determine the temperature of the sample by looking at the spread of the cloud with no external forces affecting it aside from gravity. It begins with the atoms being loaded into the blue MOT. If the atoms in the cloud have a uniform temperature T_M then the velocity distribution function $f(v)$ will be a Maxwell-Boltzmann distribution:

$$f(v) = \sqrt{\frac{m}{2\pi k_B T_M}} e^{-\frac{mv^2}{2k_B T_M}} \tag{83}$$

with m being the mass of one strontium atom and v is its velocity. Spatial distribution function $f(r)$ of the atoms will follow Gaussian distribution:

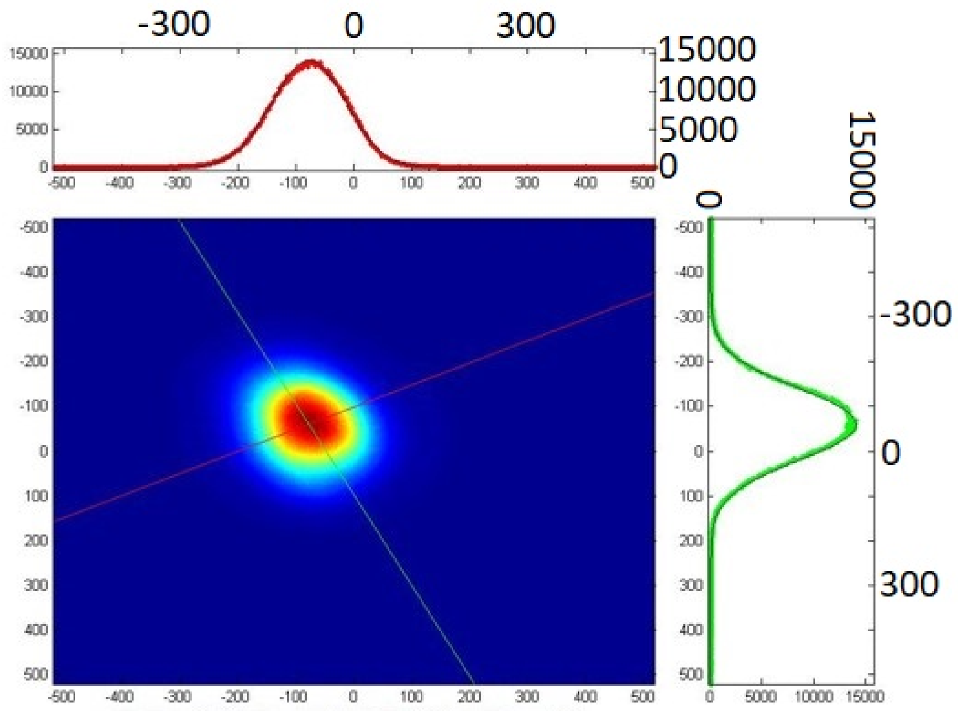

Figure 69: The active blue MOT density captured with the Zyla 5.5 (Andor) camera and software. The atom number is measured in each location and pixel data is sent to a spreadsheet for recreation in graphing software using a 2D Gaussian function to fit.

$$f(r) = \frac{1}{\sqrt{2\pi} r_M} e^{-\frac{r}{2r_M^2}} \tag{84}$$

r is the atom's position within the cloud and r_M is the MOT radius. The next step requires the anti-Helmholtz coils and the cooling laser to be turned off. Without the field or laser the atomic cloud will begin to expand and at a time t later the atom will have moved from a position r_i to final position $r_t = r_i + vt$. The position distribution at this time t is given by:

$$f'(r_i, t) = \int_{-\infty}^{\infty} f(r_i) f(v) dr_i = \int_{-\infty}^{\infty} f(r_i) f\left(\frac{r_t - r_i}{t}\right) dr_i = f(r_i) * f(v) \tag{85}$$

This result leads to the MOT radius becoming:

$$r^2(t) = r_0^2 + \left(\frac{k_B T_M}{m}\right) t^2 \tag{86}$$

with r_0 being the radius at time $t = 0$.

Next the blue laser needs to be switched on so the imaging camera can be used to take a snapshot of the image at the desired time t. By comparing the picture of the MOT before and after the expansion the temperature can be calculated using (86). Fig 70 shows the repeated measurement of the cloud after several milliseconds of expanding to create a time lapse. In Fig 71 the values for the terms in equation (86) are plotted as a straight line graph. The calculation of the temperature for the blue MOT in this instance returned a value of 2.5 ± 0.4 mK which will be improved in future testing due to problems in power output for the 461 nm laser.

Fig 72(a) shows the blue MOT being loaded under several conditions. With no Zeeman or repump lasers, only 2×10^6 atoms are trapped in the MOT. If the Zeeman laser is active at 15 mW then the number obtained increases 20 times. Turning on the 707 nm repump will double the atomic number whilst dual repumps increase the steady-state atom number further. It is clear to see that using 707 nm in conjunction with 679 nm repumps is inferior to when 707 nm is utilised alongside 2.6 µm repumps. By fixing the 707 nm power both of the remaining repumps are set to an intensity of 16 mW/cm^2; $3 \times 10^4 I_{sat}$ for 2.6 µm and $27 I_{sat}$ for 679 nm. The 2.6 µm has a saturation intensity of 0.54 µW/cm^2 whilst the 679 nm has 0.6 mW/cm^2. The graph shows an improvement of factor 16 when using the 679 nm + 707 nm setup but a much improved factor of 23 when using the 2.6 µm + 707 nm setup. The ratio between the two is $\frac{23}{16} \approx 1.4$.
The blue MOT was operated with the 2.6 µm and 707 nm dual repumps alongside the atomic source oven at 560°C, the Zeeman slower with laser power $P_{MOT} = 60$ mW for the total MOT beams and $P_{ZS} = 20$ mW for the Zeeman slower beam opposing the atomic flux. These parameters lead to a peak steady-state atom number of 9.8×10^8 and atomic density 1.4×10^{11} cm^{-3}, limited by the maximum power of the cooling laser. The MOT loading rate is 3×10^9 s^{-1}, loading time 0.3 s and lifetime for the MOT 1.1 s. After improvements in output power for the 461 nm laser had been made, thanks to repairs from M2 lasers, another TOF measurement was carried out. At this time the motor controller had been setup to be controlled via computer to eliminate the human error from turning the valve on the shutter shown in Fig 73. It can operate at set speeds but there was little available aside from start and stop, so macros were created to refine the movement to be exactly the necessary angle of rotation and stop immediately. Shown in Fig 72(b) more images of the expansion were captured and the temperature was 1.12 mK.
The number of atoms trapped in the blue MOT are around 1 billion.

Magnetic Trapping

More characterisation of the setup can come from loading the atoms into the magnetic trap of the $^3P_2$ state using the $^1S_0 \rightarrow ^1P_1$ cooling cycle. The $^3P_2$ state has a large magnetic moment of $3\mu_B$ plus a long radiative lifetime of about 17 minutes which allows this trapping to occur. The method involves continuous loading to $^3P_2$ state during the MOT process, holding in an anti-Helmholtz magnetic field for 1.3 s. Next, the 461 nm laser and the magnetic field are switched off, again after 1.3 s. Last is to turn on the 707 nm laser, the probe laser and the camera after an amount of time t_{hold} in order to detect the ^{3}P$_2$ atoms trapped via the transitions ^{3}P$_2$ $\rightarrow^3$P$_1$ $\rightarrow^1$S$_0$. The magnetic field gradient 50 G/cm gives a magnetic trap depth 38 mK. In Fig 74(a) the atom number for the trap is shown versus time in seconds. The lifetime comes out as 1.1 s whilst the loading time is 0.5 s. Fig 74(b) shows the timing sequence used. A back to back sequence of decay and loading of the MOT is shown in Fig 75 yielding a lifetime of 1.09 s.

Atom number calculation

The Andor camera software calculates the atom number N based on the following equation:

$$N = \frac{n\left(\frac{4R^2}{r^2}\right)}{P} \tag{87}$$

where:

$$P = \frac{\frac{1}{2}\left(\frac{I}{I_s}\right) G \times 10^6}{1 + \left(\frac{I}{I_s}\right) + D^2 + G^2} \tag{88}$$

where n is number of detected photons, R is the focal length of the lens, r is distance from lens to atom, I is intensity, I_s is saturation intensity, G is the natural linewidth (32 MHz) and D is the detuning (80MHz).

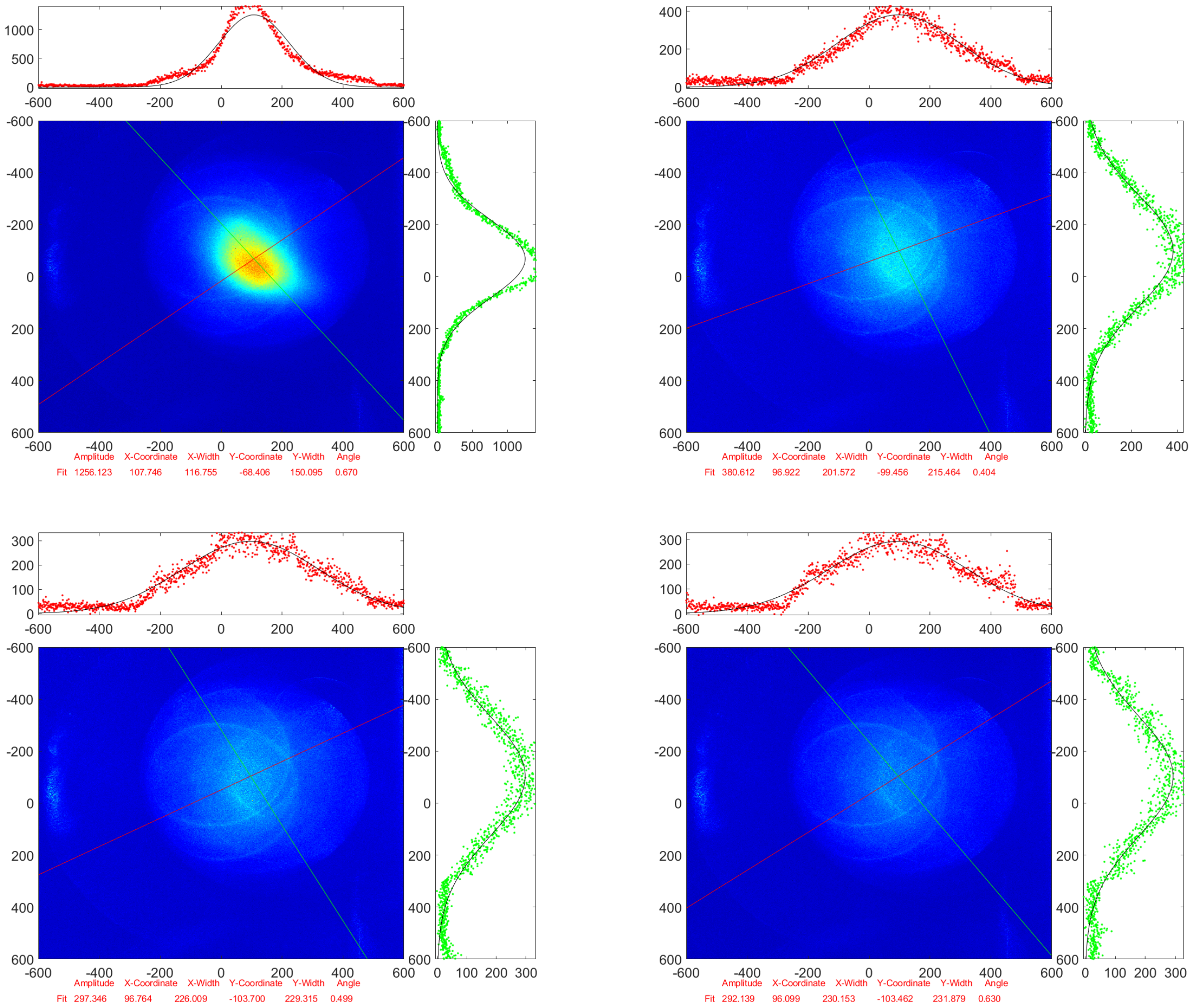

Figure 70: The time of flight (TOF) for the blue MOT. The atoms are thrown up as a collective and allowed to spread as they fall in order to measure the temperature. Multiple measurements were taken by turning off the field and laser then fluorescing the sample after several milliseconds with the 461 nm laser.

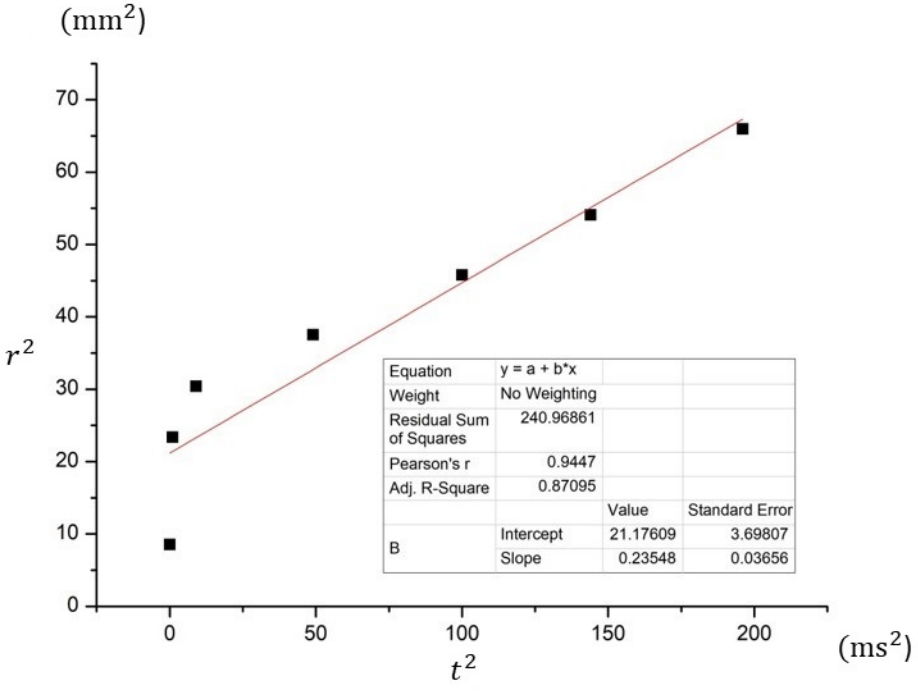

Equation	y = a + b*x		
Weight	No Weighting		
Residual Sum of Squares	240.96861		
Pearson's r	0.9447		
Adj. R-Square	0.87095		
		Value	Standard Error
B	Intercept	21.17609	3.69807
	Slope	0.23548	0.03656

Figure 71: $P_{MOT} = 45$ mW, $P_{ZS} = 15$ mW. By fitting as a straight line for equation (86), the temperature of blue MOT is obtained, which is 2.5 ± 0.4 mK

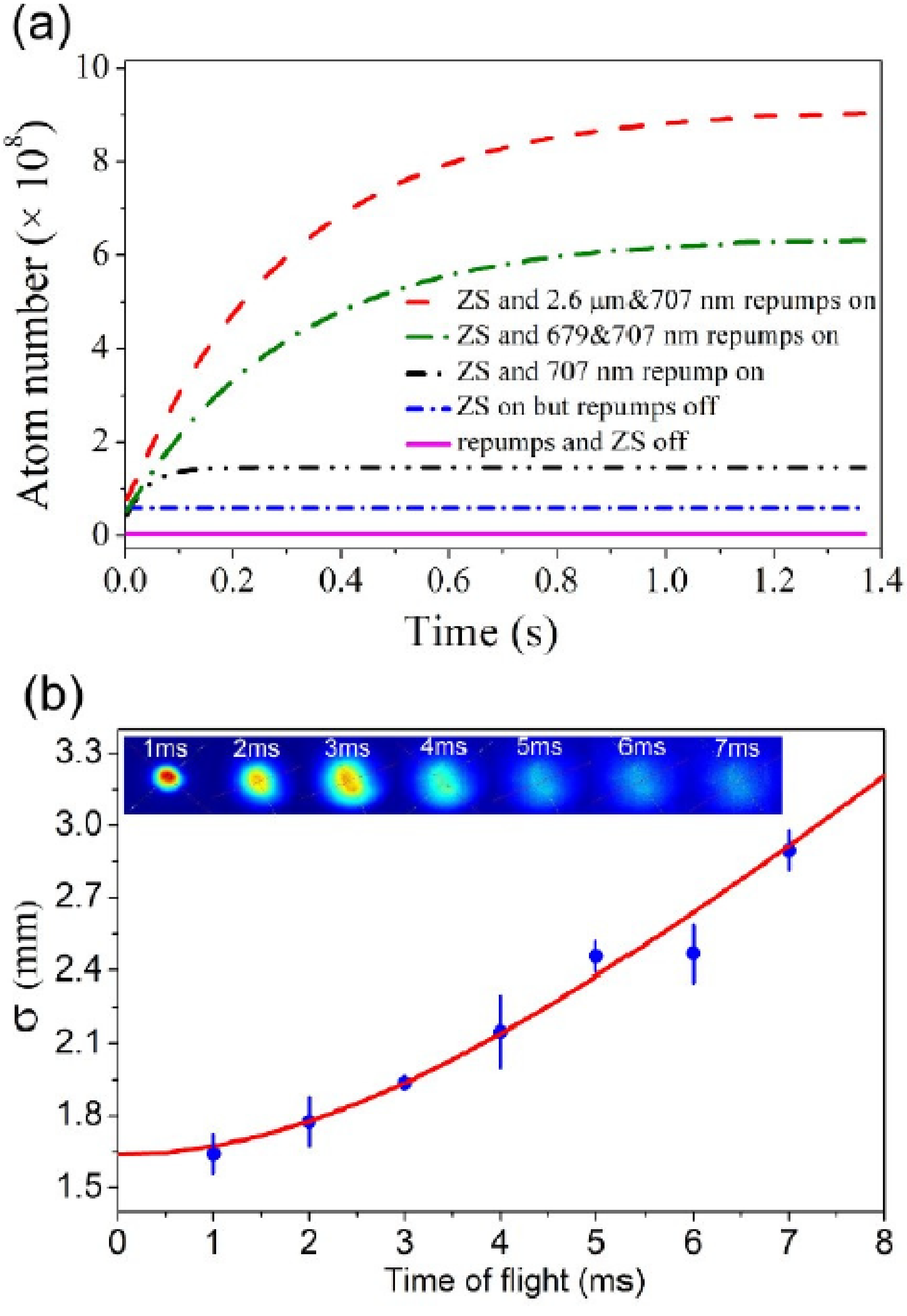

Figure 72: (a) The dependence of atom number in blue MOT on Zeeman slower beam and two repumping beams. The fluorescence of the sample is captured by the CCD camera to determine atom number. (b) The radius of blue MOT as a function of time of flight. Inset: the images of atomic cloud at different time of flight.[66]

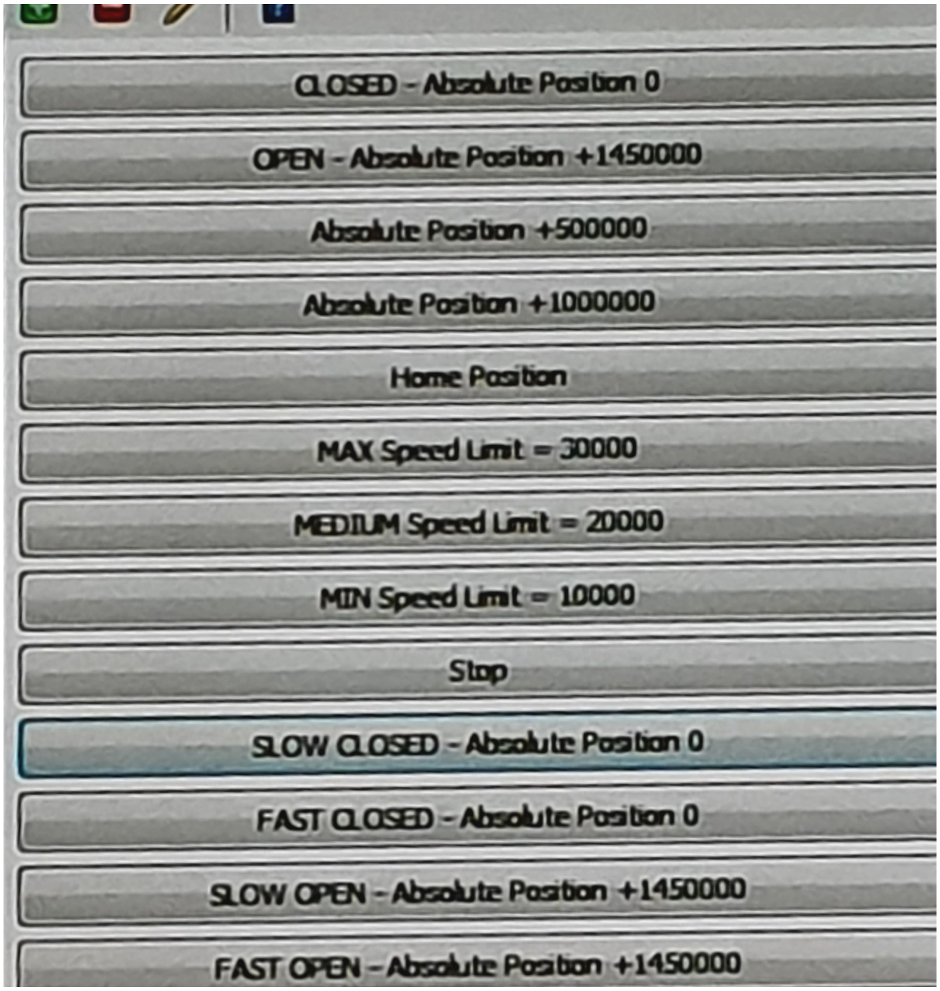

Figure 73: The motor controller can be used to rotate the shutter valve at differing speeds. The latest TOF measurements used this to reduce the errors from turning by hand.

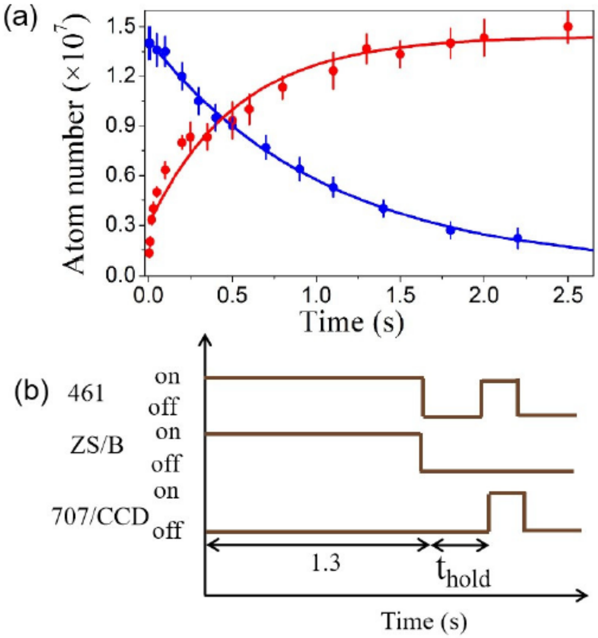

Figure 74: (a) Measuring of atom number for $^3P_2$ magnetic trap during the decay (blue solid circles) and the loading phase (red solid circles). Fits are shown by solid curves. (b) The magnetic trap decay timing sequence. ZS: Zeeman slower; B: magnetic field gradient; CCD: charge coupled device camera. In the lifetime measurement, the atoms are continuously loaded into $^3P_2$ for 1300 ms.[66]

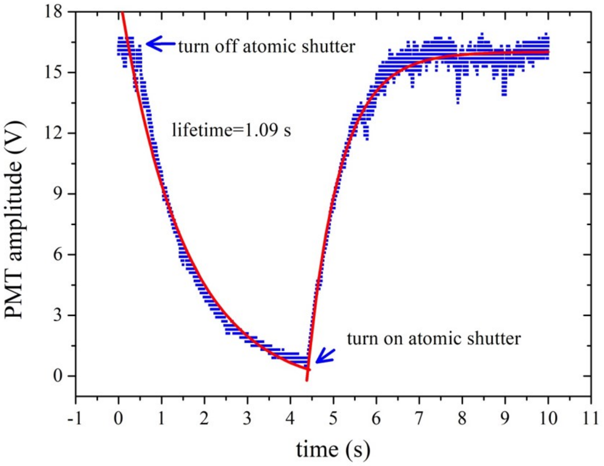

Figure 75: When turning off atomic shutter (all lasers and magnetic field are on), the PMT signal will be decreased; when turning it on again (others are kept on), the signal will increase. By fitting with an exponential function, the lifetime of the blue MOT is 1.09 s.

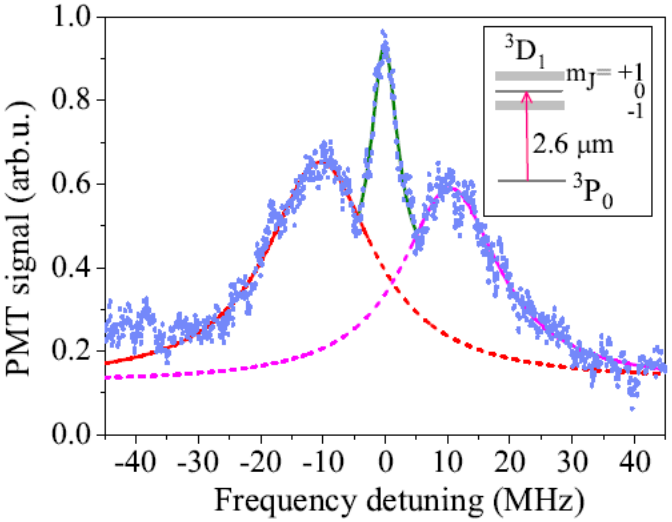

Figure 76: A typical resolved-sideband Zeeman spectroscopy of $^3P_0 \rightarrow ^3D_1$. Experimental data (blue dots) are fitted with three independent Lorentz functions (colourful curves). This is because there are three separate peaks from left to right which correspond to $m = 0 \rightarrow m' = -1, 0, +1$ transitions. Inset: the Zeeman sublevels of $^3D_1$.[66]

5.3 Landé g factor measurement

Previously, alkaline earth metals' g factors for $^1S_0$ and $^3P_{0;1;2}$ had already been experimentally determined to estimate the Zeeman shift in optical clocks[125]. Something that had not been measured was the g factors of ^3D states. This will be a new measurement of the Landé g factor of $^3D_1$ state using cold ^{88}Sr atoms confined inside a blue MOT. The resolved-sideband Zeeman spectroscopy will be key to the g factor measurement.

The first step to get this measurement was by having ^{88}Sr atoms continuously loaded in the blue MOT. Meanwhile, the 707 nm repump laser is locked and kept on the whole time. Secondly, a neutral density filter is inserted into the reflected MOT beam parallel to the anti-Helmhotz coil axis. This will cause an imbalance between the traveling-wave components. The atoms are propelled towards the reflected beam side because of the intensity imbalance which is the result of split Zeeman sublevels by the non zero magnetic field. The third step was to switch on the 2.6 µm laser to excite the $^3P_0$ atoms to $^3D_1$ and carry out the Zeeman spectroscopy by the electron shelving methods[126]. The 2.6 µm laser power was 80 µW and beam size was 2.3 mm. The laser was scanned at speed 8 MHz/s. The magnetic field gradient was 45 G/cm.

In Fig 76 the typical resolved-sideband Zeeman spectroscopy of $^3P_0 \rightarrow ^3D_1$ is shown. There are three peaks which correspond to the $m = 0 \rightarrow m' = -1, 0, +1$ from left to right. A NE02A filter (OD=0.2) is inserted which could produce a 37% difference in intensity.

The three peaks are individually fitted with a Lorentz function. They are broadened by the following effects, all of which are independent of one another: the intensity broadening, the linewidth of the 2.6 µm laser and the Doppler broadening. More broadening on the side peaks occurs due to variation of the magnetic field across the atomic cloud.

The Doppler broadening is about 175 kHz at a temperature of 1.1 mK. Intensity broadening is calculated to be 4.4 MHz using $\Delta\nu = \Delta\nu_N\sqrt{1+\frac{I}{I_{sat}}}$, with $\Delta\nu_N$ as the natural linewidth of the ^{3}D$_1$ state, I_{sat} is the saturated intensity for transition ^{3}P$_0$ $\rightarrow^3$D$_1$. The full width at half maximum (FWHM) of the three peaks are 18.3 MHz, 6.3 MHz and 14.7 MHz from left to right. The frequency shift of the left peak is 10.2 MHz from centre peak, whilst the right is shifted 10.8 MHz. The measured difference between left and right peaks in FWHM and shift is brought about via fitting uncertainty and the induced magnetic field variation across the atomic cloud during the laser scanning time period.

The peak splittings and widths are calculated from the measured displacement, S, and atomic cloud radius, $\frac{\Delta S}{2}$:

$$S = \frac{\Delta_S h}{g\mu_B m_J B'_Z} \tag{89}$$

$$\frac{\Delta S}{2} = \frac{\Delta_W h}{g\mu_B m_J B'_Z} \tag{90}$$

with Δ_S and Δ_W being the peak splitting and the FWHM difference between the central peak and side peaks, μ_B is the Bohr magneton, $m_J = \pm 1$ is the magnetic quantum number. For this experiment $S = 2.98$ mm and $\frac{\Delta S}{2} = 2.6$ mm. Using rate equations[127] [128] the values of $\Delta_S = 9.4$ MHz and $\Delta_W = 8.2$ MHz can be calculated, close to experimentally determined values of $\Delta_S = 10.5$ MHz and $\Delta_W = 10.2$ MHz. One possible reason for this discrepancy could be the magnetic field within the Science chamber is higher than 45 G/cm that was put into the calculation. Looking at the arrangement of components, a likely candidate for this extra field could be one of the ion pumps.

In Fig 77 the plot for Zeeman spectroscopy of ^{3}P$_0$ $\rightarrow^1$D$_1$ is shown. There are three cases: without filter, NE01A filter and NE02A filter with an intensity difference of 0%, 21% and 37% inserted into the reflected beam, parallel to the magnetic field axis. The cloud is shifted toward the reflected beam side in Fig 77(a). When the magnetic field is increased, the side peaks shift further and are more broadened as shown in Fig 77(b). When there is no filter there are still two side peaks visible that come about from an imperfect magnetic trap which is splitting the sublevels. The 2.6 µm laser used had Doppler broadening $\Delta\nu_d = 432$ kHz, Power broadening $\Delta\nu_p = 24$ MHz and Zeeman broadening $\Delta\nu_z = 0.91$ MHz, making power broadening the largest contributor to inaccuracies in results.

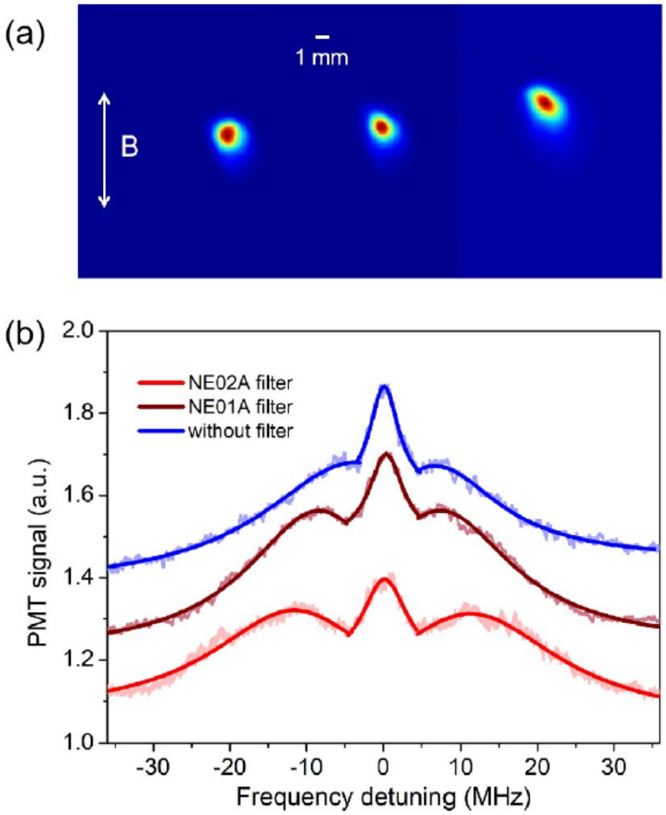

Figure 77: (a) Left: Atomic cloud without filter. Middle: Atomic cloud with small magnetic field and NE01A filter. Right: Atomic cloud with higher magnetic field and NE02A filter (the one used for Fig 76). The cloud is shifted towards the reflected beam side which is parallel to the magnetic field direction. (b) Zeeman spectroscopy for the above three scenarios. The light dots represent the experimental data and dark curves are fitted results for all three cases. The Zeeman sublevel splitting is larger and the signal amplitude weakens as the magnetic field increases.[66]

The value of g_J is measured in experiments by use of frequency splitting at various magnetic fields using $g = \frac{\Delta\nu h}{\mu_B B}$, with $\Delta\nu$ being the frequency splitting of the side peak with respect to the central peak. g will be calculated by calibrating the frequency splitting and the magnetic field. The frequency splitting can be calibrated using a 80 MHz frequency interval between the carrier and the modulated side band. The magnetic field is worked out from the equation, $B = cB'\Delta p$, with $c = 38$ µm/pix, B' is the magnetic field gradient and Δp is the change in the number of pixels. 7 measurements were taken and averaged to obtain a value of $g_J = 0.4995$.

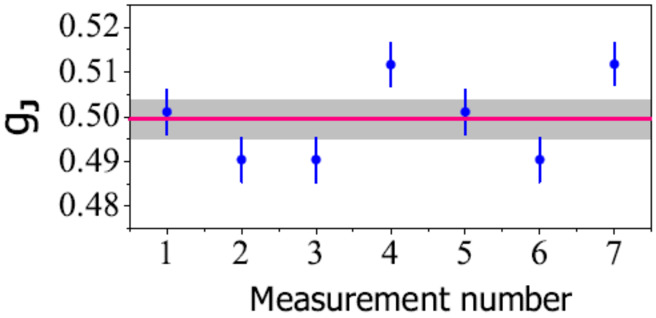

Figure 78: Summary of measurements of the Landé g factor of ^{3}D$_1$. The error bars show the uncertainty of the experiment. The soild line and the gray area represent the mean measured value and the $1-\sigma$ confidence interval. $\sigma = 0.0044$[66]

The g_J for ^{3}D$_1$ is also calculated using Russel-Saunders approximation[129]:

$$g_J = g_L \frac{J(J+1) + L(L+1) - S(S+1)}{2J(J+1)} + g_S \frac{J(J+1) + S(S+1) - L(L+1)}{2J(J+1)} \tag{91}$$

L is the total orbital angular momentum quantum number, S is the total spin quantum number, J is the total angular momentum quantum number. $g_L = 1$ and $g_S = 2 \times 1.0011597$ for this experiment[130]. This leads to a calculated value of $g_J = 0.4988$ for the ^{3}D$_1$ state of ^{88}Sr. The measured value for g_J is shown in Fig 78; the mean value experimentally is 0.4995(44) which is remarkably close to the theoretical calculated value of 0.4988. The error bars show the uncertainty which mostly come about from the frequency splitting calculation and the magnetic field. This value can be refined further when the 2.6 µm laser is locked to the cavity.

The work done throughout the course of this thesis has been published in papers and presented at conferences:

- S. Zhang, P. Ramchurn, M. Menchetti, Q. Ubaid, J. Jones, K. Bongs and Y. Singh, "Novel repumping on $^3P_0 \rightarrow ^3D_1$ for Sr magneto-optical trap and Landé g factor measurement of $^3D_1$", (2020). J. Phys. B: At. Mol. Opt. Phys. 53 235301
- Sh. Zhang, P. Ramchurn, S. Ganesh, K. Bongs, Y. Singh, "Light Scattering from Sr Atoms in a Two-Dimensional Optical Lattice", (2021). Quantum Optics X, 5-11 September 2021, Toruń, Poland.
- S. Zhang, P. Ramchurn, K. Bongs, Y. Singh, "Simulation of Dipole-Dipole Interactions With Ultracold Sr in an Optical Lattice", (2021). 2021 Joint Conference of the European Frequency and Time Forum and IEEE International Frequency Control Symposium (EFTF/IFCS)
- S. Zhang, P. Ramchurn, K. Bongs, Y. Singh, "The Measurement of Landé Factor of $^3D_1$ with Cold ^{88}Sr Atoms", (2020). 2020 Joint Conference of the IEEE International Frequency Control Symposium and International Symposium on Applications of Ferroelectrics (IFCS-ISAF)
- S. Zhang, P. Ramchurn, K. Bongs, Y. Singh, "Characterization of ultracold 88Sr atoms for the dipolar interaction of the 3P0-3D1 transition", (2020). APS Division of Atomic, Molecular and Optical Physics Meeting Abstracts

6 Conclusion

Looking back on the strontium LRI project I remember all the hurdles that the group has overcome and still managed to accomplish some milestones. The thesis introduced the setup required for confining a sample of Sr atoms inside of a trap through cooling with the aim to develop a BEC through the additional cooling with a dipole laser. Steps towards achieving the BEC and ultimately probing strontium for evidence of long-range interactions have been undertaken so that those who wish to utilise the current setup may find it in a better state than it was 3 years ago:

- The experimental confirmation of the Landé g factor
- The vacuum system has been upgraded to a new ion pump with 80 times the pump speed to reduce external effects upon the blue MOT atoms in the Science chamber
- Motion manager software macros have been implemented to assist the TOF measurement by automatically twisting the valve with the push of a button
- The 2.6 µm laser was free running but now has a cavity and chamber to lock it into place for an increase in stability

- The current atom number for ^{88}Sr is $\sim 10^9$ cooled down to 1.1 mK with a density for the cloud 1×10^{11} cm^{-3}. When switching to broadband red MOT the transfer efficiency was 30% - 40%. From broadband to single frequency red MOT the efficiency was 90%.
- The 1.06 µm dipole laser has been installed and is operating at maximum power 20 W safely

6.1 Unfinished tasks

I successfully worked alongside my colleagues to get the systems up and running again after returning to the labs; since being inactive throughout lockdown. Naturally there are some things left unfinished:

- Characterising the 2.6 µm laser
- Create optical dipole trap to perform a BEC with ^{84}Sr
- Perform the blue detuned optical lattice
- Make further improvements to the vacuum system by adding two additional ion pumps to the Science chamber also rated for 200 l/s

Overall I thoroughly enjoyed the experimental side of physics, having previously only had a background in mathematics and theoretical physics. It was not obvious at first that a lot of time is spent setting up an experiment rather than just carrying it out. However, the research into the world of cold atoms has revealed a new side to reality that would otherwise have been overlooked or neglected. Strontium and many other alkaline earth metals will be the subject of many additional experiments to investigate the ultracold frontier with atoms. Having worked on the project for 3 years it is apparent that such steps are hardly ever made alone, considering the input from others working in the cold atoms group have contributed, both small and large.

The first step for the project from here on is to lock the 2.6 µm laser to the cavity. Once this is done the next task will be to achieve the BEC using strontium-84. From here there are two options: i) either proceed to achieve long-range interactions or ii) to load the BEC into an optical lattice at 412 nm, thereby putting the atoms into the Mott insulator state and then drive the long-range interactions using the 2.6 µm laser.

For the future detection of LRI, the fluorescence of the linewidth broadening will be measured. It is expected that the frequency will shift and the peak is suppressed. At the current rate of progress we expect around 2 years to detect preliminary readings for LRI.

References

[1] H. Lyons, "The Atomic Clock: A Universal Standard of Frequency and Time", (1950). The American Scholar Vol. 19, No. 2 (SPRING 1950), pp. 159-168

[2] F. Trixler, "Quantum Tunnelling to the Origin and Evolution of Life", (2013). Current Organic Chemistry. 17 (16): 1758–1770.

[3] M. Lombardi, "The accuracy & stability of quartz watches", (2008). Horological Journal, 150(2):57, 2008. 3

[4] R. Hobson, "An Optical Lattice Clock with Neutral Strontium", (2016). University of Oxford.

[5] NASA, "What is an Atomic Clock?", (2019). [Online] Available: https://www.nasa.gov/feature/jpl/what-is-an-atomic-clock

[6] P. Delva and J. Lodewyck, "Atomic clocks: new prospects in metrology and geodesy", (2013). Acta Futura, Issue 7, p. 67-78 [Online] Available: arXiv:1308.6766 [physics.atom-ph]

[7] N. Hinkley, J. A. Sherman, N. B. Phillips, M. Schioppo, N. D. Lemke, K. Beloy, M. Pizzocaro, C. W. Oates & A. D. Ludlow, "An atomic clock with 10(-18) instability", (2013). Science (New York, N.Y.), 341(6151), 1215–1218. https://doi.org/10.1126/science.1240420

[8] J. Terrien, "News from the International Bureau of Weights and Measures", (1967). Metrologia 3 23

[9] J. C. Hafele and R. E. Keating, "Around-the-World Atomic Clocks: Observed Relativistic Time Gains", (1971). Science, New Series, Vol. 177, No. 4044 (Jul. 14, 1972), pp. 168-170

[10] J. C. Hafele, "Performance and results of portable clocks in aircraft", (1971). [Online] Available: https://web.archive.org/web/20170126213131/
http://tycho.usno.navy.mil/ptti/1971papers/Vol%2003_17.pdf

[11] J. L. Hall, M. Zhu, and P. Buch, "Prospects for using laser-prepared atomic fountains for optical frequency standards applications", (1989). J. Opt. Soc. Am. B 6, 2194-2205

[12] W. Ertmer, R. Blatt, and J. L. Hall, "Some Candidate Atoms and Ions for Frequency Standards Research using Laser Radiative Cooling Techniques", (1984). Prog. Quant. Electr. 1984, Vol. 8, pp. 249-255

[13] D. B. Newell and E. Tiesinga, eds. "The International System of Units (SI)", (2019). (NIST Special publication 330, 2019 ed.)

[14] A. Griesmaier, J. Werner, S. Hensler, J. Stuhler and T. Pfau, “Bose-einstein condensation of chromium”, (2005). Phys. Rev. Lett., vol. 94, p. 160 401, 16 Apr. 2005. [Online]. Available: https://link.aps.org/doi/10.1103/PhysRevLett.94.160401.

[15] J. L. Bohn, A. M. Rey, and J. Ye, “Cold molecules: Progress in quantum engineering of chemistry and quantum matter”, (2017). Science, vol. 357, no. 6355, pp. 1002–1010, 2017, issn: 0036-8075. eprint: http://science.sciencemag.org/content/357/6355/1002.full.pdf. [Online]. Available: http://science.sciencemag.org/content/357/6355/1002.

[16] D. Comparat and P. Pillet, “Dipole blockade in a cold Rydberg atomic sample”, (2010). *J. Opt. Soc. Am.* B, vol. 27, no. 6, A208–A232, 2010. [Online]. Available: http://josab.osa.org/abstract.cfm?URI=josab-27-6-A208.

[17] M. Mauck, “Knife-edge profiling of Q-switched Nd:YAG laser beam and waist”, (1979). Appl. Opt., vol. 18, no. 5, pp. 599–600, Mar. 1979. [Online]. Available: http://ao.osa.org/abstract.cfm?URI=ao-18-5-599.

[18] G. H. Chapman, “Knife Edge measurement of Gaussian Beam”. Simon Fraser University. School of Engineering Science. [Online] Available: http://www.sfu.ca/ gchapman/e894/e894la1-extra4.pdf

[19] M. Schioppo, “Development of a transportable strontium optical clock”, (2010). PhD thesis, Universit ́a degli studi di Firenze, Dipartimento di Fisica e Astronomia, 2010. Applied Physics B volume 117, pages1107–1116 (2014)

[20] T. Hänsch and A. Schawlow, “Cooling of gases by laser radiation”, (1975). Optics Communications, vol. 13, no. 1, pp. 68 –69, 1975, issn: 0030-4018. [Online]. Available: http://www.sciencedirect.com/science/article/pii/0030401875901595.

[21] D. J. Wineland, R. E. Drullinger, and F. L. Walls, “Radiation-pressure cooling of bound resonant absorbers”, (1978). Phys. Rev. Lett., vol. 40, pp. 1639–1642, 25 1978. [Online]. Available: https://link.aps.org/doi/10.1103/PhysRevLett.40.1639.

[22] D. J. Wineland and W. M. Itano, “Laser cooling of atoms”, (1979). Phys. Rev. A 20, 1521 – Published 1 October 1979

[23] W. D. Phillips and H. Metcalf, “Laser deceleration of an atomic beam”, (1982). Phys. Rev. Lett., vol. 48, pp. 596–599, 9 Mar. 1982. [Online]. Available: https://link.aps.org/doi/10.1103/PhysRevLett.48.596.

[24] S. Chu, L. Hollberg, J. E. Bjorkholm, A. Cable, and A. Ashkin, “Three-Dimensional Viscous Confinement and Cooling of Atoms by Resonance Radiation Pressure”, (1985). Phys. Rev. Lett., vol. 55(1), pp. 48-51, 1985. [Online]. Available: https://journals.aps.org/prl/pdf/10.1103/PhysRevLett.55.48

[25] S. Chu, J. E. Bjorkholm, A. Ashkin, and A. Cable, "Experimental observation of optically trapped atoms", (1986). Phys. Rev. Lett., vol. 57, pp. 314–317, 3 Jul. 1986. [Online]. Available: https://link.aps.org/doi/10.1103/PhysRevLett.57.314.

[26] E. L. Raab, M. Prentiss, A. Cable, S. Chu, and D. E. Pritchard, "Trapping of neutral sodium atoms with radiation pressure", (1987). Phys. Rev. Lett., vol. 59, pp. 2631–2634, 23 Dec. 1987. [Online]. Available: https://link.aps.org/doi/10.1103/PhysRevLett.59.2631.

[27] M. Boyd, "High Precision Spectroscopy of Strontium in an Optical Lattice: Towards a New Standard for Frequency and Time", (2007). ProQuest Dissertations And Theses; Thesis (Ph.D.)–University of Colorado at Boulder, 2007.; Publication Number: AAI3284498; ISBN: 9780549315513; Source: Dissertation Abstracts International, Volume: 68-11, Section: B, page: 7388.; 245 p.

[28] E.S. Shuman, J.F. Barry and D. DeMille, "Laser cooling of a diatomic molecule", (2011). Nature. 467 (7317): 820–823. arXiv:1103.6004

[29] Massachusetts Institute of Technology. "Laser-cooling Brings Large Object Near Absolute Zero", (2007). ScienceDaily. [Online] Available: www.sciencedaily.com/releases/2007/04/070406171036.htm

[30] S. R. Bowman, "Lasers without internal heat generation", (1999). IEEE Journal of Quantum Electronics, vol. 35, no. 1, pp. 115-122, Jan. 1999, doi: 10.1109/3.737628.

[31] Denis V Seletskiy *et al*, "Laser cooling in solids: advances and prospects", (2016). Rep. Prog. Phys. 79 096401

[32] S. N. Bose, Zeitschrift für Physik volume 26, pages 178–181 (1924)

[33] A. Einstein, "Quantentheorie des einatomigen idealen Gases", (1925). Sitzungsberichte der Preussischen Akademie der Wissenschaften. 1: 3.,

[34] F. London, "The λ-Phenomenon of Liquid Helium and the Bose-Einstein Degeneracy", (1938). Nature 141, 643–644 (1938). https://doi.org/10.1038/141643a0

[35] F. London, "On the Bose-Einstein Condensation", (1938). Phys. Rev. 54, 947

[36] O. Penrose and L. Onsager, "Bose-Einstein Condensation and Liquid Helium", (1956). Phys. Rev. 104, 576

[37] T. R. Sosnick, W. M. Snow, and P. E. Sokol, "Deep-inelastic neutron scattering from liquid ^{4}He", (1990). Phys. Rev. B 41, 11185

[38] D. M. Ceperley, "Path integrals in the theory of condensed helium", (1995). Rev. Mod. Phys. 67, 279

[39] Gallagher T. F., "Rydberg Atoms" (1994), Cambridge Monographs on Atomic, Molecular and Chemical Physics, Cambridge, Cambridge University Press.

[40] Sibalić, N. & Adams, C. S. "Rydberg Physics", (IOP, 2018); [Online] Available: https://iopscience.iop.org/book/978-0-7503-1635-4

[41] H. Yang, X. Wang & X. Li, "The exciton-polariton properties of hexagonal BN based microcavity and their potential applications in BEC and superconductivity", (2021). Physical Review B (2021): n. pag. [Online] Available: arXiv:2107.14376 [cond-mat.mtrl-sci]

[42] C. Becker *et al*, "Oscillations and interactions of dark and dark-bright solitons in Bose-Einstein condensates", (2018). Nature Phys 4, 496–501 (2008). https://doi.org/10.1038/nphys962 [Online] Available: arXiv:0804.0544 [cond-mat.other]

[43] C. Vo, S. Riedl, S. Baur, G. Rempe & S Dürr, "Coherent Logic Gate for Light Pulses Based on Storage in a Bose-Einstein Condensate", (2012). Phys. Rev. Lett. 109, 263602

[44] C. Lee, "Wandering Bose-Einstein condensate may lead to scalable quantum computer", (2018). [Online] Available: https://arstechnica.com/science/2018/08/doing-the-quantum-mash-cloud-of-atoms-may-provide-new-way-to-compute/

[45] S. Dadras, A. Gresch, C. Groiseau, S. Wimberger & G. S. Summy, "Quantum Walk in Momentum Space with a Bose-Einstein Condensate", (2018). Phys. Rev. Lett. 121, 070402

[46] P. Singh, "A Study on the basics of Quantum Computing", (2005). [Online] Available: arXiv:quant-ph/0511061

[47] R. P. Feynman, "Simulating Physics with Computers", (1981). Int J Theor Phys 21, 467–488 (1982). https://doi.org/10.1007/BF02650179. Department of Physics, California Institute of Technology, Pasadena, California 91107. 1981.

[48] T. Boulier, M. J. Jacquet, A. Maître, G. Lerario, F. Claude, S. Pigeon, Q. Glorieux, A. Bramati, E. Giacobino, A. Amo, J. Bloch, "Microcavity Polaritons for Quantum simulation", (2020). Adv. Quantum Technol., 3: 2000052. https://doi.org/10.1002/qute.202000052

[49] V. Giovannetti, S. Lloyd, L. Maccone, "Advances in Quantum Metrology", (2011). Massachusetts Institute of Technology – Research Lab of Electronics and Dept. of Mechanical Engineering 77 Massachusetts Avenue, Cambridge, MA 02139, USA, 2011. [Online]. Available: https://arxiv.org/pdf/1102.2318.pdf

[50] Raimond, J. M., Vitrant, G. & Haroche, S., "Spectral line broadening due to the interaction between very excited atoms: 'the dense Rydberg gas'". J. Phys. B 14, L655-L660 (1981).

[51] M. Lewenstein, A. Sanpera, V. Ahufinger, "Ultracold atoms in Optical Lattices", First Edition, (2012). Oxford University Press.

[52] R. T. Sutherland and F. Robicheaux, "Coherent forward broadening in cold atom clouds", (2016). Department of Physics and Astronomy, Purdue University. Phys. Rev. A 93, 023407

[53] S. D. Jenkins and J. Ruostekoski, "Optical Resonance Shifts in the Fluorescence of Thermal and Cold Atomic Gases", (2016). Mathematical Sciences, University of Southampton. Phys. Rev. Lett. 116, 183601

[54] R. Jones, J. A. Needham, I. Lesanovsky, F. Intravaia and B. Olmos, "Modified dipole-dipole interaction and dissipation in an atomic ensemble near surfaces", (2018). School of Physics and Astronomy, The University of Nottingham. Phys. Rev. A 97, 053841

[55] A. Glicenstein, G. Ferioli, N. Šibalić, L. Brossard, I. Ferrier-Barbut, & A. Browaeys, "Collective shift in resonant light scattering by a one-dimensional atomic chain", (2020). Physical review letters, 124(25), 253602. https://doi.org/10.1103/PhysRevLett.124.253602 [Online]. Available: https://arxiv.org/pdf/2004.05395.pdf

[56] H. Christodoulidi, A. Bountis, & L. Drossos, "The effect of long-range interactions on the dynamics and statistics of 1D Hamiltonian lattices with on-site potential", (2018). Eur. Phys. J. Spec. Top. 227, 563–573 (2018). https://doi.org/10.1140/epjst/e2018-00003-9

[57] D. Del Castillo-Negrete, "Dynamics and self-consistent chaos in a mean field Hamiltonian model", (2008). Lecture Notes in Physics. DOI:10.1007/3-540-45835-2_13

[58] L. Pezzè, A. Smerzi, M. K. Oberthaler, R. Schmied & Philipp Treutlein, "Quantum metrology with nonclassical states of atomic ensembles," (2018). Rev. Mod. Phys. 90, 035005

[59] R. Santra and C. H. Greene, "Tensorial analysis of the long-range interaction between metastable alkaline-earth atoms", (2003). Phys. Rev. A 67, 062713 [Online] Available: https://arxiv.org/pdf/physics/0302060.pdf

[60] T. Ido and H. Katori, "Recoil-free spectroscopy of neutral Sr atoms in the Lamb-Dicke regime", (2003). Phys. Rev. Lett. 91, 053001 [Online] Available: https://arxiv.org/pdf/physics/0303032.pdf

[61] H. Katori, "Spectroscopy of strontium atoms in the Lamb-Dicke confinement", (2002). Proceedings of the 6th Symposium on Frequency Standards and Metrology, 323-330

[62] S. B. Nagel, P. G. Mickelson, A. D. Saenz, Y. N. Martinez, Y. C. Chen, and T. C. Killian, "Photoassociative spectroscopy at long range in ultracold strontium", (2004). Physical review letters vol. 94,8 (2005): 083004. doi:10.1103/PhysRevLett.94.083004 [Online] Available: https://arxiv.org/pdf/physics/0410030.pdf

[63] T. Ido, T. H. Loftus, M. M. Boyd, A. D. Ludlow, K. W. Holman and J. Ye, "Precision Spectroscopy and Density-Dependent Frequency Shifts in Ultracold Sr", (2005). Phys. Rev. Lett. 94, 153001. JILA, National Institute of Standards and Technology and University of Colorado.

[64] C. L. Vaillant, M. P. A. Jones and R. M. Potvliege, "Long-range Rydberg-Rydberg interactions in calcium, strontium and ytterbium", (2012). J. Phys. B: At. Mol. Opt. Phys. 45 135004. Department of Physics, Durham University.

[65] S. Stellmer, R. Grimm, and F. Schreck, "Production of quantum degenerate strontium gases: Larger, better, faster, colder", (2012). Phys. Rev. A 87, 013611 [Online]. Available: https://arxiv.org/pdf/1212.2539.pdf

[66] S. Zhang, P. Ramchurn, M. Menchetti, Q. Ubaid, J. Jones, K. Bongs and Y. Singh, "Novel repumping on ^{3}P$_0$ $\rightarrow$^{3}D$_1$ for Sr magneto-optical trap and Landé g factor measurement of ^{3}D$_1$", (2020). J. Phys. B: At. Mol. Opt. Phys. 53 235301

[67] R. K. Sinnot. "Chemical Engineering Design", 4th Edition. 2005.

[68] F. J. Vesely, Statistical Physics, The Maxwell Boltzmann distribution. (2005). Available: https://homepage.univie.ac.at/franz.vesely/sp_english/sp_print.pdf (accessed 04/11/21)

[69] The National Institute of Standards and Technology (NIST) database, [Online] Available: http://www.nist.gov/pml/data.

[70] B. Olmos, D. Yu, Y. Singh, F. Schreck, K. Bongs and I. Lesanovsky, "Long-range interacting many-body systems with alkaline-earth-metal atoms," Phys. Rev. Lett., vol. 110, p. 143 602, 14 2013. [Online]. Available: http://link.aps.org/doi/10.1103/PhysRevLett.110.143602.

[71] D. Yu, "Properties of far-field fluorescence from an ensemble of interacting Sr atoms", Phys. Rev. Lett. 2013, 110, 143602. (2013)

[72] M. H. Anderson, J. R. Ensher, M. R. Matthews, C. E. Wieman, and E. A. Cornell, "Observation of bose-einstein condensation in a dilute atomic vapor," Science, vol. 269, no. 5221, pp. 198–201, 1995, issn: 0036- 8075. eprint: http://science.sciencemag.org/content/269/5221/ 198.full.pdf. [Online]. Available: http://science.sciencemag.org/content/269/5221/198

[73] K.B. Davis, M.-O. Mewes, M. R. Andrews, N. J. van Druten, D. S. Durfee, D. M. Kurn and W. Ketterle, "Bose-Einstein Condensation in a Gas of Sodium Atoms", Phys. Rev. Lett. 75, 3969 (1995).

[74] C. C. Bradley, C. A. Sackett, J. J. Tollett and R. G. Hulet, Phys. Rev. Lett. 75, 1687 (1995).

[75] F. Dalfovo, S. Giorgini, L. P. Pitaevskii and S. Stringari, "Theory of Bose-Einstein condensation in trapped gases", (1998). Rev. Mod. Phys. 71, 463 [Online] Available: https://arxiv.org/pdf/cond-mat/9806038.pdf

[76] E.A. Cornell, J.R. Ensher, and C.E. Wieman, "Experiments in Dilute Atomic Bose-Einstein Condensation", (1999). JILA, University of Colorado and National Institute of Standards and Technology and Department of Physics. Collected Papers of Carl Wieman, pp. 533-584 (2008)

[77] T. Lahaye, C. Menotti, L. Santos, M. Lewenstein, and T. Pfau, "The physics of dipolar bosonic quantum gases", (2009). Reports on Progress in Physics, vol. 72, no. 12, p. 126 401, 2009. [Online]. Available: http://stacks.iop.org/0034-4885/72/i=12/a=126401.

[78] A. Debnath and A. Khan, "Investigation of Quantum Liquid in Quasi One Dimensional Bose-Einstein Condensate", (2020). Department of Physics, School of Engineering and Applied Sciences, Bennett University, Greater Noida, UP-201310, India. [Online] Available: https://arxiv.org/pdf/2008.00484.pdf

[79] L. Pitaevskii and S. Stringari, "Bose-Einstein Condensation" (2003). Oxford Science Publications.

[80] H. F. Hess, "Magnetic trapping of spin-polarized atomic hydrogen", (1986). Phys. Rev. B 34 3476

[81] P. Bouyer, V. Boyer, S.G. Murdoch, G. Dellanoy, Y. Le Coq, A. Aspect & M. Lecrivain, "RF-induced evaporative cooling and BEC in a high magnetic field" (2000). [Online] Available: https://arxiv.org/ftp/physics/papers/0003/0003050.pdf

[82] S. Chaudhuri, S. Roy & C. S. Unnikrishnan, "Evaporative Cooling of Atoms to Quantum Degeneracy in an Optical Dipole Trap", (2007). J. Phys.: Conf. Ser. 80 012036

[83] S. Stellmer, "Degenerate quantum gases of strontium", (2013). Innsbruck.

[84] J. C. Zhang, Z. L. Zhu, Y. F. Liu & J. F. Sun, "Elastic Scattering Properties of Ultracold Strontium Atoms", (2011). Henan Normal University. Chinese Phys. Lett. 28 123401

[85] M. Menchetti, "Experimental set-up for realising long-range interaction using strontium atoms in an optical lattice", PhD Thesis, University of Birmingham, (2017).

[86] C. J. Foot, "Atomic Physics". Oxford University Press, 2005.

[87] H. J. Metcalf *et al.*, "Laser Cooling and Trapping", (1999).

[88] H. Katori, T. Ido, Y. Isoya and M. Kuwata-Gonokami, “Magneto-Optical Trapping and Cooling of Strontium Atoms down to the Photon Recoil Temperature” (1999). Physical Review Letters, 82:1116-1119, Feb 1999.

[89] T. Mukaiyama, H. Katori, T. Ido, Y. Li, and M. Kuwata-Gonokami, “Recoil-limited laser cooling of ^{87}Sr atoms near the fermi temperature”, (2003). Phys. Rev. Lett., 90:113002, Mar 2003.

[90] T. H. Loftus, T. Ido, A. D. Ludlow, M. M. Boyd, and J. Ye, “Narrow Line Cooling: Finite Photon Recoil Dynamics”, (2018). Phys. Rev. Lett. 93, 073003 [Online] Available: arXiv:physics/0401055 [physics.atom-ph]

[91] V. I. Balykin, V. S. Letokhov, and V. I. Mishin, “Observation of the cooling of free sodium atoms in a resonance laser field with a scanning frequency”, (1979). Zh. Eksp. Teor. Fiz. 78, 1376-1385 (April 1980)

[92] B. Ole Kock, “Magneto-Optical Trapping of Strontium for use as a Mobile Frequency Reference,” (2013). PhD Thesis, University of Birmingham

[93] Q. Wang, Bai-Ke Lin, Y. Zhao *et al*, “Magneto-Optical Trapping of ^{88}Sr atoms with 689nm Laser,” (2011). Chin. Phys. Lett. 28 033201

[94] I. R. Hill, Y. B. Ovchinnikov, E. M. Bridge, E. Anne Curtis and P. Gill, “Zeeman Slowers for Strontium based on Permanent Magnets,” (2014). J. Phys. B: At. Mol. Opt. Phys. 47 075006 [Online] Available: arXiv:1402.5271 [physics.atom-ph]

[95] Qasim Hassan Ubaid, “Towards a strontium based stationary optical lattice clock” (2018), PhD Thesis, University of Birmingham.

[96] I. Courtillot, A. Quessada, R. P. Kovacich, J.-J. Zondy, A. Landragin, A. Clairon, and P. Lemonde, “Efficient cooling and trapping of strontium atoms”, Opt. Lett. 28, 468 (2003).

[97] M. Inguscio and L. Fallani, Atomic Physics: Precise Measurements and Ultracold Matter. Oxford Scholarship Online, 2013. DOI:10.1093/acprof:oso/9780198525844.001.0001

[98] R. Grimm, M. Weidem¨uller, and Y. B. Ovchinnikov, “Optical dipole traps for neutral atoms,” in, ser. Advances In Atomic, Molecular, and Optical Physics, B. Bederson and H. Walther, Eds., vol. 42, Academic Press, 2000, pp. 95 –170. [Online]. Available: http://www.sciencedirect.com/science/article/pii/S1049250X0860186X.

[99] I. R. Hill, “Development of an apparatus for a strontium optical lattice optical frequency standard,” (2007). PhD thesis, Department of Physics, Imperial College London, 2007.

[100] G. Pesce, G. Volpe,O. M. Maragó, P .H. Jones, S. Gigan, A. Sasso and G. Volpe, “A Step-by-step Guide to the Realisation of Advanced Optical Tweezers”, (2015). J. Opt. Soc. Am. B 32, B84-B98 (2015) [Online]. Available: https://arxiv.org/pdf/1501.07894.pdf

[101] A. Ashkin, "Acceleration and trapping of particles by radiation pressure", Phys. Rev. Lett. 24, 156–159 (1970).

[102] A. Ashkin, J. M. Dziedzic, J. E. Bjorkholm, and S. Chu, "Observation of a single-beam gradient force optical trap for dielectric particles", Opt. Lett. 11, 288–290 (1986).

[103] C. J. Pethick & H. Smith, "Bose-Einstein Condensation in Dilute Gases", Second Edition (2008). Cambridge.

[104] V. D. Ovsyannikov, V. G. Pal'chikov, H. Katori and M. Takamoto, "Polarisation and dispersion properties of light shifts in ultrastable optical frequency standards", Quantum Electronics, vol. 36, no. 1, pp. 3–19, 2006. doi:10.1070/QE2006v036n01ABEH013098.

[105] M. Takamoto, F.-L. Hong, R. Higashi and H. Katori, "An optical lattice clock", Nature 435, 321–324 (2005). https://doi.org/10.1038/nature03541

[106] H. Katori, "Optical lattice clocks and quantum metrology". Nature Photon 5, 203–210 (2011). https://doi.org/10.1038/nphoton.2011.45

[107] B. Olmos, D. Yu, Y. Singh, F. Schreck, K. Bongs & I. Lesanovsky, "Long-range interacting many-body systems with alkaline-earth-metal atoms", (2013). The University of Nottingham. Phys. Rev. Lett. 110, 143602

[108] R. H. Lehmberg, "Radiation from an N-Atom System. I. General Formalism". Phys. Rev. A 2, 883 (1970)

[109] D. F. V. James, "Frequency shifts in spontaneous emission from two interacting atoms". Phys. Rev. A 47, 1336 (1993)

[110] M. Nickerson, "A review of Pound-Drever-Hall laser frequency locking", JILA, University of Colorado and NIST, Boulder, CO 80309-0440, USA. [Online]. Available: http://jila1.nickersonm.com/papers/PDH%20Locking%20Review.pdf

[111] E. D. Black, "An introduction to Pound–Drever–Hall laser frequency stabilization" (2001). American Journal of Physics 69, 79 (2001); doi: 10.1119/1.1286663

[112] S. Viswam, "Advanced laser frequency stabilisation systems for mobile strontium optical lattice clocks", (2019). The University of Birmingham.

[113] T. Legero, T. Kessler and U. Sterr, "Tuning the thermal expansion properties of optical reference cavities with fused silica mirrors", (2010). Physikalisch–Technische Bundesanstalt (PTB), Bundesallee 100, 38116 Braunschweig, Germany. [Online]. Available: https://arxiv.org/pdf/1002.2070.pdf

[114] B. Kaltenhäuser, H. Kübler, A. Chromik, J. Stuhler, and T. Pfau, "Low retaining force optical viewport seal", (2007). Review of Scientific Instruments 78, 046107 (2007); https://doi.org/10.1063/1.2723065

[115] H. A. Adam *et al*, "Indium seals for dismountable vacuum systems" (1957). J. Sci. Instrum. 34 123

[116] Review of Scientific Instruments 43, 1088 (1972); https://doi.org/10.1063/1.1685850 Submitted: 24 April 1972. Published Online: 04 November 2003

[117] S. J. M. Kuppens, K. L. Corwin, K. W. Miller, T. E. Chupp, and C. E. Wieman, "Loading an optical dipole trap", (2000). Phys. Rev. A 62, 013406 – Published 13 June 2000

[118] M. D. Barrett, J. A. Sauer, and M. S. Chapman, "All Optical Formation of an Atomic Bose-Einstein Condensate", (2001). Phys. Rev. Lett. 87, 010404 [Online] Available: arXiv:cond-mat/0106027 [cond-mat.soft]

[119] G. Cennini, G. Ritt, C. Geckeler *et al.* "Bose–Einstein condensation in a CO_2-laser optical dipole trap", (2003). Appl. Phys. B 77, 773–779 (2003). https://doi.org/10.1007/s00340-003-1333-1

[120] J. Kobayashi, Y. Izumi, M. Kumakura & Y. Takahashi, "Stable all-optical formation of Bose–Einstein condensate using pointing-stabilized optical trapping beams", (2006). Appl. Phys. B 83, 21–25 (2006). https://doi.org/10.1007/s00340-006-2140-2

[121] T. Gericke, P. Würtz, D. Reitz, C. Utfeld & H. Ott, "All-optical formation of a Bose–Einstein condensate for applications in scanning electron microscopy", (2007). Appl. Phys. B 89, 447–451 (2007). https://doi.org/10.1007/s00340-007-2862-9

[122] T. Kinoshita, T. Wenger, & D. S. Weiss, "All-optical Bose-Einstein condensation using a compressible crossed dipole trap", (2005). Physical Review A - Atomic, Molecular, and Optical Physics, 71(1), [011602]. https://doi.org/10.1103/PhysRevA.71.011602

[123] Faulhaber Technical Manual. 7000.05038, 8th edition, 9-11-2018 [Online] Available: www.faulhaber.com

[124] H. Hagman, P. Sjölund, S. J. H. Petra *et al.* "Assessment of a time-of-flight detection technique for measuring small velocities of cold atoms", (2009). J. Appl. Phys. 105, 083109; https://doi.org/10.1063/1.3097466

[125] M. Boyd, T. Zelevinsky, A. Ludlow, S. Blatt, T. Willette, S. Foreman, and J. Ye, "Nuclear Spin Effects in Optical Lattice Clocks", (2007). Phys. Rev. A 76, 022510 (2007). [Online] Available: arXiv:0704.0912 [physics.atom-ph]

[126] A. D. Ludlow, M. M. Boyd, T. Zelevinsky, S. M. Foreman, S. Blatt, M. Notcutt, T. Ido, and J. Ye, "Systematic study of the ^{87}Sr clock transition in an optical lattice", (2005). Phys. Rev. Lett. 96, 033003 (2006). [Online] Available: arXiv:physics/0508041 [physics.atom-ph]

[127] S. Stellmer and F. Schreck, "Reservoir spectroscopy of $5s5p\,^3P_2$-$5snd\,^3D_{1;2;3}$ transitions in strontium", (2018). Phys. Rev. A 90, 022512 (2014). [Online] Available: arXiv:1406.0409 [physics.atom-ph]

[128] F. Hu, I. Nosske, L. Couturier, C. Tan, C. Qiao, P. Chen, Y. H. Jiang, B. Zhu, and M. Weidemüller,, "Analyzing a single-laser repumping scheme for efficient loading of a strontium magneto-optical trap", (2019). Phys. Rev. A 99, 033422 (2019). [Online] Available: arXiv:1812.01258 [physics.atom-ph]

[129] N. Beverini, E. Maccioni, and F. Strumia, "g_J Factor of neutral calcium ^{3}P metastable levels" , (1998). J. Opt. Soc. Am. B/ Vol. 15, No. 8/August 1998

[130] E. R. Cohenand B. N. Taylor, "The 1986 adjustment of the fundamental physical constants", (1987). Rev. Mod. Phys. 59, 1121 (1987).

[131] F. Owen, J. Jones. Untitled PhD Thesis (2022). University of Birmingham.

[132] T. Lahaye, C. Menotti, L. Santos, M. Lewenstein and T Pfau, "The physics of dipolar bosonic quantum gases", (2009). Rep. Prog. Phys. 72, 126401 (2009). [Online] Available: arXiv:0905.0386 [cond-mat.quant-gas]

[133] J. E. Sansonettia and G. Nave, "Wavelengths, Transition Probabilities, and Energy Levels for the Spectrum of Neutral Strontium (Sr I)", (2010). Journal of Physical and Chemical Reference Data 39, 033103 (2010); https://doi.org/10.1063/1.3449176

[134] G. García and J. Campos, J. Quant. Spectrosc. Radiat. Transfer. 39, 477 (1988).

[135] J R Rubbmark1 and S A Borgström 1978 Phys. Scr. 18 196. "Rydberg Series in Strontium Found in Absorption by Selectively Laser-Excited Atoms"

[136] X. Zhou, X. Xu, X. Chen, and J. Chen, "Magic wavelengths for terahertz clock transitions", (2010). Phys. Rev. A 81, 012115 – Published 25 January 2010